Master's thesis

NTNU
Norwegian University of Science and Technology
Faculty of Information Technology and Electrical Engineering
Department of Electric Power Engineering

Arve Starheim Ytrehus

Modeling of a Maritime DC-distribution System Supplied from a Diode Rectifier Connected Synchronous Generator

Master's thesis in Electric Power Engineering
Supervisor: Roy Nilsen
June 2019

NTNU
Norwegian University of Science and Technology

Arve Starheim Ytrehus

Modeling of a Maritime DC-distribution System Supplied from a Diode Rectifier Connected Synchronous Generator

Master's thesis in Electric Power Engineering
Supervisor: Roy Nilsen
June 2019

Norwegian University of Science and Technology
Faculty of Information Technology and Electrical Engineering
Department of Electric Power Engineering

NTNU
Norwegian University of
Science and Technology

Problem Description

The DC-distribution system has gained increased attention in the marine industry. Especially in application where Hybrid Power systems gives potential environmentally friendly solutions and reduced operation cost. The most common solutions today are Engine-Generator sets as main power source, operated either with diesel or Liquefied Natural Gas (LNG). The Gen-Sets are connected to the DC-link either with diode/thyristor-rectifier or 3-phase inverter. The main objective of the project is to model the generator/diode system.

Previous theses have investigated the instability problems concerning the synchronous generator and diode rectifier set-up. However, these theses have focus heavily on simulations of the system. The objective in this project is a theoretical analysis of the system.

- Emphasis should be on obtaining a solid theoretical foundation and develop detailed models of the system.
- These models shall be used for field current control design and stability analysis of the system.
- If sufficient time, a voltage controller as a part of power control should be included.

Trondheim 2019
Prof. Roy Nilsen

Preface

This thesis is the final work of the 2-year master study ”Electric Power Engineering” and was written in the spring of 2019 at the Norwegian University of Science and Technology (NTNU). The thesis is written for the Department of Electric Power Engineering at the Faculty of Information Technology and Electrical Engineering.

The thesis work consists of modeling of a maritime DC-distribution system supplied by synchronous generators, where the voltage is rectified with three-phase diode rectifiers. The models are applicable for regulator tuning purposes and stability considerations.

I would like to thank my supervisor Roy Nilsen for support and guidance. I appreciate the time set aside to help and advise me during the thesis work.

Arve Starheim Ytrehus

Trondheim, June, 2019

Abstract

Strict emission regulations have been introduced to the maritime sector by the International Maritime Organization. New and existing technology are evaluated with an increased focus on developing environmentally friendly solutions. The DC-distribution system is an old technology which has been revitalized by the progression in the power electronic solutions. The DC-distribution system offers fuel saving potentials not accessible in its AC-counterpart. The objective of this thesis is to develop system models applicable for control system design purposes and stability analysis.

The system consists of synchronous generator, diode rectifier and a DC-link capacitor. Diode rectifiers are preferred in many cases due to low prince and simple control structures. However, diode rectifier has no option for voltage control. The DC-link voltage control is therefore realized through generator field current regulation.

A model containing the different system elements was constructed. The model was linearized, Laplace transformed and represented as a signal flow diagram. A transfer function describing the relation between the field voltage and field current was deduced by node and branch reducing the signal flow diagram. This function was utilized in the regulator tuning.

The theory presented in this report lays a solid foundation for further modeling, controller design and system stability analysis. The initial method presented for tuning the field current controller could be evolved further to develop a standardized tuning principle for this system. However, it is evident that some aspect concerning modeling, stability and tuning regarding the field circuit needs to be examined further. The challenges expressed concerning the inner field circuit regulator should be priorities before further voltage control design is conducted.

Sammendrag

Strenge utslippsreglement har blitt introdusert i den maritime sektor av den Internasjonale Maritime Organisasjon. Ny og eksiterende teknologi er analysert med høyt fokus på å utvikle mer miljøvennlige løsninger. DC distribusjonssystem er en gammel teknologi som har fått nytt liv takket være utviklinger innen løsninger med kraftelektronikk. DC distribusjonssystemet har muligheter for drivstoffbesparelse som ikke er tilgjengelig i AC-systemer. Målet med denne oppgaven er å utvikle modeller for systemet som kan brukes for kontrollsystemdesign og stabilitetsanalyse.

Systemet i denne oppgaven består av en synkrongenerator, en diodelikeretter og en DC-linkkondensator. En diodebro er å foretrekke i mange tilfeller grunnet lav pris og enkel kontrollstruktur. Det er ikke mulighet for spenningskontroll i en diodebro. Regulering av DC-linkspenningen blir derfor realisert gjennom regulering av generatorens feltstrøm.

En modell som inneholder de ulike systemelementene er blitt konstruert. Modellen er linearisert, Laplacetransformert og representert i et signalflytdiagram. En transferfunksjons som beskriver relasjonen mellom felt spenningen og felt strømmen er utledet ved at signalflytdiagrammet er node- og grenredusert. Denne transferfunksjonen er brukt i feltkontrollerinnstilliger.

Teorien presentert i denne rapporten danner et solid grunnlag for videre modellering, kontrollerdesign og stabilitetsanalyser. Metoden presentert for å utlede feltkontrollerinnstilligene presenter kan benyttes for videre utvikling av standardiserte innstillingsmetoder for slike system. Videre utredning av modellering, stabilitet og innstilliger av fellstrømkontroller er nødvendig. Disse utfordringene bør prioriteres før videre arbeid rundt designet av spenningskontolleren fortsetter.

Table of Contents

List of Tables

List of Figures

Nomenclature

Abbreviations:

AC	Alternating Current
DC	Direct Current
Gen-Set	Generator-Engine
LNG	Liquefied Natural Gas
ICE	Internal Combustion Cngines
DP	Dynamic Positioning
IMO	International Maritime Organization
MARPOL	Maritime Pollution
CCM	Continuous Conduction Code
DCM	Discontinuous Conduction Code
NCM	Non-conduction Mode
KVL	Kirchhoff's Voltage Law
pu	Per Unit
NAVSEA	Naval Sea System Command
SG	Shaft Generator
IPS	Integrated power system
SFOC	Specific Fuel Oil Consummation
ESS	Energy Storage System
MVDC	Medium Voltage Direct Current
LVDC	Low Voltage Direct Current

Symbols:

U	Voltage
I	Current
R	Resistance
L	Inductance
C	Capacitance
P	Active power
S_p	Droop curve
Ψ	Flux linkage
U_{LL}	Line-to-line voltage
ω_n	Nominal angular frequency
μ	Commutation angle
$\hat{I}_1$	First harmonic current amplitude
I_a	Current phase a
τ	Torque [pu]
n	Generator speed
f	Frequency
θ	Rotor position angle
L_m	Air gap inductance
L_σ	Leakage inductance
L_g	Rotor dependent air gap inductance
$\mathbf{R}$	Resistance matrix
$\mathbf{J}$	Matrix utilized in transformation
$\mathbf{x}$	Reactance matrix
T	Time constant
U_{dio}	Ideal rectifier voltage
U_{dk}	Commutation voltage loss
L_f	Arbitrary inductance between generator and rectifier
G	Transfer function
h_0	Open loop tranfer function
M	Closed loop transfer function

Small letters represents per unit values

Subscript:

a, b, c	Phases
α, β, γ	Coordinate vectors transformed system
s	Stator quantity
r	Rotor quantity
f	Field circuit quantity
z	Intermediate circuit quantity
DC	DC-link quantity
g	Negative stator current quantity
D	d-axis actual values
d	d-axis per unit values
Q	q-axis actual values
q	d-axis per unit values

Superscript:

S	Stator quantities in stator coordinates
R	Rotor quantities in rotor coordinates
SR	Stator and rotor quantities in their original coordinate system
s	Referred to stator
r	Referred to rotor
k	Referred to transformed frame

Chapter 1

Introduction

1.1 Background

Technological development has seen an ever-increasing dependency on electrical solutions, and the maritime sector is no exception. Introduction of diesel-electrical systems has transformed propulsion system form pure mechanical system, operated with internal combustion engines (ICE), into hybrid systems. The propulsion itself is realized with electrical motor, while the electrical power is produced by ICEs. The majority of loads, such as hotel and service loads in cruise ships and Dynamic Positioning (DP)- system for subsea operation are also usually electrical [1]. It is desirable to keep the fuel consummation of the ICEs to a minimum for economic reasons, but also due to strict emission regulations. The *International Maritime Organization's* (IMO) MARPOL Annex VI calls for a progressive reduction in global emissions of SOx, NOx and particulate matters [2].

New technologies and solutions are explored in order to reach these goals. In the DC-distribution case, an old concepts is made viable by rapid development of power electronic components [3]. Previous challenges such as transformation between voltage levels and system protection are realized with power electronic solutions. The DC-power system is a further development of the already existing DC-link of modern shipboard power systems. Usually more than 80% of total electric power consummation occurs in propulsion or thruster system with AC/DC converters with internal DC-links [4]. The relocation of the rectifying unit to the supply network makes it possible to keep the proven technology, such as AC-generators, inverter modules and AC-motor, while eliminating the AC-switchboard and transformers.

The DC-distribution system has some unique attributes compared to the AC-system. It is possible to operate the prime movers at variable speed, since constant frequency regulation is not required. The system can implement energy storage systems in a simple fashion and has space saving potential compared to AC-systems. Even though the DC-distribution in shipboard power system is in an early stage, pilot project reports positive results. Among others, ABB has published a paper regarding their DC-grid on board MPSV Dina Star [5]. This states that a reduction in fuel consummation of 20% and 40% for medium and high-speed generator respectively for partial load operation. In regard to space saving a 30% reduction is reported.

The rectification unit can be either be active, operated with transistors, or passive which utilizes diodes. The active rectifier has the option of controlling the DC-link voltage by switching the transistors on and off. The diode rectifier on the other hand has a constant output voltage based on the input voltage. The active system has more options with regard to voltage control, and therefore power flow. However, a passive system, like a three-phase diode rectifier, is preferred in many chases due to simpler control structure and lower price.

The simpler control structure of the passive rectifier system results in fewer controllable parameter. The only option for voltage regulation with this system is either to change the prime mover speed or to regulate the magnetizing current of the synchronous machine. However, the prime mover speed is controlled according to optimal fuel consummation. Therefore, the magnetizing current must be regulated based on prime mover speed and DC-link current to achieve specified DC-link voltage.

1.2 Scope of work

It is then evident that the passive system would result in a slower DC-link voltage control compared to the active system, due to time constants in the exciter circuit. There has also been reports of instability in these types of regulation systems. In order to investigate these challenges a proper model of the different elements of the system need to be developed. The tasks to be addressed in this thesis are:

- Develop models for the different elements
- Combined into one model representing the entire system. This model should be applicable for control design and stability analyzing purposes.
- Deduced a process transfer function describing the relation between the field circuit voltage and current
- Design the field circuit controlled based on the resulting transfer function
- Stability analysis
- If enough time, design a voltage controller
- Additional, include a theory part about the shipboard power system, DC-distribution and important system elements.

The problem description requires a solid theoretical foundation and a emphasis on system modeling. The allocated time to voltage controller design and stability analysis therefore depends on how much time is left after the modeling and deducing of transfer function are completed.

1.3 Software

This project has a large emphasis on deriving mathematical expressions for the system. This includes complicated calculations, simplifications and manipulation of equations, matrices and transfer function. These operations are evaluated in Maplesofts mathematics program Maple. Matlab is utilized to plotting and analyzing functions and transfer function, the report itself is written in Overleaf, Online LaTeX Editor.

1.4 Report structure

This report is divided into five main parts. The first part, in chapter 2, is a summary of the specialization project. This chapter looks into important findings which are utilized for further development in the master thesis.

The second main part, chapter 3, gives an introduction into the shipboard power system. The chapter opens by presenting the characteristics-, and design philosophies for the shipboard power system. Then follows a short introduction to the prime mover. The second to last sub-chapter includes an overview of the DC-distribution system. Here are some of the benefits, such as fuel and space saving, and some challenges with the DC-system investigated. The chapter is rounded out by comparing the control schemes of the AC and DC control systems.

In chapter 4, which contains the third main section, models are developed for the different elements in the system. A major part of this project is the introduction of the synchronous machine into the model. The rather complicated equations of the synchronous machine is transformed in order to be applicable for a control purpose. The diode rectifier model utilized in the specialization project are then restructured such that the pu-values corresponds to synchronous machine and to include a frequency dependency. Lastly, the two models are combined and analyzed.

The last main part, the control system, is analyzed in chapter 5. A signal flow diagram is constructed for the combined system. The signal flow diagram is node and branch reduced and utilized for tuning the field current controller. Finally, the open- and closed loop transfer functions for the field current control system are plotted and analyzed.

Then follows discussion, conclusion and further work in chapter 6,7 and 8 respectively.

Chapter 2

Summary of the Specialization Project

A Specialization Project was conducted during the fall of 2018 in the course TET 5500 at the Department of Electric Power Engineering at NTNU. The project was a study of the three-phase diode rectifier connected to a DC-link. Solutions with this configuration has experienced instability in the past. It was therefore important to obtain a solid understanding of the operation principles of the system.

A large capacitor was connected to the DC-link, which results in an assumption of constant DC-link voltage without ripple. This differs from the classical model, where the load current is assumed constant. Despite the widespread use of such a system, it has seen a discrepancy in analysis compared to the constant current load case [6]. While the mechanics at work differs in the two cases, the constant current model is still utilized for constant voltage loads. The main objective of the specialization project was to develop a model for the constant voltage case, then compare it to the constant current model and simulated results of the actual system.

Different methods were utilized to simplify the governing equations of the constant voltage operation in order to deduce a simple, yet accurate, mathematical model. However, the resulting model did not fulfill these requirements. On the other hand, the constant current model was proven to be accurate within nearly the entire operation region of the system. Considering these findings, it was decided to continue with this model. The following sub-chapter is a summary of the findings which has importance for the future work.

2.1 Operation of the three-phase rectifier

A schematic of the circuit analyzed in specialization project is presented in figure 2.1. The system consisted of a three-phase rectifier, commutation inductances, a balanced three-phase source and, and as mentioned above, a very large capacitor.

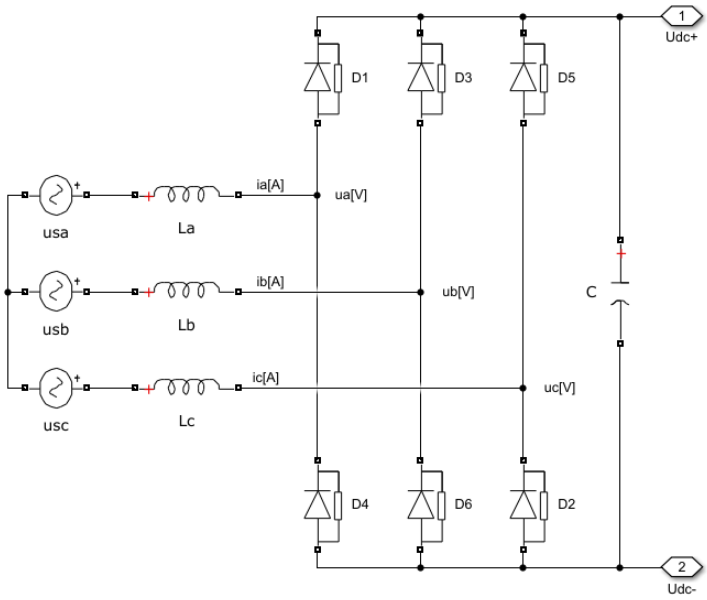

Figure 2.1: Illustration of the system

The operation states of system were investigated [7] and categorized into three modes:

- Non-conduction mode (NCM)
- Discontinuous conduction mode (DCM)
- Continuous conduction mode (CCM)

The Non-conduction mode is when the voltage on the DC-link are constantly higher than the rectified supply voltage. This occur when loads feeds power back to the DC-link, causing the voltage to rise. This state is self-explanatory from an operation perspective and was not given much attention in the specialization project. In discontinuous conduction the currents stay zero for an extended period. While in continuous conduction mode the currents only pass through zero, resulting in an almost sinusoidal supply current. The broadest focus was given to DCM. This includes bridge input voltages, bridge input line voltage, phase currents and harmonic analysis. The analysis of CCM was restricted to bridge input voltages and boundary conditions. A thorough analysis of the different states can be found in [6].

2.2 Constant current model

The expression for the DC-voltage and $\cos(\mu)$ for the constant current model are presented in equation 2.1 and 2.2 respectively [8].

$$U_{dc} = \frac{3\sqrt{2}}{\pi} U_{LL} - \frac{3}{\pi} \omega L I_{dc} \tag{2.1}$$

$$\cos(\mu) = 1 - \frac{2L\omega}{\sqrt{2}U_{LL}} I_{dc} \tag{2.2}$$

It was stated above that the constant current model was accurate for nearly the entire operation region of the system. This statement is based on a comparison between simulated and calculated results in the specialization project. The results are presented in table 2.1. A close correspondence between calculated and simulated results can be observed. There are some deviations in the periphery regions.

Table 2.1: Comparison of simulated and calculated DC-link voltage and commutation interval

$Power$ $[MW]$	X_{L-pu} $[pu]$	I_{dc} $[A]$	U_{dc-sim} $[V]$	$U_{dc-calc}$ $[V]$	μ_{sim} $[deg]$	μ_{calc} $[deg]$
0.16	0.1	217	923.0	923.7	5.5°	10.5°
0.64	0.1	780	897.9	903.4	16.9°	20.0°
1.00	0.1	1372	874.3	882.1	24.5°	26.3°
0.16	0.2	219	913.1	915.7	10.8°	15.0°
0.64	0.2	808	866.4	873.3	27.3°	28.9°
1.00	0.2	1461	820.7	826.2	39.3°	39.3°
0.64	0.3	221	903.7	907.6	14.9°	18.4°
0.64	0.3	837	835.4	841.0	35.7°	36.3°
1.00	0.3	1556	766.6	762.5	55.1°	50.4°
0.16	0.4	237	894.6	899.3	18.7°	21.4°
0.64	0.4	865	805.3	806.3	43.1°	43.0°
1.00	0.4	1690	709.4	687.9	63.0°	61.0°

2.3 Power factor and harmonics

The equations for the first harmonic current magnitude and $cos(\varphi)$ is presented in equation 2.3 and 2.4 respectively. The method utilized for deriving these equations is based on assumption that the higher harmonics has little influence on the systems active power transfer. The voltages harmonics on the rectifier input can be interpreted as the voltage drop of the harmonic current over the commutation inductance. This results in a phase shift of 90 degrees between the voltage and each higher harmonic. The active power of the higher harmonics is then more or less zero [9].

$$\hat{I}_1 = \frac{2\sqrt{3}}{\pi} I_{dc} \tag{2.3}$$

$$\cos(\varphi_1) = \frac{1}{2} + \frac{\cos(\mu)}{2} \tag{2.4}$$

Two different approximation was investigated regarding the currents. Firstly, the calculated first harmonic current was compared to simulate first harmonic current. Then the simulated first harmonic current was compared to the simulated phase current. The first harmonic current was compared to the phase current to look into the possibility to use the first harmonic current as an approximation of the phase current. The results are presented in table 2.2. There were some inaccuracies at low power/inductances due to the relatively high current ripple, resulting in the constant current assumption to be inaccurate. The high current ripple also cased the approximation of phase current equal the first harmonic current to be inaccurate, due to a significant amount of higher harmonics.

Table 2.2: First harmonic currents calculated from the constant current model

$Power$ $[pu]$	X_{L-pu} $[pu]$	I_{dc} $[A]$	I_a $[A]$	I_{a1-sim} $[A]$	$I_{a1-calc}$ $[A]$
0.16	0.1	217	$279\angle -32.2°$	$244\angle -13.2°$	$239\angle -7.4°$
0.64	0.1	780	$905\angle -23.1°$	$863\angle -15.9°$	$860\angle -14.1°$
1.00	0.1	1372	$1557\angle -23.9°$	$1509\angle -19.5°$	$1513\angle -18.7°$
0.16	0.2	219	$262\angle -25.5°$	$244\angle -13.7°$	$242\angle -10.6°$
0.64	0.2	808	$911\angle -24.6°$	$888\angle -20.8°$	$891\angle -20.4°$
1.00	0.2	1461	$1613\angle -28.4°$	$1591\angle -26.4°$	$1612\angle -27.5°$
0.16	0.3	221	$259\angle -23.8°$	$246\angle -15.2°$	$244\angle -13.0°$
0.64	0.3	837	$928\angle -26.8°$	$913\angle -24.8°$	$924\angle -25.5°$
1.00	0.3	1556	$1692\angle -32.9°$	$1681\angle -32.1°$	$1726\angle -35.1°$
0.16	0.4	237	$247\angle -23.2°$	$246\angle -16.7°$	$244\angle -15.1°$
0.64	0.4	856	$933\angle -28.6°$	$931\angle -28.3°$	$958\angle -30.0°$
1.00	0.4	1690	$1780\angle -37.5°$	$1777\angle -37.3°$	$1865\angle -42.4°$

2.4 Important notes for further work

The voltage was supplied from an ideal three-phase source during the project work. This simplification was utilized while attempting to deduce a mathematical model of the system. In the thesis work the balanced three-phase source is replaced with a complete model of the synchronous generator. The rectifier model must be restructured to accommodate for this change.

The non-conducting mode was just briefly analyzed in the project work. This is due to the self-explanatory nature of this mode. When the voltage on the DC-link exceeds the bridge input voltage, no current is flowing through the rectifier. However, this mode of operation is more important from a control and stability perspective. The voltage regulation for this system is obtained through regulating the generator magnetizing current. The challenge occurs when a load is feeding power backwards onto the DC-link. This leads to a voltage increase on the DC-link which the regulator, without success, tries to keep at reference value. This leads to an integral wind-down in the regulator. It is therefore important to implement a countermeasure in the voltage controller to deal with this problem.

Chapter 3

Shipboard power system

While the fundamental concepts between the terrestrial power system and the shipboard power system are similar, the difference in size, spinning reserves and criteria for reliability and dependability results in different design philosophies for the two systems. System failure is more critical for ships, due to the safety of the passengers and crew. Shipboard power systems are therefore design with high levels of reliability and dependability. These terms are defined as following [1]:

- *Reliability*: The system reliability is a measurement of the effect of component failure and internal errors. The reliability is calculated from component mean time to fail statistics and static dependency analysis.
- *Dependability*: Describes the system's ability to continue operation despite internal errors or component failure.

A well formulated description of design philosophy for the naval power system is presented in the Naval Sea System Command (NAVSEA) *Design Practices and Criteria Manual, Electrical Systems for Surface Ships, Chapter 300* [1] [10]:

- The primary aim of the electric power system design will be for survivability and continuity of the electrical power supply. To ensure continuity of service, consideration shall be given to the number, size and location of generators, switchboard, and to the type of electrical distribution systems to be installed and the suitability for segregating or isolating damaged sections of the system.

A common principle to achieve both reliability and dependability is redundancy. For instance, according to DNV-GLs *Dynamic positioning vessel design philosophy guidelines*[11], redundancy is the concept which achieves the worst case failure design intent. The worst-case design intent is defined as minimum amount of propulsion and control equipment remaining operating after a worst case failure.

3.1 Characteristics

The shipboard power system shares many of the same characteristics as a terrestrial microgrid. A terrestrial mircogrid is defined, according to [12], as an electrical and geographical small power systems. They are capable of operating connected to a national grid or as a standalone power system (islanded operation). When the microgrid is in island operation strict requirements, such as energy independence and service quality for an extended period, applies. The shipboard powers system can then for all intents and purposes be defined as a microgrid.

Due to the many similarities, the two systems have the possibility to share design philosophies, use the same equipment, and apply related control strategies. It is important to map the characteristics of these system, in order to determine the correct design solutions. A thorough examination of the similarities between terrestrial microgrids and shipboard power systems, and where they differ, is presented in [12]. Many of the same findings, with focus on the shipboard power systems characteristics, is discussed in [1] and [10] and presented below:

Frequency

Traditional the shipboard power system is designed for a specific frequency, usually 60 Hz, due to comparability and equipment rating. The large use of 60 Hz, or 50 Hz in terrestrial installations, drives down the price compared to equipment operating on other frequencies. The frequency of a shipboard system cannot be assumed constant, because of the limited inertia of prime movers and generator. Rapid power variation cause frequency fluctuations which can persist for a couple of seconds. The introduction of DC-power systems eliminates the necessity of constant frequency and dependency on frequency converting components.

Power generation and load shedding

A shipboard power system operating at sea has no option for grid-connection and needs to be dimension to serve the peak demand of power. Load shedding in these systems relies on constantly monitoring the generators output. A predetermined load-shedding scheme is activated when loads exceeds given value for a period of time. This is in contrast to terrestrial microgrids, where the power provider does not own the loads. Load-shredding are then dependent on negotiations done in advance.

Time-scale separation

In shipboard power system the time constants of controls, machine dynamics and electric dynamics fall into the same range of milliseconds to seconds. The common practice of time-scale separation is therefore much more difficult.

Load types and dynamics

Loads in the shipboard power system are usually constant impedance load or constant power loads. The constant impedance loads are for instance hotel and service loads, while propulsion, thrusts or other loads connected through power converters are constant power load. The system is subject to rapid changes is power demand. This is due to system and equipment with high power ratings, such as propulsion, switching on and off. This load may be intermittent and operate in the range from kW to MW on timescales down to milliseconds. This introduces a high degree of dynamics into the system which needs to be taken into account.

System size and electrical distances

The shipboard power system can utilize a high level of central control due to the limited size of the system. The short electrical distances make modeling of the transmission lines unnecessary, trivializing the power flow problems. In addition, the short electrical distances strengthen the dynamic coupling of the various sub-systems of the power system.

Stability

Both microgrids and shipboard power have distributed power architecture where different voltage areas are separated through converters. These kinds of constant power loads introduce a destabilization effect into the system, which are more severe as constant power to linear load ratio increases [13].

3.2 Grid-design

The shipboard power system has been through a lot of changes. Especially in the later years, with the rapid development of power electronics, the trend has shifted from dependency on mechanical system toward electrical systems. The push toward more environmentally friendly solutions, which still must adhere to strict safety regulations, requires constant evaluation of the grid design philosophy.

3.2.1 Power generation configurations

Conventional mechanical/electrical-drive configuration

Traditionally, the propulsion system was mechanical-driven where the prime mover was connected to the propeller shaft through a reduction gear [14], while separate auxiliary diesel generator was utilized to produce power to the ship's service loads. On many ships the mechanical system was replace with an electrical-drive system to gain faster response [1]. The result are two separated power system, presented in figure 3.1 [1]. The existing power system supplying the service loads, and the new power system supplying the propulsion. In this configuration the power cannot freely be distributed between the systems. It might therefore be necessary to have an increased number of running prime mover. A typical separated system has two propulsion system, with two prime movers each for redundancy. Additional, three to five smaller auxiliary diesel generators utilized for the service load power system [14]. This could result in multiple prime movers running at reduced load. Since the prime movers are least efficient at low load, this would result in an increased fuel consummation.

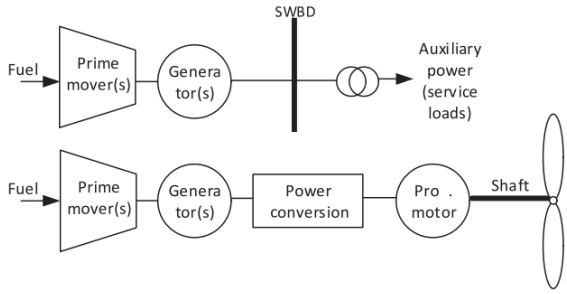

Figure 3.1: Segregated power system

Shaft generators configuration

In this configuration the main generator is mounted directly on the propeller shaft. This generator, named shaft generator (SG), is then driven by the ships main engine. The ship's main engine has normally a lower fuel consummation then auxiliary diesel generators and has the possibility to run on less expensive heavy fuel oil or LNG [15]. The downside of this system has historically been the dependency on constant propulsion speed to maintain network frequency. A common solution was to control propulsion trust and ship speed by adjusting the propeller pitch, which leads to increased fuel consummation. The modern solution is to add a frequency converter to the configuration. The frequency converter enables main engine speed changes, while at the same time maintaining stable frequency and voltage. The shaft generator configuration can therefore be a good alternative to the separated electric-drive configuration.

Integrated power system

Another configuration introduced to overcome the problems with the conventional electric-drive power system is the integrated power system [1]. In this configuration, presented in figure 3.2 [1], the power generation units delivers power to a shared power grid. The integrated power system then supplies all the individual consumers on board, similar to the terrestrial utility grid.

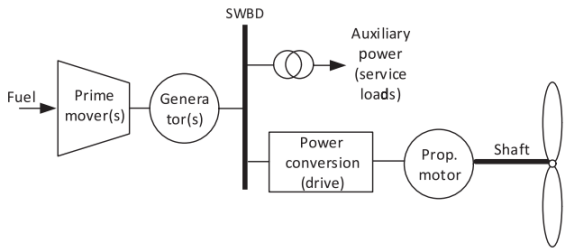

Figure 3.2: Integrated power system

The main advantage of the IPS is the ability to share power, which improves power flexibility and availability. The ability to share power between the system open the possibility to reduce the number om prime movers in the system, while at the same time maintain redundancy. A potential design is presented in figure 3.3. A equivalent integrated system to the separated system in chapter 3.2.1 could manage with to-three large prime movers, and two auxiliary diesel generators [14]. Fewer gen-set operation at more ideal loading condition results in less fuel consummation, which is preferred both from an economical and environmental perspective.

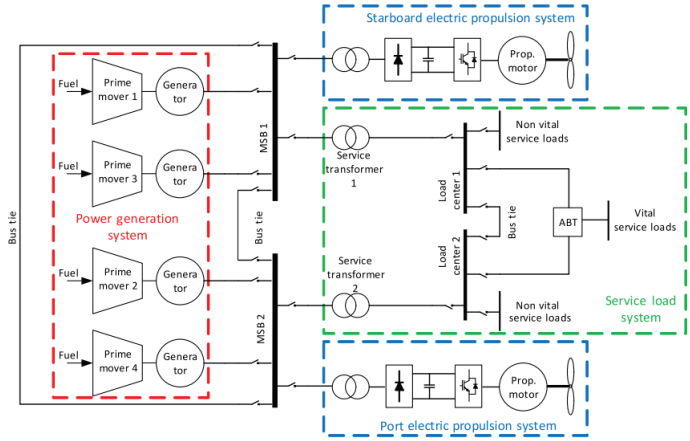

Figure 3.3: Integrated power system topology

3.2.2 Zonal distribution topology

A zonal distribution topology is often implemented together with the IPS to ensure redundancy [1]. Traditionally, redundancy was implemented by longitudinal power cables connecting vital loads to multiple switchboards via alternate power routes. This solution, the radial distribution system, is heavy and bulky when the amount of vital loads increases. A new configuration, introduced in the 1990s, was the zonal distribution system. A comparison between the two systems is shown in figure 3.4 [1]. The zonal system provides vital load from short feeder cables running between switchboards on port- and starboard sides of the ship. This enables the removal of long feeder cables, reducing weight and cost, and as a potential benefit, reduces fuel consummation and emissions. The IPS/Zonal topology enables easier post-construction installations and flexible installation regarding redundant solutions.

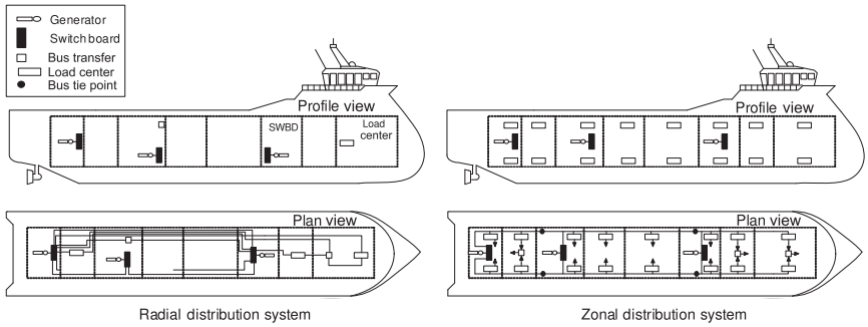

Figure 3.4: Radial vs Zonal distribution system

3.3 Prime Mover

As previously stated, the shipboard synchronous generators are driven by internal combustion engines (ICE), usually operated by diesel, heavy fuel oil or, in recent time, LNG. The combustion engine is constantly modified to increase efficiency and reduce emissions. Nevertheless, the peak utilization factor of the ICE is still only around 40%, while the remaining stored energy is dissipated through heat and exhaust [16]. The specific fuel oil consummation (SFOC) for a ICE is plotted in figure 3.5 [17], where the color represents different SFOCs for a given engine speed and load. It is observed from the graph that the engines fuel consummation could be improved by adjusting engine speed according to load.

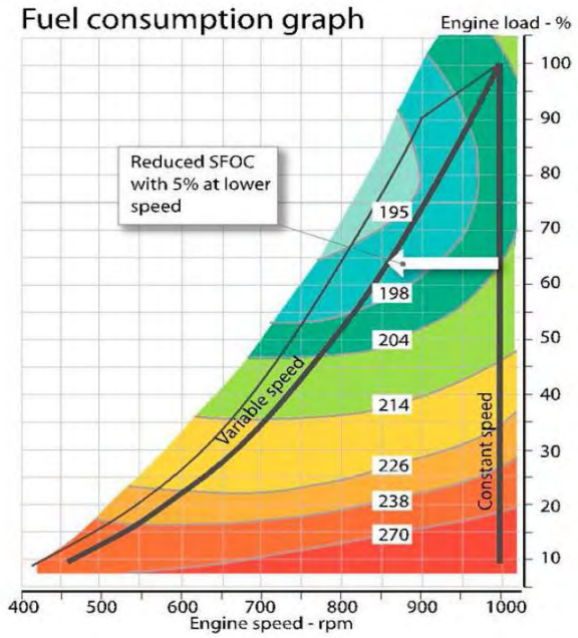

Figure 3.5: ICE fuel consumption

3.4 DC-distribution system

Some attributes of the DC-distribution system are explored in order to establish why this system is emerging as a valid alternative to the AC-distribution system.

3.4.1 Variable prime mover speed

As explore in chapter 3.3, the efficiency of the prime mover is dependent on the engine speed and load. In a classic AC-distribution system, the speed of the prime mover is fixed in order to achieve rated frequency. The implementation of a DC-distribution system removes this dependency.

In a DC-system the prime movers are free to operate at the most fuel-efficient engine speed. Most prime mover has a small window for lowest fuel consummation, typical around 85%, when operation with constant speed. With variable speed this operation window is expended to 50-100% [4]. This is especially beneficial for ships operating in DP, where the average electric thruster load is low. Additional, if the ship is applying a two-split configuration, an increased number of operating gen-sets are necessary to obtain redundancy. A two-split configuration can be observed in figure 3.2, when the bus tie switches is open. This opens the possibility to operate the ship even if one side of the power system fails. However, for the case in figure 3.2, the minimum amount of online gen-sets increased from two to four, operating at low load. The DC-distribution system offers the possibility of reducing the engine speed of all prime movers online, increasing their fuel efficiency.

3.4.2 Weight and space savings

An additional advantage with the DC-power system is the possibility to reduce the footprint of the installation. There are three main sources for space and weight saving:

1. *Generator size*: In conventional AC-systems the pole number and nominal speed of the generator has to be set according to system frequency. In a DC-system, where the system is independent of frequency, the pole numbers of the machine can be chosen more freely. A generator, which in AC-system was design for 60Hz (2-poles), can be replace with an 8-pole machine (240Hz). Machines with higher pole numbers are generally smaller, lighter and less noisy. [18]

2. *Reduced amount of components*: Many key components in the AC-system can be eliminated its DC counterpart. The main AC switchboard is omitted, and circuit breakers and relays are removed. Propulsion and thruster transformers can also be eliminated. [19]

3. *Less conductors*: The DC-system requires one less conductor than the AC-system. Removing a conductor saves space in corridors reserved for power distribution. It is also possible to replace the power cables with DC bus ducts, which is especially beneficial in the zonal topology. Some advantages of the DC bus duct include reduced cross section, no bending radius and improved fire damage resistance. [20]

3.4.3 Energy storage system

Most of the energy storage system (ESS) available are DC-based, which makes it easier and more cost efficient to implement them in an DC-system than in a AC-system with the same functionality[19]. Figure 3.6 [5] shows the difference between implementing a ESS in a AC-system versus a DC-system. The DC-solution requires less equipment than the AC-counterpart, even when converters are used. An ESS can further improve the efficiency of the system. It can deliver power during load steps, removing a constraint from the generator. The ESS can also be utilized instead of spinning reserves. In case of generator tripping, the ESS delivers power to the system until a new gen-set can be brought online, ensuring redundancy.

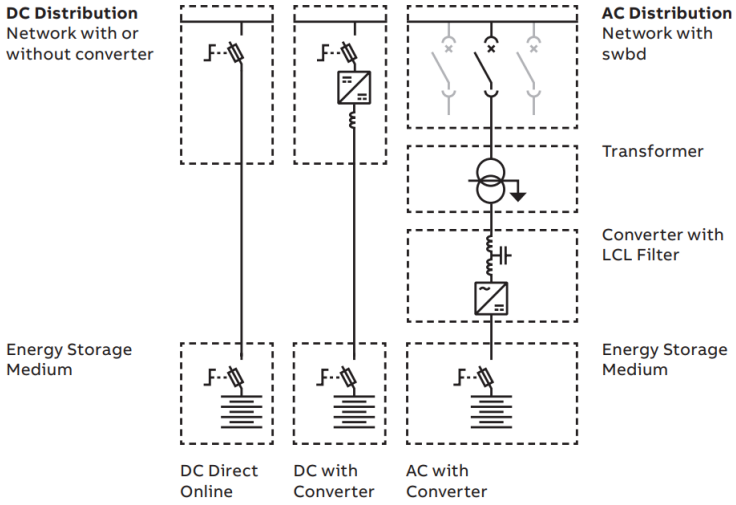

Figure 3.6: Implementation of energy storage system

3.4.4 Parallel connection of generators

The synchronization of generators can be achieved faster in a DC-system than in an AC-system. In an AC-system, frequency, voltage and phase must be synchronized before the generator can be connected to the system. In a DC-system only the voltage needs to be synchronized. A generator (high speed) can then be online in close to 10 seconds in a DC-grid [5].

3.4.5 Voltage levels

Table 3.1 shows IEEE's recommendations for established and potential future MVDC voltage classes [21]. Different sources have looked into the possibility for LVDC (Up to 1000V) [4][19][17]. However, high power system would benefit from the implementation of MVDC, effectively reducing the current in the system [3].

Table 3.1: Recommended MVDC voltage classes

	MVDC Class $[kV]$	Nominal MVDC Class Rated voltage $[kV]$	Maximum MVDC Class Rated voltage $[kV]$
Established	1.5	1.5 ($\pm$0.75)	2 ($\pm$1)
Classes	3	3 ($\pm$1.5)	5 ($\pm$2.5)
	6	6 ($\pm$3)	10 ($\pm$5)
Future	12	12 ($\pm$6)	16 ($\pm$8)
Design	18	18 ($\pm$9)	22 ($\pm$11)
Classes	24	24 ($\pm$12)	28 ($\pm$14)
	30	30 ($\pm$15)	34 ($\pm$17)

3.4.6 Challenges with DC-system

The DC-distribution system has some challenges which must be addressed before the system can truly be a realistic alternative to the AC-systems. It is worth noting that many of these challenges are not due to something inherently wrong with the DC-system, but rather due to it being unproven and underdeveloped compared to AC-systems.

1. *High short-circuit current*: A advantages with AC-system compared to DC-system is the natural occurrence of reactances in the cables, effectively limiting the short-circuit current (SSC). In a system with passive rectification the generators feed into the short-circuit until the fault is cleared. In this scenario the generator impedance is the main limiter of the SSC, which can result in rather large fault currents. [22]

2. *Protection scheme*: The protection scheme in a DC-system is different than in the AC counterpart. The DC-system cannot utilize the zero-crossing of the current, which traditionally is used for AC-systems. The DC-protection scheme relies on a combination of fuses and power-electronic switches. The combination of AC-protection and DC-protection scheme also adds to the complexity. The diode rectifier topology in particular is not easily handled in SC-scenarios [22]. However, if properly coordinated, the DC-protection scheme has the ability to clear faults faster than the AC-protection scheme [20].

3. *Lack of equipment and converters*: The DC-distribution system is underdeveloped compared to the AC-distribution system. As a result, the DC-system lacks in equipment, converters, standardization and coordination, especially for higher voltages ($> 10kV$)[3].

3.5 AC- vs DC control scheme

The differences between the AC- and DC-system control schemes are explored. This includes the control of active power generation and active power sharing when two or more generators are operated in parallel. Some aspects considering reactive power generation are also included.

3.5.1 AC control scheme

Active power control in an AC-system is achieved through frequency considerations. The active power delivered from the prime mover can be written as:

$$p = \tau \cdot n \tag{3.1}$$

Where τ is the torque produced and n is the engine speed, which is proportional to system frequency. I can then be observed that for a given τ, an increase in p would cause the speed to drop. A frequency governor is utilized to regulate prime mover torque with changing power demand in order to keep engine speed, and therefore, system frequency constant. When more than one generator is supplying power to the system, frequency droop is utilized. Frequency droop, presented in figure 3.7 [23], is a control strategy which enables load sharing between generator without the need for communication. The droop curves, S_{p1} and S_{p2}, regulates the individual change in active power produced by the generators based on curve slops. When the generators have stabilized on the new operation point, the nominal frequency can be achieved by changing droop set point. In other word, increasing f_0 and move the curves upwards until nominal frequency is achieved.

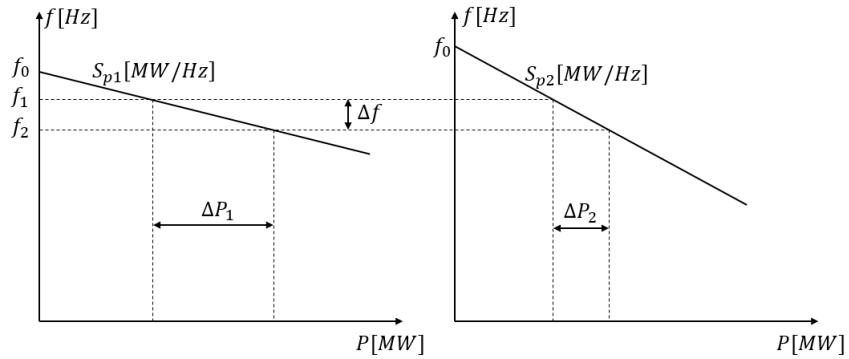

Figure 3.7: Frequency droop

An automatic voltage regulator (AVR) is applied to regulate the voltage. The functions of the AVR includes voltage- and reactive power control and enhancement of system stability. The AVR adjusts the field current of the generator in order to maintain terminal voltage, within the continuous capability of the generator, as the output changes [23]. A concern for shipboard power system is voltage instability, which occurs when the generator hits the reactive power production limit. The dominating load is often induction motor, which consumes reactive power. Also, when the motor accelerates from stand still, the reactive power demand increases. During some cases, this might cause the generator to exceed the capability of reactive power production of the generators [12].

3.5.2 DC control scheme

The speed of the generator, and consequently the frequency on the AC-side of the rectifier, is controlled in order to operate at the prime movers most fuel-efficient speed. It is therefore not possible to utilize frequency governors in this system. The active power control is then realized through DC-link voltage consideration in the DC-system. The DC-link voltage drops with increased active power due to increased voltage losses caused by commutation. An equivalent droop control system can then be realized with voltage instead of frequency. The droop curves are presented in figure 3.8.

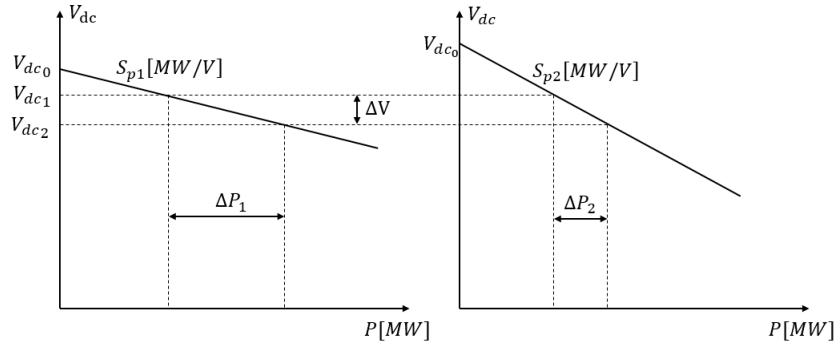

Figure 3.8: Voltage droop

The reactive power production in DC-systems is normally low compared to AC-systems. The reactive power consummation of loads, such as induction motors, are handled by the individual load inverters. The generator only supplies reactive power demand caused by itself and eventual elements between the generator and the rectifier, such as filter.

A voltage controller is applied in order to regulate the DC-link voltage. The voltage is regulated by adjusting the field current of the generator. The following chapters are dedicated to deducing models utilized in design and tuning of these controllers.

Chapter 4

Modeling

This chapter is dedicated to modeling of the system. This includes a model for the synchronous generator, the diode rectifier and the two models combined into one system. All models use a motor reference for both voltages and currents. Large letters represent the physical value of a unit, while small letters represent pu-values.

4.1 Synchronous generator

The model of the synchronous generator is deduced based on [24] [25]. The goal of the modeling is to be able to represent the three-phase generator as a transformed model, where the physical windings are replaced with two fictitious windings fixed according to the rotor. There are two main advantages with such a model. Firstly, the model only has DC-quantities in stationary conditions. Secondly, the transformed model is simpler than the original model, where the inductances in the machine are dependent of the rotors position. The modeling is based on the following assumptions:

- Neglecting magnetic saturation.
- Sinusoidal B-fields.
- Symmetrical windings.
- The actual distributed windings can be represented as concentrated windings.
- Resistances and inductances independent of temperature and frequency.

The basis for the system is a loss-less magnetic storage system. These models are valid if the losses in the system can be represented independent of the storage system. The ohmic losses is then modeled outside the electrical terminals, and the mechanical losses as a part of the load.

4.1.1 The Electrical Equations

A representation of the generator windings based on the previous assumption is shown in figure 4.1 [24]. Six different windings can be observed in the figure. Three in the stator, one for each phase, and three in the rotor. The rotor consists of a field winding and a damper winding, represented in the dq-axis.

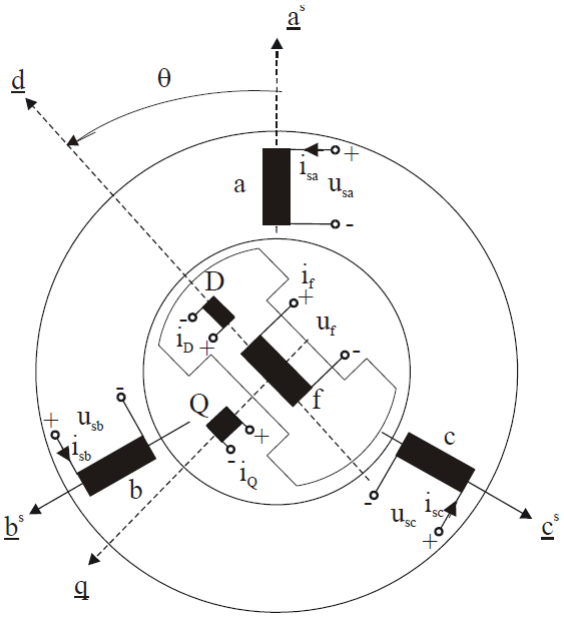

Figure 4.1: Synchronous machine with damper windings

The physical damper winding consist short-circuited bars distributed at the tip of the rotor. These acts similar to a squirrel cage in an asynchronous motor. Rapid load changes cases oscillation in the rotor, resulting in an induced current due to the frequency difference. These current, combined with the B-field, produces a torque opposite to these oscillations. The result is a reduction, or damping, of the oscillations which helps to regain synchronism. The damper winding voltage is equal to zero, due to the short-circuiting of the bars. The voltages in the different phases can then be written as:

$$\begin{aligned} U_{sa} &= R_s \cdot I_{sa} + \frac{d\Psi_{sa}}{dt} & \qquad U_f &= R_f \cdot I_f + \frac{d\Psi_f}{dt} \\ U_{sb} &= R_s \cdot I_{sb} + \frac{d\Psi_{rb}}{dt} & \qquad 0 &= R_D \cdot I_D + \frac{d\Psi_D}{dt} \\ U_{sc} &= R_s \cdot I_{sc} + \frac{d\Psi_{sc}}{dt} & \qquad 0 &= R_Q \cdot I_Q + \frac{d\Psi_Q}{dt} \end{aligned} \tag{4.1}$$

The following is a rewriting of these equations as a matrix to obtain a more compact representation:

$$\underline{U}^{SR} = \mathbf{R}^{SR}\underline{I}^{SR} + \frac{d\underline{\Psi}^{SR}}{dt} \qquad \underline{\Psi}^{SR} = \mathbf{L}^{SR}\underline{I}^{SR} \tag{4.2}$$

The matrix representation of the inductances is presented in equation 4.3. Deducing the different inductances is rather complicated and will not be conducted in this report. However, a short explanation is given on what the different inductances represent and their dependency on the rotor position.

$$\boldsymbol{L}^{SR} = \begin{bmatrix} L_{sa}(\theta) & L_{sasb}(\theta) & L_{sasc}(\theta) & L_{saf}(\theta) & L_{saD}(\theta) & L_{saQ}(\theta) \\ L_{sbsa}(\theta) & L_{sb}(\theta) & L_{sbsc}(\theta) & L_{sbf}(\theta) & L_{sbD}(\theta) & L_{sbQ}(\theta) \\ L_{scsa}(\theta) & L_{scsb}(\theta) & L_{sc}(\theta) & L_{scf}(\theta) & L_{scD}(\theta) & L_{scQ}(\theta) \\ L_{fsa}(\theta) & L_{fsb}(\theta) & L_{scf}(\theta) & L_{f}(\theta) & L_{fD}(\theta) & 0 \\ L_{Dsa}(\theta) & L_{Dsb}(\theta) & L_{Dsc}(\theta) & L_{Df}(\theta) & L_{D}(\theta) & 0 \\ L_{Qsa}(\theta) & L_{Qsb}(\theta) & L_{Qsc}(\theta) & 0 & 0 & L_{Q}(\theta) \end{bmatrix} \tag{4.3}$$

The field and damper winding are mounted on the rotor and rotates accordingly. This results in a constant air gap between these windings and the stator and they are therefore independent of the rotor position. Their self-inductance is the summation of the inductance due to the air gap flux, denoted L_m, and leakage inductance, denoted L_σ. The mutual inductance between the field winding / d-axis damper winding, which has the same orientation, and the q-axis damper winding are equal to zero, since these are perpendicular to each-other.

$$\begin{aligned} L_f &= L_{fm} + L_{f\sigma} & L_{fD} &= L_{Df} \\ L_D &= L_{Dm} + L_{D\sigma} & L_{fQ} &= L_{Qf} = 0 \\ L_Q &= L_{Qm} + L_{D\sigma} & L_{DQ} &= L_{QD} = 0 \end{aligned} \tag{4.4}$$

The stator winding self-inductances is also a summation of an inductance due to the air gap flux and a leakage flux. However, a third term is added to represent the air gaps dependency on the rotors position, denoted L_g. The self-inductance is largest when the rotor is parallel to the windings, and smallest when they are perpendicular. This is due to the inductance being inverse proportional to the air gap. This pattern repeats itself two time for each rotor rotation. Both L_{sm} and L_g are constant and $L_{sm} > L_g$.

$$\begin{aligned} L_{sa}(\theta) &= L_{sm} + L_{s\sigma} + L_g \cdot \cos(2\theta) \\ L_{sb}(\theta) &= L_{sm} + L_{s\sigma} + L_g \cdot \cos\left(2\theta - 240^\circ\right) \\ L_{sc}(\theta) &= L_{sm} + L_{s\sigma} + L_g \cdot \cos\left(2\theta + 120^\circ\right) \end{aligned} \tag{4.5}$$

The mutual inductances between the stator windings are more difficult to comprehend. However, it can be proved that these can be written as in equation 4.6, where $\frac{L_{sm}}{2} > L_g$. The stator windings are shifted 120° relative to each other which results in the mutual inductance between them to be negative. The maximum magnitude of the inductances occurs when the rotor d-axis is midway between the axes of the stator windings.

$$\begin{aligned} L_{sasb} = L_{sbsa} &= -\frac{L_{sm}}{2} + L_g \cdot \cos\left(2\theta - 120^\circ\right) \\ L_{sbsc} = L_{scsb} &= -\frac{L_{sm}}{2} + L_g \cdot \cos(2\theta) \\ L_{sasc} = L_{scsa} &= -\frac{L_{sm}}{2} + L_g \cdot \cos\left(2\theta - 240^\circ\right) \end{aligned} \tag{4.6}$$

The mutual inductance between the field winding and stator windings and d-axis damper winding and stator windings are investigate together, since their positive flux direction is parallel. The positive maximum mutual inductance occurs when the windings positive flux direction is parallel, $\theta = 0^\circ$, and maximum negative when parallel in opposite flux direction, $\theta = 180^\circ$. The mutual inductance is zero when the flux directions are perpendicular, $\theta = 90^\circ$.

$$\begin{aligned} L_{af}(\theta) = L_{fa}(\theta) &= L_{df} \cdot \cos(\theta) \\ L_{bf}(\theta) = L_{fb}(\theta) &= L_{df} \cdot \cos\left(\theta - 120^\circ\right) \\ L_{cf}(\theta) = L_{fc}(\theta) &= L_{df} \cdot \cos\left(\theta - 240^\circ\right) \end{aligned} \tag{4.7}$$

$$\begin{aligned} L_{aD}(\theta) = L_{Da}(\theta) &= L_{dD} \cdot \cos(\theta) \\ L_{bD}(\theta) = L_{Db}(\theta) &= L_{dD} \cdot \cos\left(\theta - 120^\circ\right) \\ L_{cD}(\theta) = L_{Dc}(\theta) &= L_{dD} \cdot \cos\left(\theta - 240^\circ\right) \end{aligned} \tag{4.8}$$

The mutual inductance between the q-axis damper winding and the stator windings are analyzed in a similar fashion. However, a 90° phase shift is included since the q- and d-axis are perpendicular.

$$\begin{aligned} L_{aQ}(\theta) &= L_{Qa}(\theta) = L_{qQ} \cdot \cos(\theta + 90^\circ) = -L_{qQ} \cdot \sin(\theta) \\ L_{bQ}(\theta) &= L_{Qb}(\theta) = L_{qQ} \cdot \cos(\theta - 30^\circ) = -L_{qQ} \cdot \sin(\theta - 120^\circ) \\ L_{cQ}(\theta) &= L_{Qc}(\theta) = L_{qQ} \cdot \cos(\theta - 150^\circ) = -L_{qQ} \cdot \sin(\theta - 240^\circ) \end{aligned} \tag{4.9}$$

4.1.2 dq0-transformation

It is evident from the previous chapter that further modeling with the actual electric equations would be rather complicated. The equations are therefore transformed with the dq0-transformation, or Park/Clark-transformations, to simplify the analysis. The Park and Clark transformation is used together to create a new equivalent two-phase synchronous rotating reference frame.

The stator currents in the machine can be represented with a to-dimensional space vector. However, it can be shown that multiple different combination of the stator currents can produce the same two-dimensional space vector, and therefore a three-dimensional space is needed to obtain a unambiguous solution. A third component is introduced, such that the inverse matrix exists. The third component is chosen as the sum of the stator current, since this is zero for a balanced system.

The goal is to express the coordinate vector α, β and γ in equation 4.11 with the coordinate's vectors a, b and c in equation 4.10. In other words, find the transformation matrix between the coordinate systems. The coordination vectors are then chosen as shown in equation 4.12.

$$\underline{I}_s = \frac{2}{3} \cdot [I_{sa} \cdot \underline{a}^s + I_{sb} \cdot \underline{b}^s + I_{sc} \cdot \underline{c}^s] \tag{4.10}$$

$$\underline{I}_s = \frac{2}{3} \left[I^s_{s\alpha} \cdot \underline{\alpha}^s + I^s_{s\beta} \cdot \underline{\beta}^s + I^s_{s\gamma} \cdot \underline{\gamma}^s \right] \tag{4.11}$$

$$\underline{a}^s = \begin{bmatrix} 1 \\ 0 \\ \frac{1}{2} \end{bmatrix} \qquad \underline{b}^s = \begin{bmatrix} -\frac{1}{2} \\ \frac{\sqrt{3}}{2} \\ \frac{1}{2} \end{bmatrix} \qquad \underline{c}^s = \begin{bmatrix} -\frac{1}{2} \\ -\frac{\sqrt{3}}{2} \\ \frac{1}{2} \end{bmatrix} \tag{4.12}$$

The transformation can be written as in equation 4.13, where $\boldsymbol{T}$ is the well-known Clark transformation matrix. Multiplying and utilize the fact that the sum of currents equal zero result in the equations in expression array 4.14. The inverse Clark matrix is applied in the reversed transformation in equation 4.15, which result in the equations presented in expression array 4.16.

$$\underline{I}^s_{s\alpha\beta\gamma} = \boldsymbol{T} \cdot \underline{I}_{sabc} = \frac{2}{3} \begin{bmatrix} 1 & -\frac{1}{2} & -\frac{1}{2} \\ 0 & \frac{\sqrt{3}}{2} & -\frac{\sqrt{3}}{2} \\ \frac{1}{2} & \frac{1}{2} & \frac{1}{2} \end{bmatrix} \begin{bmatrix} I_{sa} \\ I_{sb} \\ I_{sc} \end{bmatrix} \tag{4.13}$$

$$I^s_{s\alpha} = I_{sa} \qquad I^s_{s\beta} = \frac{\sqrt{3}}{3}\left(I_{sb} - I_{sc}\right) \qquad I^s_{s\gamma} = 0 \tag{4.14}$$

$$\underline{I}_{sabc} = \boldsymbol{T}^{-1} \cdot \underline{I}^s_{s\alpha\beta\gamma} = \begin{bmatrix} 1 & 0 & 1 \\ -\frac{1}{2} & \frac{\sqrt{3}}{2} & 1 \\ -\frac{1}{2} & -\frac{\sqrt{3}}{2} & 1 \end{bmatrix} \begin{bmatrix} I^s_{s\alpha} \\ I^s_{s\beta} \\ I^s_{s\gamma} \end{bmatrix} \tag{4.15}$$

$$I_{sa} = I^s_{s\alpha} \qquad I_{sb} = -\frac{1}{2} I^s_{s\alpha} + \frac{\sqrt{3}}{2} I^s_{s\beta} \qquad I_{sc} = -\frac{1}{2} I^s_{s\alpha} - \frac{\sqrt{3}}{2} I^s_{s\beta} \tag{4.16}$$

The transformed coordinate system is then to be made independent of the rotor position. Figure 4.2 includes the coordinate vector for the stator-, rotor-, and the new coordination system. In this representation, the angle θ is between stator and rotor coordinates, the angle θ_k is between stator and the new system and the angle θ_r is between rotor and the new system. The stator coordinates are then decomposed to the α and β axes, resulting in the equations in expression array 4.17. Introducing the coordinate vectors from expression array 4.12 gives the transformation matrix in 4.18, which is the Park transformation matrix.

$$\begin{aligned} \underline{\alpha}^k =& \frac{2}{3}\left[\cos\left(\theta_k\right) \cdot \underline{a}^s + \cos\left(\theta_k - 120^\circ\right) \cdot \underline{b}^s + \cos\left(\theta_k - 240^\circ\right) \cdot \underline{c}^s\right] \\ \beta^k =& -\frac{2}{3}\left[\sin\left(\theta_k\right) \cdot \underline{a}^s + \sin\left(\theta_k - 120^\circ\right) \cdot \underline{b}^s + \sin\left(\theta_k - 240^\circ\right) \cdot \underline{c}^s\right] \\ \gamma^k =& \frac{1}{3}\left[\underline{a}^s + \underline{b}^s + \underline{c}^s\right] \end{aligned} \tag{4.17}$$

$$\begin{bmatrix} \alpha^k \\ \beta^k \\ \gamma^k \end{bmatrix} = \begin{bmatrix} \cos(\theta) & \sin(\theta) & 0 \\ -\sin(\theta) & \cos(\theta) & 0 \\ 0 & 0 & 1 \end{bmatrix} \tag{4.18}$$

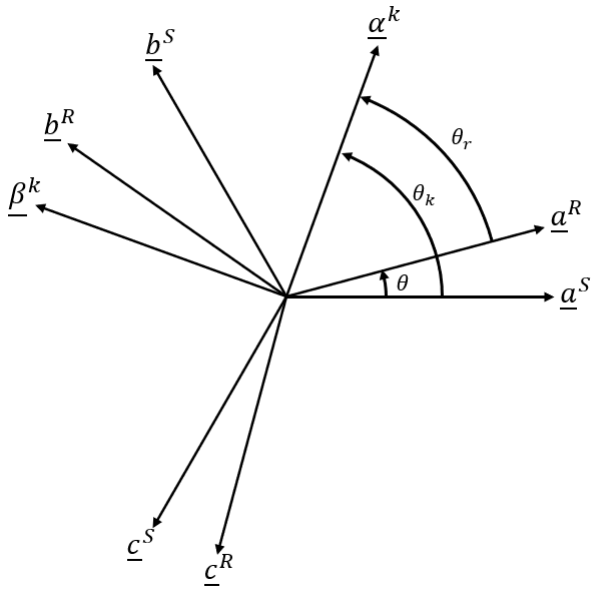

Figure 4.2: Transformation between coordinate systems

The transformation matrix is deduced by expressing the new coordinate vectors with regard to the old. The result is presented in equation 4.19. This matrix is proven to be a combination of the Clarke and Park transformation, which is defined as the dq0-transformation matrix. The inverse dq0-transformation matrix is shown in equation 4.20.

$$\mathbf{T}_{ss}^{k} = \frac{2}{3}\begin{bmatrix} \cos(\theta_k) & \cos(\theta_k - 120°) & \cos(\theta_k - 240°) \\ -\sin(\theta_k) & -\sin(\theta_k - 120°) & -\sin(\theta_k - 240°) \\ \frac{1}{2} & \frac{1}{2} & \frac{1}{2} \end{bmatrix} \tag{4.19}$$

$$\mathbf{T}_{ss}^{-k} = \begin{bmatrix} \cos(\theta_k) & -\sin(\theta_k) & 1 \\ \cos(\theta_k - 120°) & -\sin(\theta_k - 120°) & 1 \\ \cos(\theta_k - 240°) & -\sin(\theta_k - 240°) & 1 \end{bmatrix} \tag{4.20}$$

The same procedure can be applied for the rotor windings. This results in the same transformation matrix as for the stator reference frame:

$$\mathbf{T}_{ss}^{k} = \mathbf{T}_{rr}^{k} \qquad \mathbf{T}_{ss}^{-k} = \mathbf{T}_{rr}^{-k} \tag{4.21}$$

The total transformation matrix can be written as:

$$\mathbf{T}^k = \begin{bmatrix} \mathbf{T}_{ss}^k & \mathbf{0} \\ \mathbf{0} & \mathbf{T}_{rr}^k \end{bmatrix} \qquad \mathbf{T}^{-k} = \begin{bmatrix} \mathbf{T}_{ss}^{-k} & \mathbf{0} \\ \mathbf{0} & \mathbf{T}_{rr}^{-k} \end{bmatrix} \tag{4.22}$$

The new coordinate system is still referred to the arbitrary position α^k. A special case occurs for the synchronous machine since θ_k is set equal to θ. This results in the physical rotor windings occurring in the transformed model. The total transformation matrices can then be written as:

$$\mathbf{T}^r = \begin{bmatrix} \mathbf{T}_{ss}^r & \mathbf{0} \\ \mathbf{0} & \mathbf{I} \end{bmatrix} \quad \mathbf{T}^{-r} = \begin{bmatrix} \mathbf{T}_{ss}^{-r} & \mathbf{0} \\ \mathbf{0} & \mathbf{I} \end{bmatrix} \quad \mathbf{T}_{rr}^r = \mathbf{I} = \begin{bmatrix} 1 & 0 & 0 \\ 0 & 1 & 0 \\ 0 & 0 & 1 \end{bmatrix} \tag{4.23}$$

4.1.3 Transformation of the electrical equations

The electrical equations are transformed to the new reference frame by applying equation 4.23 on equation 4.2, which result in the following equations:

$$\underline{U}^r = \mathbf{T}^r \cdot \underline{U}^{SR} \tag{4.24}$$

$$\begin{aligned} \underline{\Psi}^r &= \mathbf{T}^r \cdot \underline{\Psi}^{SR} & \underline{\Psi}^{SR} &= \mathbf{T}^{-r} \cdot \underline{\Psi}^r \\ \underline{I}^r &= \mathbf{T}^r \cdot \underline{I}^{SR} & \underline{I}^{SR} &= \mathbf{T}^{-r} \cdot \underline{I}^r \end{aligned} \tag{4.25}$$

The voltage vectors in the new rotor-oriented reference are presented in equation 4.26. The matrices and vectors included in the voltage matrix is presented in expression array 4.27.

$$\underline{U}^r = \mathbf{R}^r \underline{I}^r + \frac{d\underline{\Psi}^r}{dt} + \omega \cdot \mathbf{J}\underline{\Psi}^r \tag{4.26}$$

$$\begin{aligned} \mathbf{J} &= \mathbf{T}^r \frac{d\mathbf{T}^{-r}}{d\theta} & \mathbf{R}^r &= \mathbf{T}^r \mathbf{R}^{RS} \mathbf{T}^{-r} \\ \underline{\Psi}^r &= \mathbf{L}^r \underline{I}^r & \mathbf{L}^r &= \mathbf{T}^r \mathbf{L}^{RS} \mathbf{T}^{-r} \end{aligned} \tag{4.27}$$

The voltages, currents and fluxes present in the new transformed model is presented in expression array 4.28.

$$U^r = \begin{bmatrix} U_d \\ U_q \\ U_0 \\ U_f \\ U_D \\ U_Q \end{bmatrix} \qquad I^{r=} \begin{bmatrix} I_d \\ I_q \\ I_0 \\ I_f \\ I_D \\ I_Q \end{bmatrix} \qquad \psi^r = \begin{bmatrix} \Psi_d \\ \Psi_q \\ \Psi_0 \\ \Psi_f \\ \Psi_D \\ \Psi_Q \end{bmatrix} \tag{4.28}$$

It is evident from transformed inductance matrix presented equation 4.29 that the main goals of the transformation have been achieved. The model only consists of DC-quantities, since the reference frame is rotating synchronous with the rotor. It is also evident from equation 4.29 that the inductances are independent of the rotor angle and are generally simpler due to the zero elements. However, due to the $\frac{3}{2}$ factor from the Clark transformation, the matrix is not symmetrical. This is dealt with when converting to pu-values.

$$\mathbf{L}^r = \begin{bmatrix} L_d & 0 & 0 & L_{df} & L_{dD} & 0 \\ 0 & L_q & 0 & 0 & 0 & L_{qQ} \\ 0 & 0 & L_{s\sigma} & 0 & 0 & 0 \\ \frac{3}{2}L_{df} & 0 & 0 & L_f & L_{fD} & 0 \\ \frac{3}{2}L_{dD} & 0 & 0 & L_{fD} & L_D & 0 \\ 0 & \frac{3}{2}L_{qQ} & 0 & 0 & 0 & L_Q \end{bmatrix} \tag{4.29}$$

$$L_d = \frac{3}{2} \cdot (L_{sm} + L_g) + L_{s\sigma} \qquad L_q = \frac{3}{2} \cdot (L_{sm} - L_g) + L_{s\sigma} \tag{4.30}$$

It can be observed from expression array 4.30 that some magnetic connections occur:

- Between the d-axis stator winding and the d-axis damper winding
- Between the stator winding and field winding
- Between the q-axis stator winding and the q-axis damper winding

The transformed resistance matrix $\mathbf{R}^r$ and the previous applied matrix $\mathbf{J}$ are presented in equation 4.31.

$$\mathbf{R}^r = \begin{bmatrix} R_s & 0 & 0 & 0 & 0 & 0 \\ 0 & R_s & 0 & 0 & 0 & 0 \\ 0 & 0 & R_s & 0 & 0 & 0 \\ 0 & 0 & 0 & R_f & 0 & 0 \\ 0 & 0 & 0 & 0 & R_D & 0 \\ 0 & 0 & 0 & 0 & 0 & R_Q \end{bmatrix} \quad \mathbf{J} = \begin{bmatrix} 0 & -1 & 0 & 0 & 0 & 0 \\ 1 & 0 & 0 & 0 & 0 & 0 \\ 0 & 0 & 0 & 0 & 0 & 0 \\ 0 & 0 & 0 & 0 & 0 & 0 \\ 0 & 0 & 0 & 0 & 0 & 0 \\ 0 & 0 & 0 & 0 & 0 & 0 \end{bmatrix} \tag{4.31}$$

4.1.4 Per unit values

The model is converted to pu values to further simplify the model. As mentioned above, the reactance matrix should be symmetrical when in pu-quantities and the base values are chosen accordingly. The following criteria should be fulfilled:

- All diagonal elements should be written either as x_{md}, for the d-axis, or x_{mq}, for the q-axis, in addition to a leakage reactance.
- All off-diagonal elements are written as either x_{md} or x_{mq}.

The reactance matrix is therefore written as:

$$\boldsymbol{x}^r = \begin{bmatrix} x_{md} + x_{s\sigma} & 0 & 0 & x_{md} & x_{md} & 0 \\ 0 & x_{mq} + x_{s\sigma} & 0 & 0 & 0 & x_{mq} \\ 0 & 0 & x_{s\sigma} & 0 & 0 & 0 \\ x_{md} & 0 & 0 & x_{md} + x_{f\sigma} & x_{md} & 0 \\ x_{md} & 0 & 0 & x_{md} & x_{md} + x_{D\sigma} & 0 \\ 0 & x_{mq} & 0 & 0 & 0 & x_{mq} + x_{Q\sigma} \end{bmatrix} \tag{4.32}$$

$$x_{md} = \frac{3}{2} \cdot \frac{(L_{sm} + L_g) \cdot \omega_n \cdot \hat{I}_n}{\hat{U}_n} \qquad x_{mq} = \frac{3}{2} \cdot \frac{(L_{sm} - L_g) \cdot \omega_n \cdot \hat{I}_n}{\hat{U}_n} \tag{4.33}$$

The stator voltage and current are chosen as the peak value of their respected unit. The basis for the mutual inductances is chosen such that the pu-value of the inductances and reactances are equal. This will in principle be the same for each individual winding.

$$I_{s,basis} = \hat{I}_n \qquad U_{s,basis} = \hat{U}_n \qquad \Psi_{s,basis} = \frac{\hat{U}_n}{\omega_n} \tag{4.34}$$

The pu-values for the rotor are chosen to fulfill the above-mentioned criteria for the reactance matrix. These, along with the power and torque bases, are presented in [24]. The complete equations for the transformed model with pu-representation are presented below:

$$\begin{aligned} u_d &= r_s \cdot i_d + \frac{1}{\omega_n}\frac{d\psi_d}{dt} - n \cdot \psi_q & 0 &= r_D \cdot i_D + \frac{1}{\omega_n}\frac{d\psi_D}{dt} \\ u_q &= r_s \cdot i_q + \frac{1}{\omega_n}\frac{d\psi_q}{dt} + n \cdot \psi_d & 0 &= r_Q \cdot i_Q + \frac{1}{\omega_n}\frac{d\psi_Q}{dt} \\ u_f &= r_f \cdot i_f + \frac{1}{\omega_n}\frac{d\psi_f}{dt} & u_0 &= r_s \cdot i_0 + \frac{1}{\omega_n}\frac{d\psi_0}{dt} \end{aligned} \tag{4.35}$$

$$\begin{aligned} \psi_d &= x_d \cdot i_d + x_{md} \cdot i_f + x_{md} \cdot i_D & \psi_D &= x_{md} \cdot i_d + x_{md} \cdot i_f + x_D \cdot i_D \\ \psi_q &= x_q \cdot i_q + x_{mq} \cdot i_Q & \psi_Q &= x_{mq} \cdot i_q + x_Q \cdot i_Q \\ \psi_0 &= x_{s\sigma} \cdot i_0 & \psi_f &= x_{md} \cdot i_d + x_f \cdot i_f + x_{md} \cdot i_D \end{aligned} \tag{4.36}$$

$$\begin{aligned} x_d &= x_{md} + x_{s\sigma} & x_D &= x_{md} + x_{D\sigma} \\ x_q &= x_{mq} + x_{s\sigma} & x_Q &= x_{mq} + x_{Q\sigma} \\ x_f &= x_{md} + x_{f\sigma} \end{aligned} \tag{4.37}$$

$$\tau_e = \psi_d \cdot i_q - \psi_q \cdot i_d \tag{4.38}$$

4.1.5 Block diagram for the generator

The equations established in the previous sections is normally transformed to investigate non-stationary processes for the synchronous machine [26]. The currents occurring in the damper windings are usually of no interest, and it is therefore convenient to eliminate them from the system. The transformation also introduces the characteristic constant of the synchronous machine, namely the subtransient-, transient and synchronous reactance and their respected time constants. Linear equations exist between the previous mentioned magnetic connections for the damper windings and the field winding. These equations can therefore be solved with the aid of Laplace transformation. This involves complicated mathematical evaluations, which is conducted in [26]. The result, with pu-values chosen according to chapter 4.1.4 is presented in [24]. It should be mentioned that the functions presented below is based on a simplification involving the elimination of the smallest time constants.

$$\begin{aligned} u_d(s) =& r_s \cdot i_d(s) + \frac{s}{\omega_n}\psi_d(s) - n \cdot \psi_q(s) \\ u_q(s) =& r_s \cdot i_q(s) + \frac{s}{\omega_n}\psi_q(s) + n \cdot \psi_d(s) \\ u_f(s) =& r_f \cdot i_f(s) + \frac{s}{\omega_n} \cdot \psi_f(s) \end{aligned} \tag{4.39}$$

It can be shown after some extensive calculations, eliminations and simplification, that the mutual fluxes can be written as:

$$\psi_q(s) = i_q(s) \cdot x_q(s) \tag{4.40}$$

$$\psi_d(s) = \frac{\omega_n \cdot T'_{d0}}{1 + T'_{d0} \cdot s} \cdot \frac{x_d - x'_d}{x_{md}} \cdot u_f(s) + i_d(s) \cdot x_d(s) \tag{4.41}$$

Which includes the following transfer functions:

$$x_d(s) = \frac{(1 + T'_d \cdot s) \cdot (1 + T''_d \cdot s)}{(1 + T'_{d0} \cdot s) \cdot (1 + T''_{d0} \cdot s)} \cdot x_d \tag{4.42}$$

$$x_q(s) = \frac{1 + T''_q \cdot s}{1 + T''_{q0} \cdot s} \cdot x_q \tag{4.43}$$

The field current in the machine is one of the regulation parameters. The field current is therefore solved as a function of the field voltage:

$$i_f(s) = \frac{\omega_n \cdot T'_{d0}}{1 + T'_{d0} \cdot s} \cdot \frac{x_d - x'_d}{x^2_{md}} \cdot u_f(s) - \frac{s \cdot T'_{d0}}{1 + T'_{d0}} \cdot \frac{x_d - x'_d}{x_{md}} \cdot i_d(s) \tag{4.44}$$

It can be observed from equation 4.44 that the field current is a function of the field voltage and the d-axis current. However, the d-axis current only has influence during transient stage. The field current is solely dependent on the field voltage in steady state.

The block-diagram for the synchronous machine can then be drawn based on the equation deduced in this chapter:

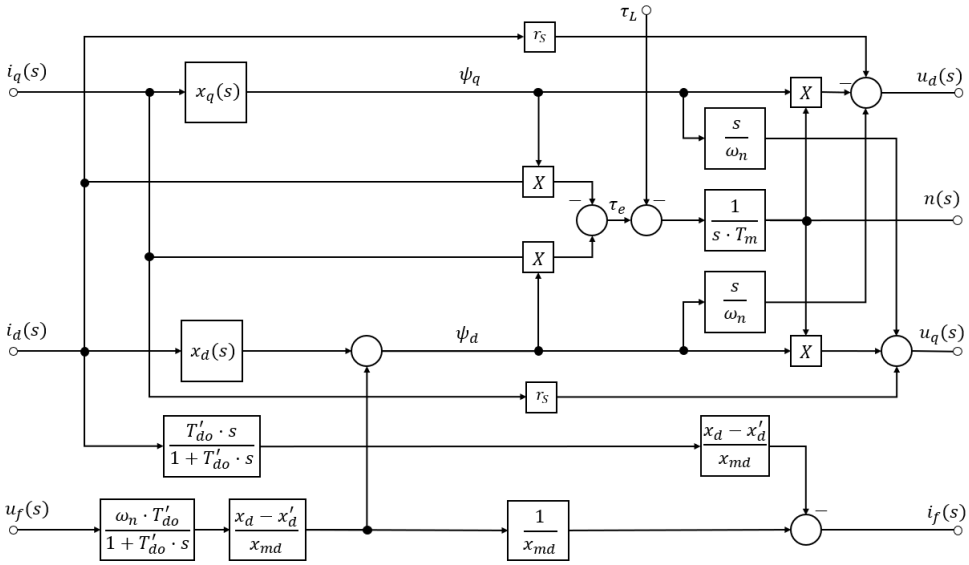

Figure 4.3: Block diagram for the synchronous machine

4.1.6 Stationary operation

The stationary characteristics of the synchronous machine is investigated. These characteristics is used to determine the reference values for the control system. In steady state the flux linkages remain constant, which results in the time derivatives of these fluxes to be equal zero. The voltages from expression array 4.35 then becomes:

$$u_d = r_s \cdot i_d - n \cdot \psi_q \qquad u_q = r_s \cdot i_q + n \cdot \psi_d \qquad u_f = r_f \cdot i_f \tag{4.45}$$

It can also be observed from expression array 4.35 that both the d-axis and q-axis damper winding current is equal to zero. This conclusion can also be drawn based on the fact that there are no oscillations of the rotor in steady state. The d- and q-axis fluxes from expression array 4.36 then becomes:

$$\psi_q = x_q \cdot i_q \qquad \psi_d = x_d \cdot i_d + x_{md} \cdot i_f \tag{4.46}$$

Inserting for the fluxes in equation 4.45 from equation 4.46 yields:

$$u_d = r_s \cdot i_d - n \cdot x_q \cdot i_q \qquad u_q = r_s \cdot i_q + n \cdot x_d \cdot i_d + n \cdot x_{md} \cdot i_f \tag{4.47}$$

An example vector diagram for a motor-operation of the synchronous machine is then presented in figure 4.4. The power angle δ and the power factor angle ϕ, which in this case is negative due to capacitive operation, is also included.

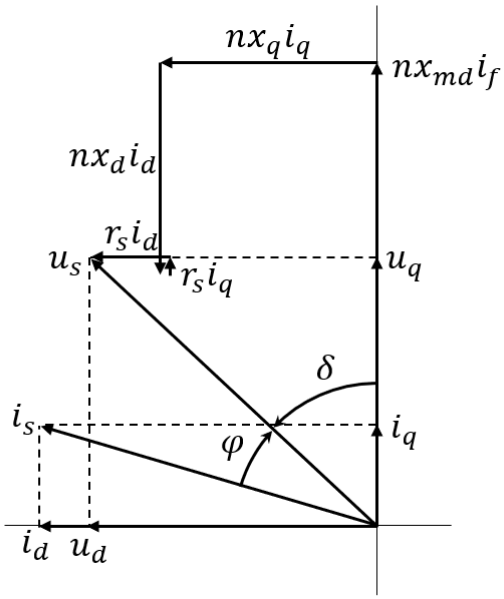

Figure 4.4: generator vector diagram

The voltage and current can be decomposed along the d- and q-axis:

$$\begin{aligned} u_d &= -\,u_s \cdot \sin(\delta) & u_q &= u_s \cdot \cos(\delta) \\ i_d &= -\,i_s \cdot \sin(\delta - \varphi) & i_q &= i_s \cos(\delta - \varphi) \end{aligned} \tag{4.48}$$

The stator voltage in steady state can be calculated as following:

$$\begin{aligned} \underline{u}_s &= r_s \cdot \underline{i}_s + \frac{d\underline{\psi}_s}{dt} \\ &= r_s \cdot \underline{i}_s + j\left(f_s \cdot \underline{\psi}_s\right) \\ &= r_s \cdot \underline{i}_s + j \cdot n \cdot \underline{\psi}_s \end{aligned} \tag{4.49}$$

The operation ranges of a synchronous machine as a function of the power factor angle φ are shown in figure 4.5. Based on chapter 2.3, it can be concluded that the machine in this system would operate in the third quadrant. The machine is supplying active power to the DC-power and producing enough reactive power to suffice the AC-side reactances.

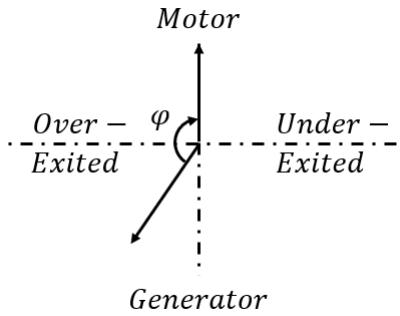

Figure 4.5: Operation range of the synchronous machine as a function of power factor angle φ

4.2 Diode rectifier

The modeling of the diode rectifier, which was analyzed in the specialization project, was summarized in chapter 2.1-2.4. It was concluded in the project report that the constant current model was a good representation of the large capacitor DC-link setup. It was also determined that the first harmonic component of the current was a good representation of the phase current, except at low load. These justifications are applied in further modeling of the diode rectifier. The models presented in this chapter are based on the work in chapter 6 of [24] and chapter 3 in [26].

4.2.1 Average rectifier model

It is sufficient, for the control purpose of the system, to apply the average model of the rectifier. The models presented in this chapter is based on the work in chapter 6.2.3 of [24]. The harmonics of the voltage and the current are neglected and only the corresponding average values are considered. Figure 4.6 shows the equivalent circuit diagram for this model.

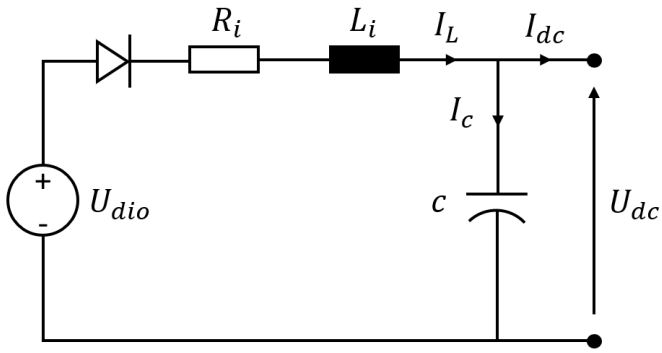

Figure 4.6: Average rectifier model

The voltage U_{dio} is represented by an ideal voltage source in the equivalent circuit. The reduced voltage due to the commutation is modeled as a resistance R_i. It is worth noting that this a fictional resistance, which does not produce heat. It should not be included in loss calculating.

When the dynamic behaviour of the rectifier is analyzed the inductance L_i and the capacitance C must be taken into account. It can be observed from figure 2.1 that in the normal case of two diodes conducting current, the inductance is equal $2L_s$. While during commutation, when three diodes are conducting current, the total inductance is equal $\frac{3}{2}L_s$. This is because the two phases commutating are conducting in parallel. However, the commutation period is assumed relative short compared to the total commutation interval and is therefore neglected in the average model. Finally, a diode is included to complete the model. The diode indicates that the rectifier only can conduct current in forward direction.

The DC-link voltage equation is then written as:

$$U_{dc} = U_{dio} + U_{dk} \tag{4.50}$$

$$U_{dio} = \frac{3\sqrt{2}}{\pi} \cdot U_s \qquad\qquad U_{dk} = -\frac{3}{\pi}\omega L_i \cdot I_L \tag{4.51}$$

It can be observed that equation 4.50 is equivalent to equation 2.1, with the exception of the line-to-line voltage denoted as U_s. Based on the analysis above, the expressions for the equivalent resistance and the inductance is given as:

$$R_i = \frac{3}{\pi}\omega L_s \qquad\qquad L_i = 2L_s \tag{4.52}$$

The equation for the dynamic behavior of the rectifier is evaluated using kirchhoff's voltage law (KVL). The resulting equation is presented equation 4.53, where the dynamic behavior of the capacitor is described by equations 4.54.

$$U_{dc}(t) = U_{dio} - R_i \cdot I_L(t) - L_i \cdot \frac{dI_L(t)}{dt} \tag{4.53}$$

$$I_L - I_{dc} = C \cdot \frac{d}{dt}U_{dc} \tag{4.54}$$

4.2.2 Rectifier model with generator reference

The topology of the three-phase diode rectifier is similar to figure 2.1 in chapter 2.1, with some different terms. The generator leakage inductance L_σ is introduced in addition to the arbitrary inductance L_f. The inductances L_f could for instance be cable- or filter inductances. This inductance can in many cases be assumed zero. It is important to note that the generator leakage inductance should only be included in commutation voltage loss considerations. The dynamic behaviour is included in the generator model.

The stator currents are defined toward the source voltages, due to the motor reference applied in the modeling. In this system the synchronous machine is operated as a generator, which results in negative stator currents. Three current, i_{ga}, i_{gb} and i_{gc}, are therefore introduced and are defined as the negative stator currents. These correlates to the currents i_a, i_b and i_c from figure 2.1. These currents are used in further calculations, which makes it possible to utilize the expressions in chapter 2.1-2.4.

The term intermediate circuit is introduced, which is defined as the rectifier part of the system. In other word the rectifier model without the dc-link capacitor. The current in the intermediate circuit is denoted as I_z. The resulting model is presented in figure 4.7.

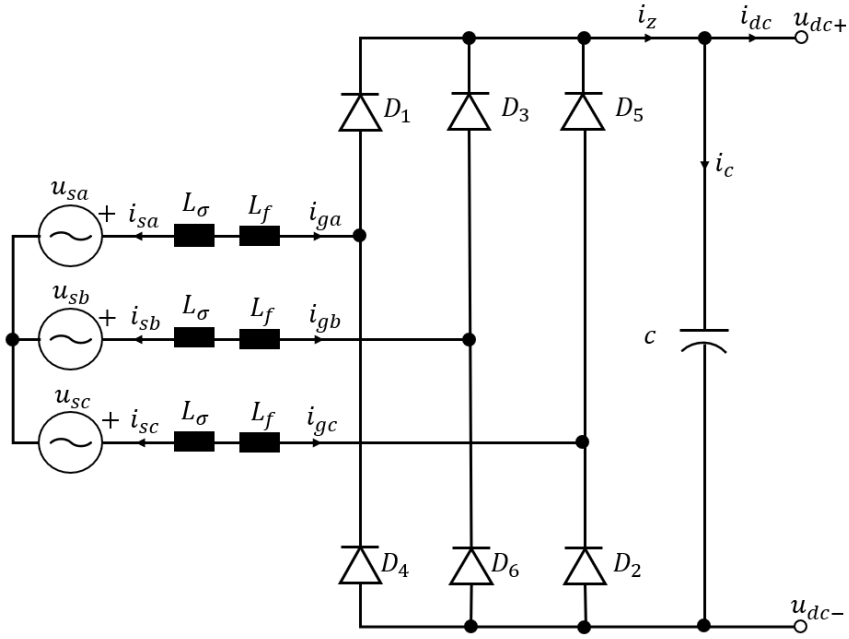

Figure 4.7: Rectifier model with generator reference

Per unit values

The DC-link voltage equations, presented in equation 4.50 and 4.51, are rewritten to include the new notation. Additionally, the line-to-line voltage are replaced with the peak value of the terminal voltage of the generator, denoted $\hat{U}_y$. The inductance L_i is defined as the sum of the inductances in figure 4.7.

$$\begin{aligned} U_{dc} &= U_{dio} + U_{dk} & \qquad U_{dio} &= \frac{3\sqrt{3}}{\pi} \cdot \hat{U}_y \\ U_{dk} &= -\frac{3}{\pi}\omega L_i \cdot I_z & \qquad L_i &= L_s + L_\sigma \end{aligned} \tag{4.55}$$

The base values for the rectifier model are chosen such that the per unit values of the rectifier corresponds with the generator's per unit values. The base voltage for the rectifier, denoted as U_{br}, is therefore set as following:

$$U_{br} = \frac{3\sqrt{3}}{\pi} \cdot \hat{U}_n \tag{4.56}$$

The per unit value for the rectifier voltage is calculated as:

$$u_{dio} = \frac{U_{dio}}{U_{br}} = \frac{\frac{3\sqrt{3}}{\pi} \cdot \hat{U}_y}{\frac{3\sqrt{3}}{\pi} \cdot \hat{U}_n} = \frac{\hat{U}_y}{\hat{U}_n} = u_s \tag{4.57}$$

Where u_s is the generator stator voltage in per unit.

The same procedure is repeated for the current. The relationship between the stator current and the intermediate current was explored in chapter 2.3. It was determined that the first harmonic of the current was an accurate representation of the stator current in normal operation areas. Rewriting equations 2.3 with regards to the intermediate current results in:

$$I_z = \frac{\pi}{2\sqrt{3}} \cdot \hat{I}_{g1} \tag{4.58}$$

Based on equation 4.58 the rectifier base current I_{br} is chosen as:

$$I_{br} = \frac{\pi}{2\sqrt{3}} \cdot \hat{I}_n \tag{4.59}$$

The per unit current for the intermediate circuit can then be calculated:

$$i_z = \frac{I_z}{I_{br}} = \frac{\frac{\hat{I}_{g_1} \cdot \pi}{2\sqrt{3}}}{\frac{\pi}{2 \cdot \sqrt{3}} \cdot \hat{I}_n} = \frac{\hat{I}_{g_1}}{\hat{I}_n} \tag{4.60}$$

Equation 4.57 for the rectifier voltage and equation 4.60 for intermediate current is compared to the base values of the generator defined in chapter 4.1.4, equation 4.34. It can be determined, based on these equations, that the terminal voltage of the generator is equal to the rectifier voltage in per unit. Additionally, the intermediate current is equal to the first harmonic of the generator's stator current in per unit. Finally, the per unit voltage-loss is calculated from the equation for U_{dk} in expression array 4.55. The result is presented in equation array 4.61. The base values from equation 4.56 and 4.59 are introduced in the second calculation. In the third calculation the relation $\omega = f \cdot \omega_n$ is introduced, where f is the generator frequency in per unit.

$$\begin{aligned} u_{dk} \cdot U_{br} &= -\frac{3}{\pi} \cdot \omega L_i \cdot i_z \cdot I_{br} \\ u_{dk} &= -\frac{3}{\pi} \cdot \omega L_i \cdot \frac{I_{br}}{U_{br}} \cdot i_z \\ &= -\frac{\pi}{6} \cdot \omega_n \cdot f \cdot L_i \cdot \frac{\hat{I}_n}{\hat{U}_n} \cdot i_z \\ &= -\frac{\pi}{6} x_i \cdot f \cdot i_z \end{aligned} \tag{4.61}$$

The reactance x_i are given by the following equations:

$$x_i = x_\sigma + x_f \tag{4.62}$$

Where the leakage inductance and line inductance are given by:

$$x_\sigma = \omega_n L_\sigma \cdot \frac{\hat{I}_n}{\hat{U}_n} \qquad\qquad x_f = \omega_n L_s \cdot \frac{\hat{I}_n}{\hat{U}_n} \tag{4.63}$$

The leakage reactance, or commutation reactance, of the generator change during commutation [27]. A representation of the reactance by a value in the middle of the commutation interval is given as:

$$x_\sigma = \frac{x''_d + x''_q}{2} + \frac{x''_d - x''_q}{2} \cdot \cos(2\delta + \mu) \tag{4.64}$$

Which, if the dependency on the power angle and commutation is neglected, simply can be written as:

$$x_\sigma = \frac{x''_d + x''_q}{2} \tag{4.65}$$

Including the angular frequency dependency

The relation between the stator voltage and the angular frequency is presented equation 4.49. If the stator resistance is assumed zero, the following equation occurs for the absolute value:

$$u_s = n \cdot \psi_s \tag{4.66}$$

The commutation interval in equation 2.2 is converted to per unit values in equation array 4.67. The generator peak terminal voltage is introduced instead of the line-to-line voltage. The generator stator voltage in per unit, presented in equation 4.57, and the per unit current from equation 4.59 are introduced in the second calculation. The term ω_n/ω_n is added in the fourth calculation such that the reactance x_i can be included and make it possible to utilize the relation $n = \omega/\omega_n$.

$$\begin{aligned}
\cos(\mu) &= 1 - \frac{2 \cdot L_i \cdot \omega}{\sqrt{3} \cdot \hat{U}_y} \cdot I_z \\
&= 1 - \frac{2 \cdot \omega L_i}{\sqrt{3} \cdot \hat{U}_n \cdot u_s} i_z \cdot I_{br} \\
&= 1 - \frac{2 \cdot \omega L_i}{\sqrt{3} \cdot \hat{U}_n \cdot u_s} \cdot i_z \cdot \frac{\pi}{2\sqrt{3}} \cdot \hat{I}_n \\
&= 1 - \frac{\omega}{u_s} \frac{\omega_n}{\omega_n} \cdot \frac{\pi}{3} i_z \cdot \frac{\hat{I}_n}{\hat{U}_n} \cdot L_i \\
&= 1 - \frac{n}{u_s} \cdot \frac{\pi}{3} \cdot i_z \cdot x_i
\end{aligned} \tag{4.67}$$

Applying the relation from equation 4.66 results in the result from equation array 4.67 yield the following expression:

$$\cos(\mu) = 1 - \frac{\pi \cdot x_i}{3 \cdot \psi_s} i_z \tag{4.68}$$

It can be observed from equation 4.68 that the commutation interval is independent of the angular frequency. It should be notated that at low frequencies, the influence of the ohmic resistance in the generator cannot be neglected. However, it is in this model assumed that the angular frequency is never reduced to a level where the resistance becomes significant.

Average model of the intermediate circuit

An average model for the intermediate circuit is developed based on the same principles as in chapter 4.2.1. The equivalent circuit is presented in figure 4.8.

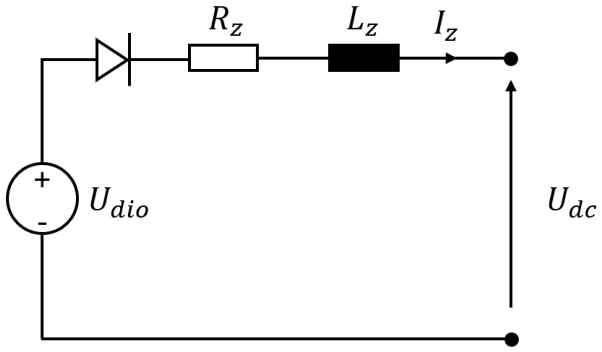

Figure 4.8: Equivalent circuit of the intermediate circuit

Applying KVL on the circuit in figure 4.8 results in the following equation:

$$-U_{dio} + R_z \cdot I_z + L_z \cdot \frac{d}{dt} I_z + U_{dc} = 0 \tag{4.69}$$

Equation 4.69 is restructured to include pu-values in equation array 4.70.

$$\begin{aligned} u_{dio} \cdot U_{br} - u_{dc} \cdot U_{br} =& R_z \cdot i_z \cdot I_{br} + L_z \cdot \frac{d}{dt} i_z \cdot I_{br} \\ u_{dio} - u_{dc} =& r_z \cdot i_z + r_z \cdot T_z \cdot \frac{d}{dt} i_z \end{aligned} \tag{4.70}$$

Equation 4.70 consist of the new intermediate resistance r_z. The variable r_z is the voltage reduction caused by the commutation, which was evaluated in equation 4.61. This resistance is calculated as following:

$$r_z = \frac{\pi}{6} x_i \cdot f \tag{4.71}$$

The time constant T_z of the system is calculated in equation array 4.72. The intermediate resistance is inserted in per unit, given in equation 4.71. The base values I_{br} and U_{br} from equation 4.59 and 4.56 respectively are inserted in the second calculation. The term ω_n/ω_n is also introduced such that the reactance x_z can be included.

$$\begin{aligned} T_z =& \frac{L_z}{R_z} = \frac{1}{r_z} \cdot L_z \cdot \frac{I_{br}}{U_{br}} \\ =& \frac{1}{\frac{\pi}{6} \cdot x_i f} \cdot \frac{\pi^2}{18} \cdot \frac{\hat{I}_n}{\hat{U}_n} \cdot \frac{\omega_n}{\omega_n} \cdot L_z \\ =& \frac{\pi}{3} \cdot \frac{x_z}{\omega_n x_i f} \end{aligned} \tag{4.72}$$

Where the intermediate reactance ans inductance is given as following:

$$x_z = \omega_n L_z \cdot \frac{\hat{I}_n}{\hat{U}_n} \qquad\qquad L_z = 2 \cdot L_s \tag{4.73}$$

4.2.3 Block diagrams for the rectifier and capacitor

The circuit diagram for the intermediate circuit in figure 4.8 are redrawn to include the intermediate circuit time constant and the DC-link capacitor. The result is presented in figure 4.9. Block diagrams for the two models can then be constructed.

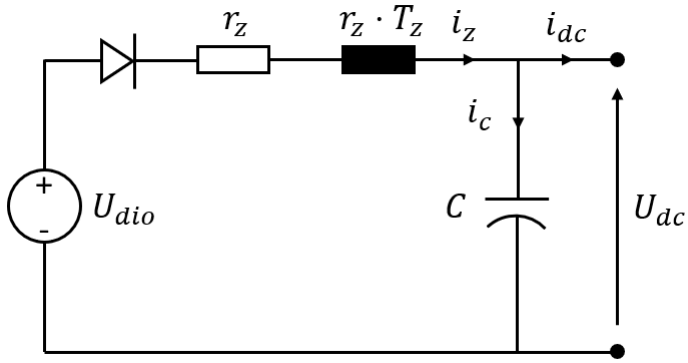

Figure 4.9: Circuit diagram for the rectifier including the intermediate circuit time contestant

Intermediate circuit

Equation 4.70 is isolated for the derivative of the intermediate current:

$$r_z \cdot T_z \cdot \frac{d}{dt} i_z = u_{dio} - u_{dc} - r_z \cdot i_z \tag{4.74}$$

Substituting T_z and r_z with equation 4.72 and 4.71 gives the following expression:

$$\frac{x_{zt}}{\omega_n} \cdot \frac{d}{dt} i_z = u_{dio} - u_{dc} - \frac{\pi}{6} \cdot f \cdot x_i \cdot i_z \tag{4.75}$$

Where the reactance x_{zt} is defined as following:

$$x_{zt} = \frac{\pi^2}{18} \cdot x_z \tag{4.76}$$

The block diagram for the intermediate circuit, presented in figure 4.10, are draw based on equation 4.75. The frequency of the system is equal to the speed of the generator in per unit and therefore $f = n$ is introduced to the model.

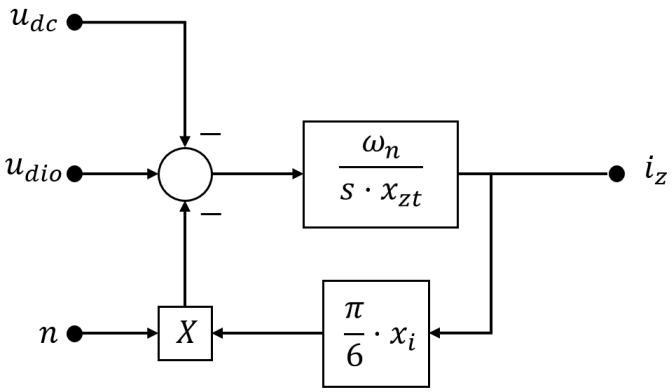

Figure 4.10: Block diagram for the intermediate circuit

The transfer function for intermediate circuit are calculated based on equation 4.70 in equation 4.77.

$$\begin{aligned} r_z \cdot T_z \cdot s \cdot i_z &= u_{dio} - u_{dc} - r_z \cdot i_z \\ i_z \cdot r_z \left(1 + T_z \cdot s\right) &= u_{\mathrm{dio}} - u_{dc} \\ \frac{i_z}{u_{dio} - u_{dc}} &= \frac{1}{(1 + T_z \cdot s)} \end{aligned} \tag{4.77}$$

DC-link capacitor

The same procedure is repeated for the DC-link capacitor. The capacitor equation 4.78 can be deduced based on figure 4.9. The per unit voltage and current are introduced:

$$(I_z - I_{dc}) = C \cdot \frac{d}{dt} U_{dc} \tag{4.78}$$

$$(i_z - i_{dc}) \cdot I_{br} = C \cdot \frac{d}{dt} \cdot u_{dc} \cdot U_{br} \tag{4.79}$$

Equation 4.79 is solved with regards to the derivative of the DC-link voltage. The term ω_n/ω_n is introduced in in order to include the capacitor reactance, which is defined in equation 4.81.

$$\begin{aligned} \frac{d}{dt} \cdot u_{dc} &= (i_z - i_{dc}) \cdot \frac{1}{C} \cdot \frac{\omega_n}{\omega_n} \cdot \frac{I_{br}}{U_{br}} \\ &= \omega_n \cdot x_c \cdot (i_z - i_{dc}) \end{aligned} \tag{4.80}$$

Where the capacitor reactance in per unit is given by:

$$x_c = \frac{1}{C \cdot \omega} \cdot \frac{I_{br}}{U_{br}} \tag{4.81}$$

$$= x_c = \frac{\pi^2}{18} \cdot \frac{1}{C\omega} \cdot \frac{\hat{I}_n}{\hat{U}_n} \tag{4.82}$$

$$\tag{4.83}$$

The block diagram, based on equation 4.80, can then be drawn as in figure 4.11.

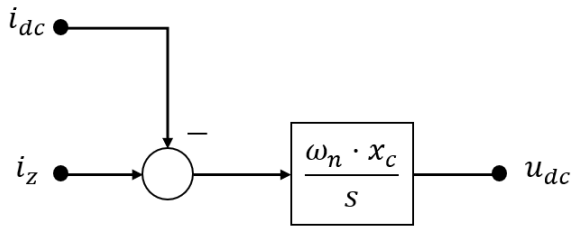

Figure 4.11: Block diagram for the DC-link capacitor

4.2.4 Phasor diagram

A phasor diagram for the diode rectifier with generator reference at an arbitrary operation point is presented in figure 4.12. The stator current is observed to be negative since the machine is operated as a generator. The angle between the current i_g and the stator voltage is denoted as φ_{g_1}. This angle is positive in capacitive generator operation, due to vector definitions.

The base values for the rectifier was chosen such that the voltage and the current would be equal generator stator voltage and current in per unit. Based on this the equalities in equation array 4.84 applies.

$$u_s = u_{dio} \qquad i_s = i_g = i_z \tag{4.84}$$

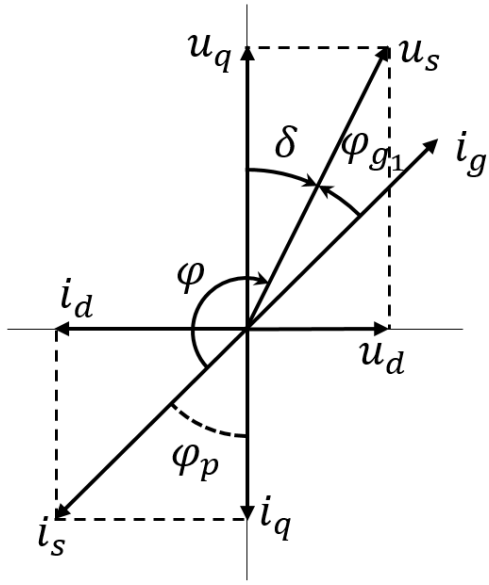

Figure 4.12: Phasor diagram for the rectifier circuit

The generator power angle δ is negative while the machine is operated as a generator. The d- and q-axis components of the stator voltage can therefore be written as:

$$u_d = u_s \cdot \sin(-\delta) = -u_s \sin(\delta) \qquad u_q = u_s \cdot \cos(-\delta) = u_s \cdot \cos(\delta) \tag{4.85}$$

The angle between u_q and i_g are, applying the rules of vertical angles, equal to the angle φ_p:

$$\varphi_p = \varphi_{g_1} - \delta \tag{4.86}$$

The d- and q-axis currents can be calculated as follows:

$$i_d = -\, i_z \cdot \sin(\varphi_p) \qquad\qquad i_q = -\, i_z \cdot \cos(\varphi_p) \tag{4.87}$$

The stator voltage is to be calculated as a function of the d- and q-axis voltages. An altitude is draw from the right angle to the hypotenuse, splitting it in two, and creating two similar triangles. The angle δ can be found in the second triangle as shown i figure 4.13.

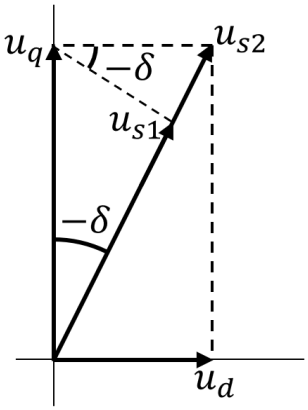

Figure 4.13: Segmenting the hypotenuse

The total length of the stator voltage phasor can then be calculated from equation 4.88. The two segments of the phasor are calculated using trigonometric function, as shown in expression array 4.89.

$$u_s = u_{s1} + u_{s2} \tag{4.88}$$

$$u_{s1} = u_q \cdot \cos(-\delta) = u_q \cdot \cos(\delta) \qquad u_{s2} = u_d \cdot \sin(-\delta) = -u_d \cdot \sin(\delta) \tag{4.89}$$

Combining equations 4.88 and 4.89 yields the following expression for the stator and rectifier voltage:

$$u_{dio} = u_s = u_q \cdot \cos(\delta) - u_d \cdot \sin(\delta) \tag{4.90}$$

4.3 The combined model

It is beneficial to consider the synchronous machine, the intermediate circuit and the DC-link capacitor as one controlled system, since there is a strong interdependence between them. The modeling of the combined system is based on LCI-converter model from chapter 5 in [28].

Inputs for this system are the field voltage, outputs are generator speed and field current, while DC-link current and the load torque occurs as disturbances. The combined system is illustrated in figure 4.14. The field voltage and current are utilized in the inner controller for the system.

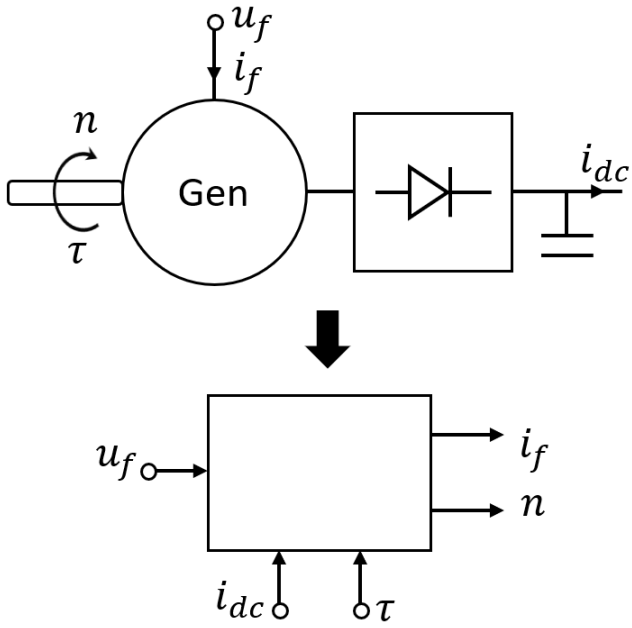

Figure 4.14: Illustration of the combined system

4.3.1 Block diagram of the combined system

The block diagram of the combined system are constructed from the synchronous machine block diagram, from figure 4.3, the intermediate circuit block diagram, from figure 4.10, and the DC-link capacitor block diagram from figure 4.11. It is necessary to inspect the transitional variables in the combined system. These are the variables connecting the generator model to the diode model. The voltage relation between the model is given by equation 4.90, while the current relations are given by equation array 4.87. The resulting block diagram for the combined system is presented in figure 4.15. The transitional variables are then observed to be the angles φ_{g_1} and δ.

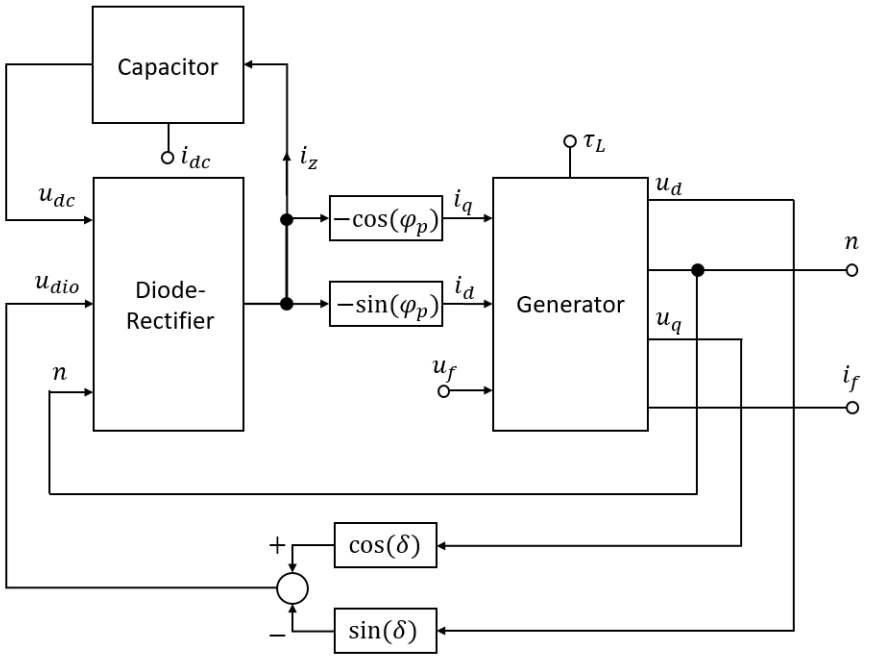

Figure 4.15: Block diagram of the combine system

4.3.2 Analyzing variables in the combined model

The transitional- and operation variables of the model are analyzed. The transitional variable are the power factor angle φ_{g_1} and the generator power angle δ. The operation variables are the field current and the torque. These variables are analyzed as a function of the intermediate current, which is determined by the loads on the DC-link.

Operation points

The relationship between the speed, flux and the stator voltage in steady state is presented in equation 4.49. If the stator resistance is assumed to be zero, the following equation occurs:

$$\underline{u}_s = j \cdot n \cdot \underline{\psi}_s \tag{4.91}$$

Where the stator flux vector consisting of the d- and q-axis flux, from equation 4.46:

$$\psi_q = x_q \cdot i_q \qquad\qquad \psi_d = x_d \cdot i_d + x_{md} \cdot i_f \tag{4.92}$$

The dependency between the different variables can be observed from equation 4.91, expression array 4.92 and figure 3.5:

The end goal for the control system is to regulate the DC-link voltage. It can be observed from expression array 4.55 that the DC-link voltage is dependent on the converter voltage U_{dio}, and the voltage-drop due to commutation. The voltage drop increases with increasing DC-link current, which means that u_s must be adjusted accordingly in order to keep constant DC-link voltage.

The stator voltage is dependent on the generator speed and the stator flux. The generator speed is controlled by an independent control system, in order to achieved optimal fuel consumption of the prime mover, according to figure 3.5. Therefore, by observing expression array 4.92, it becomes clear that the only free variable in the system is the field current. The field current, which is controlled the inner control loop, receives the reference from the outer DC-link voltage control loop. The system controllers are analyzed in detail in chapter 5.

The relation between the stator flux and the intermediate current becomes relevant when expressions for the operation variables are deduced. When evaluated, it becomes evident that the operation variables are dependent on both the intermediate current and the stator flux. It is beneficial to be able to calculate these equations based one changing variable and otherwise constant values. Since the models are based on the intermediate current, this variable is chosen. Ideally, an expression for the absolute value of the stator flux as a function of the intermediate current should be developed. However, due to time constraints, three different operation point are investigated:

- *Point one*: Operation of prime mover at $0.2pu$ which corresponds to $n = 0.58pu$.
- *Point three*: Operation of the prime mover at $1pu$. The generator is assumed to produce $0.9pu$ of active power, which determines the intermediate current.
- *Point two*: A middle speed point between the two set above. This results in $n = 0.8pu$ and $0.52pu$ loading.

The values for these operation points are presented in table 4.1. The calculations themselves are conducted in appendix B. Note that the inductance x_s is assumed zero in order to simplify the calculations.

The value of the DC-link capacitor depends on the number of inverters connected at the given operation point. It is assumed that for each MW connected through inverters an additional $10mF$ are added to the total DC-link capacitor.

Table 4.1: Generator operation points

Operation point one	Operation point two	Operation point three
$p_1 = 0.2pu$	$p_2 = 0.52pu$	$p_3 = 0.9pu$
$i_{z_1} = 0.27pu$	$i_{z_2} = 0.72pu$	$i_{z_3} = 1.23pu$
$u_{dio_1} = 0.757pu$	$u_{dio_2} = 0.78pu$	$u_{dio_3} = 0.864pu$
$n_1 = 0.58pu$	$n_2 = 0.8pu$	$n_3 = 1pu$
$\psi_1 = 1.305pu$	$\psi_2 = 1pu$	$\psi_3 = 0.864pu$
$x_c = 0.67pu$	$x_c = 0.29pu$	$x_c = 0.17pu$

When the operation variables are plotted in the following chapter, the three operation points are marked with diagonal crosses in the graphs. Additionally, a plot of the variables when the stator flux is assumed equal to $1pu$ are included. This is to determine if an assumption of constant stator flux would be applicable in further calculation.

Power factor φ_{g_1}

Equation 4.68 is inserted into equation 2.4 and the inverse trigonometric function is applied, which results in the power factor angle presented in equation 4.93. The approximated power factor angle as a function of i_z and the three operation points are plotted in figure 4.16.

$$\varphi_{g_1} = \arccos\left(1 - \frac{\pi}{6} \cdot \frac{x_i i_z}{\psi_s}\right) \tag{4.93}$$

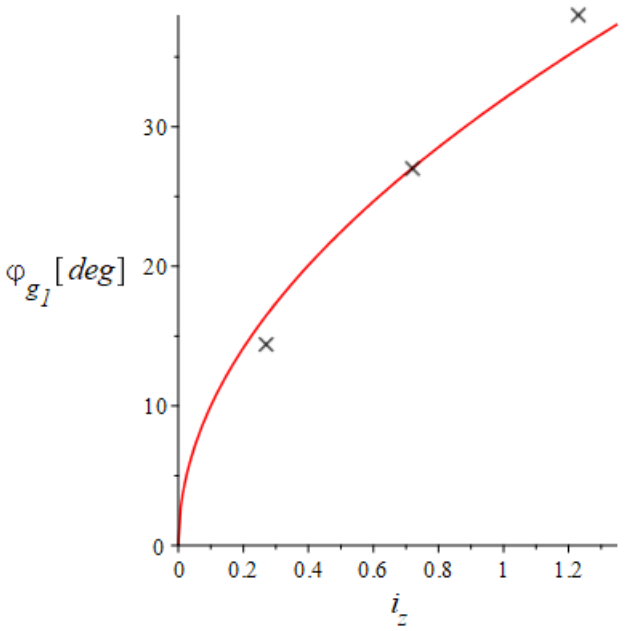

Figure 4.16: Power factor angle

Power angle δ

The expression for u_d from expression array 4.48 is solved for $tan(\delta)$:

$$\sin(\delta) = -\frac{u_d}{u_s} \tag{4.94}$$

The equation for u_d from expression array 4.47 and equation 4.49, as absolute values, are inserted into equation 4.94, which yield:

$$\sin(\delta) = -\frac{r_s \cdot i_d - \psi_q \cdot n}{r_s \cdot i_s + \psi_s \cdot n} \tag{4.95}$$

The stator resistance r_s is approximated to zero and the equation for ψ_q from expression array 4.46 is inserted in equation 4.95:

$$\sin(\delta) = \frac{x_q i_q}{\psi_s} \tag{4.96}$$

Finally, the expression for i_q from expression array 4.87 are substituted into equation 4.96. After some restructuring and utilizing the inverse trigonometric function, the following expression for the power angle occurs:

$$\delta = \arctan\left(-\frac{i_s \cdot \cos(\varphi_1)}{\frac{\psi_s}{x_q} + i_s \cdot \sin(\varphi_1)}\right) \tag{4.97}$$

The approximated power angle as a function of i_z and the three operation points are plotted in figure 4.17.

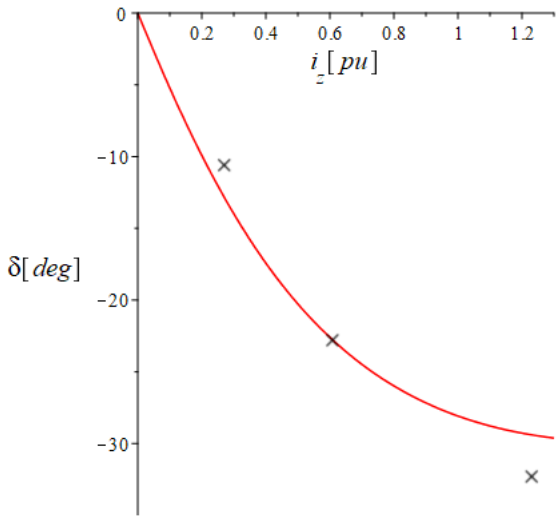

Figure 4.17: Generator power angle

Torque

The equations for u_d and u_q from expression array 4.85 and expression array 4.47, where r_s is approximated to be equal zero, can be set equal to each other as shown i expression array 4.98. When the common terms are eliminated, equations for the d- and q-axis fluxes occurs.

$$\begin{aligned} -n \cdot \psi_q &= -n \cdot \psi_s \cdot \sin(\delta) & \qquad n \cdot \psi_d &= n \cdot \psi_s \cdot \cos(\delta) \\ \psi_q &= \psi_s \cdot \sin(\delta) & \qquad \psi_d &= \psi_s \cdot \cos(\delta) \end{aligned} \tag{4.98}$$

Introducing the equations for the d- and q-fluxes from equation array 4.98 and the equations for the d- and q-currents from expression array 4.87 in equation 4.38 results in, after some calculations, the following equation for the torque:

$$m_e = -i_z \psi_s \cos\left(\varphi_{g_1}\right) \tag{4.99}$$

The approximated torque as a function of i_z and the three operation points are plotted in figure 4.18.

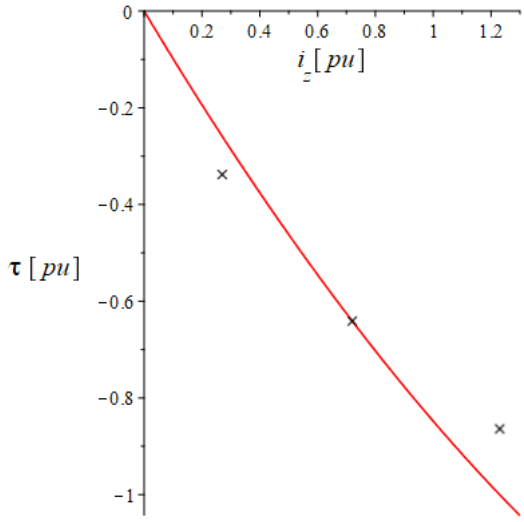

Figure 4.18: Necessary torque from prime mover

Magnetizing current

From figure 4.4 the following equality can be observed:

$$n \cdot x_{md} \cdot i_f = u_q - n \cdot i_d \cdot x_d \tag{4.100}$$

Substituting the equation for the current i_d from expression array 4.87 and for u_q from expression array 4.48, where u_s is according to 4.91 in absolute values, into equation 4.100 results in the following equation when solved for the field current:

$$i_f = \frac{\psi_s \cdot \cos(\delta) - i_s \cdot x_d \cdot \sin(\delta - \varphi_1)}{x_{md}} \tag{4.101}$$

The approximated field current as a function of i_z and the three operation points are plotted in figure 4.19.

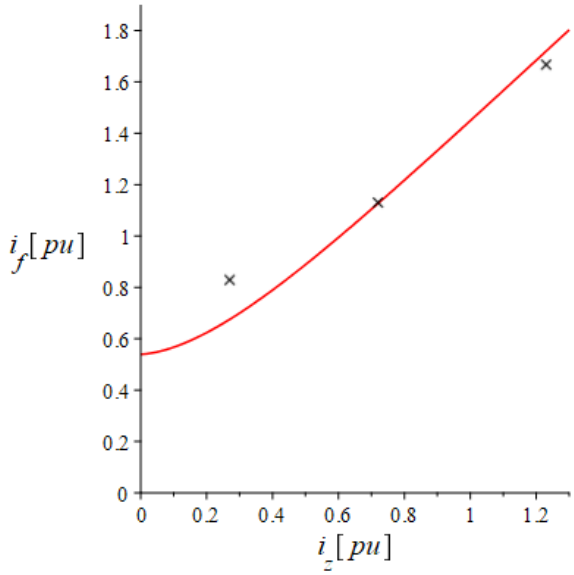

Figure 4.19: Field current as a function of intermediate current

Results from the analysis

The power angle δ, power factor angle φ_{g_1} and the transitional angle φ_p, defined in equation 4.86, are plotted for the the generators operation interval $[0.25pu < i_z < 1.25pu]$ in figure 4.20. These plots can be converted to look-up tables and utilized in the controller tuning calculations. It is then possible to utilize these variables, based on the intermediate current, without further calculations.

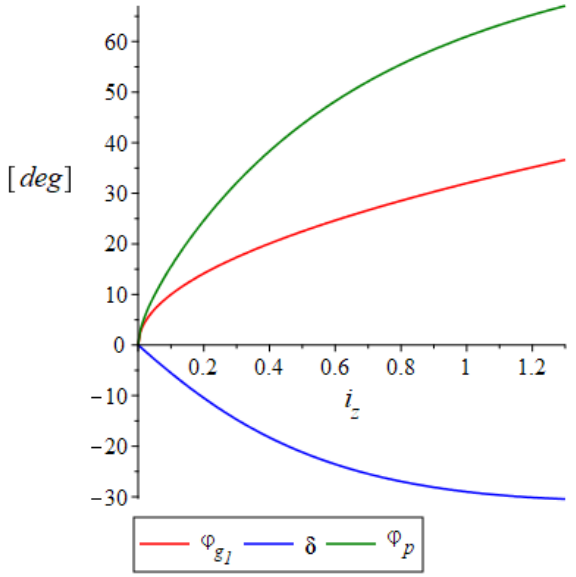

Figure 4.20: Transitional angle variables

It is evident from figure 4.17, 4.38 and 4.19 that the approximation with constant flux are rather inaccurate. The power angle and torque evaluation are accurate for low intermediate current, while the field current is accurate for high intermediate current.

4.3.3 Phasor diagram

A phasor diagram for the combined system is constructed based on the diagrams in figure 4.12 and 4.4 and presented in figure 4.21. The vector diagram are draw for operation point two from chapter 4.3.2. The calculation of vectors and angles are performed in appendix C.

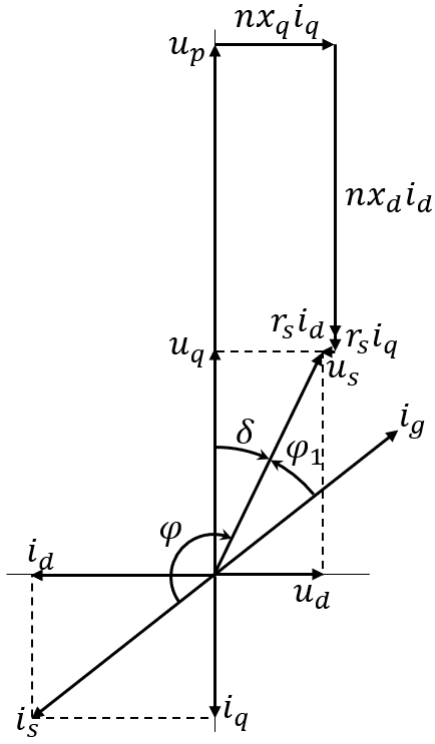

Figure 4.21: Vector diagram for the combined system

It can be observed from figure 4.21 that the actual power factor angle for the system can be calculated according to equation 4.102.

$$\varphi = -\pi + \varphi_1 \tag{4.102}$$

Chapter 5

The control system

The control structure for the regulation system is presented in figure 5.1. The control structure consists of a speed controller and a DC-link voltage controller. The speed controller regulates the speed of the prime mover to achieve optimal fuel consummation, according to chapter 3.3 and figure 3.5. The design of the speed controller is not in the scope of work for this thesis and are therefore not analyzed further.

The DC-link voltage controller consists of an inner field current controller, and an outer voltage controller. The DC-link voltage is measured, compared to a reference value and evaluated in a PI-controller. The output from the outer PI-controller acts as a reference for the field current controller. The field current is regulated by the inner PI-controller to achieve desired DC-link voltage.

The functions in this chapter are plotted for the three operation points from chapter 4.3.2. However, in order to reduce the number of changing variables, the capacitor is initially assumed to be $470mF$. The value used in the specialization project. This results in a reactance of $0.042pu$. An arbitrary value of $0.05pu$ are chosen for the inductance L_f

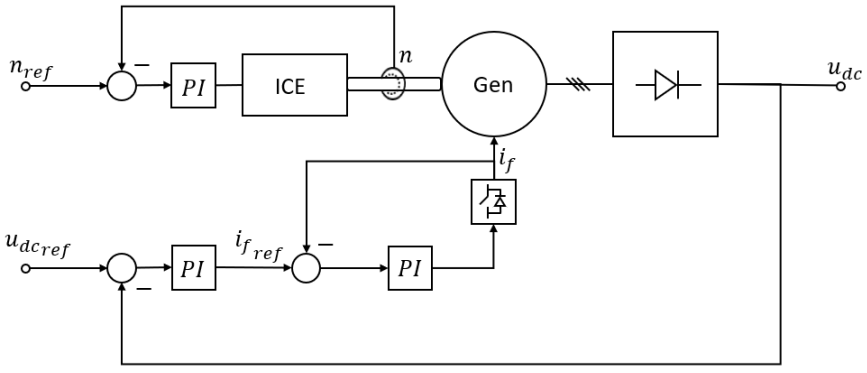

Figure 5.1: Control structure

5.1 System equations for the controlled system

A linear description of the system is essential if Laplace transformed transfer functions are to be utilized. The linearity of the system equations is therefore investigated. Non-linear system equations are linearized around an operation point.

Generator

The relevant equations for the synchronous machine were derived in chapter 4.1.5. The equations are evaluated for a given operation point. The equations for the d- and q-axis voltages from expression array 4.39 are linear if the generator speed is assumed constant. The speed is constant in steady state, and the assumption is therefore accurate. The equation for the d- and q-axis can then be written as:

$$\begin{aligned} \Delta u_d &= r_s \cdot \Delta i_d + \frac{s}{\omega_n} \cdot \Delta \psi_d - n \cdot \Delta \psi_q \\ \Delta u_q &= r_s \cdot \Delta i_q + \frac{s}{\omega_n} \cdot \Delta \psi_q - n \cdot \Delta \psi_d \end{aligned} \tag{5.1}$$

Equally, equation 4.40 and 4.41 for the mutual fluxes becomes:

$$\Delta \psi_q = x_q(s) \cdot \Delta i_q \tag{5.2}$$

$$\Delta \psi_d = x_d(s) \cdot \Delta i_d + \frac{\omega_n \cdot T_f}{1 + T_f s} \cdot \frac{x_d - x'_d}{x_{md}} \cdot \Delta u_f \tag{5.3}$$

Finally, equation 4.19 for the field current is evaluated:

$$\Delta i_f = \frac{\omega_n \cdot T'_{d0}}{1 + T'_{d0} \cdot s} \cdot \frac{x_d - x'_d}{x^2_{md}} \cdot \Delta u_f - \frac{T'_{d0} \cdot s}{1 + T'_{d0} \cdot s} \cdot \frac{x_d - x'_d}{x_{md}} \cdot \Delta i_d \tag{5.4}$$

Rectifier

The rectifier with generator reference was analyzed in chapter 4.2.2. The linearity of equation 4.77 for the intermediate current is evaluated. It is observed that the intermediate current has a linear dependency on the rectifier voltage and the DC-link voltage, and can therefore be written as:

$$\Delta i_z = \frac{\Delta u_{dio} - \Delta u_{dc}}{r_z \left(1 + s T_z\right)} \tag{5.5}$$

Combined system

The voltage relation in the combined model is given by equation 4.90, while the current relations are given by equation array 4.87. The trigonometric function involving the transitional variables, plotted in figure 4.20, causes these equations to be non-linear. They are therefore linearized in appendix D. The result of the linearization and associated considerations are presented in this chapter.

The relations between the linearization d- / q-axis currents and the intermediate current are shown in equation 5.6. The variables K_{dz} and K_{qz}, called the linearization variables, are presented in equation 5.7. These are plotted as a function of the intermediate current in figure 5.2. The expression involved in these plot calculations is rather extensive and are not included.

$$\Delta i_d = -K_{dz}\Delta i_z \qquad \Delta i_q = K_{qz}\Delta i_z \tag{5.6}$$

$$\begin{aligned} K_{dz} &= \sin(\varphi_\delta) + i_s \cdot \cos(\varphi_\delta) \cdot \frac{d(\varphi_\delta)}{di_z} \\ K_{qz} &= -\cos(\varphi_\delta) + i_s \cdot \sin(\varphi_\delta) \cdot \frac{d(\varphi_\delta)}{di_z} \end{aligned} \tag{5.7}$$

The voltage relation between the rectifier model and the generator model is observed to be non-linear, due to the involvement of power angle δ. The calculations of the linearization variable for the voltage equation was initiated in appendix D, but not concluded due to time constrains. The voltage relation is therefore assumed to be linear in further calculations, which results in the following equation:

$$\Delta u_{dio} = \Delta u_q \cdot \cos(\delta) - \Delta u_d \cdot \sin(\delta) \tag{5.8}$$

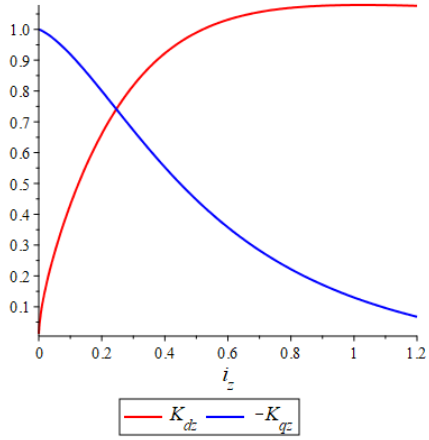

Figure 5.2: Linearization variables

5.2 Signal flow diagram of the system

The system equations from chapter 5.1 is drawn in a signal flow diagram in figure 5.3. A signal flow diagram is a set of nodes which are connected by direct branches. A branch denoted G_{ab} originates in node a and terminates in node b, where the direction is indicated by an arrowhead [29]. A signal passing through any branch is multiplied by the transfer function or variable for that branch. Each node adds up the incoming signals algebraically and delivers the resulting signal on the output. The sign of each branch is defined by the transfer function.

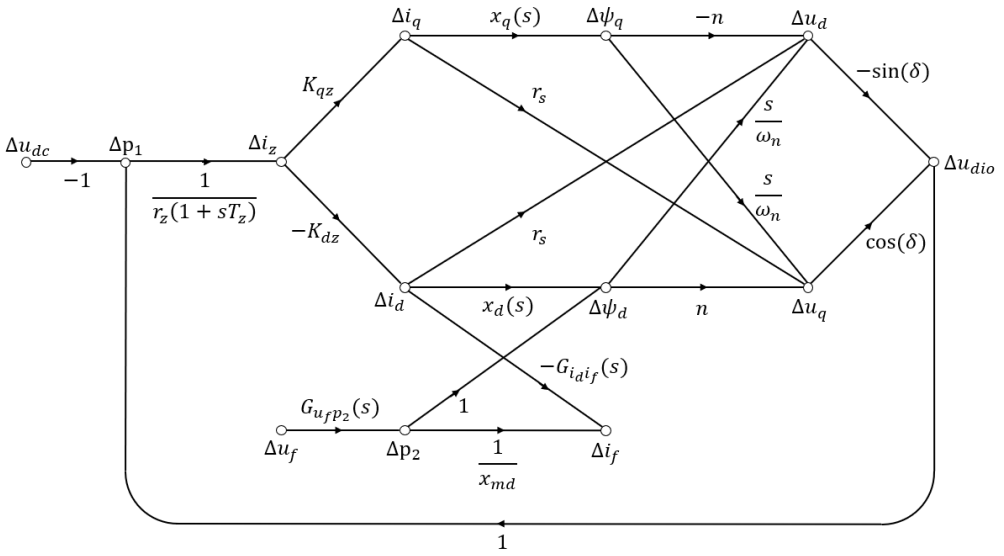

Figure 5.3: Signal flow diagram for the systems

The unnamed nodes in the generator model are given the name Δp_1 and Δp_2. Equation 5.4 for the field current is restructured into equation 5.9 for convenience. The transfer functions introduced in equation 5.9 are defined in expression array 5.10.

$$\Delta i_f = G_{u_f p_2}(s) \cdot \frac{1}{x_{md}} \cdot \Delta u_f - G_{i_d i_f}(s) \cdot \Delta i_d \tag{5.9}$$

$$\begin{aligned} G_{u_f p_2}(s) &= \frac{\omega_n \cdot T'_{d0}}{1 + T'_{d0} \cdot s} \cdot \frac{x_d - x'_d}{x_{md}} \\ G_{i_d i_f}(s) &= \frac{T'_{d0} \cdot s}{1 + T'_{d0} \cdot s} \cdot \frac{x_d - x'_d}{x_{md}} \end{aligned} \tag{5.10}$$

5.3 Node reduction

The nodes which are of no further interest are eliminated from the flow diagram. Firstly, the branches between the nodes Δi_z, Δu_{dio} Δu_f and Δi_f are evaluated, as displayed in figure 5.4. It can be observed from the figure that this section only contains cascade branches which means no feedback loops. It is then possible to reduce the number of nodes in a chosen sequence, called the order of flow, such that no feed-back occurs [29]. The removal of the nodes creates a new cascade graph with the transformed branch transfer functions.

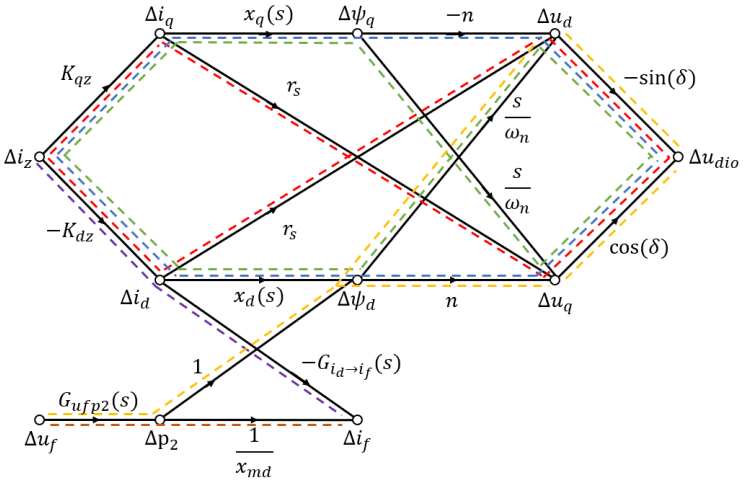

Figure 5.4: Node reduction between Δi_z and Δu_{dio}

The objective of the first transformation is to eliminated all the nodes except the periphery nodes Δi_z, Δu_{dio} Δu_f and Δi_f. According to rule one in figure 5.5, the center nodes can be eliminated as long as there are no cross connected branches. The branches in figure 5.4 are restructured according to the colored dotted lines to get rid of the cross connections. The transformation rules involved in the restructure and subsequent node reduction are presented in figure 5.5. The new breaches are calculated in equation 5.11-5.16.

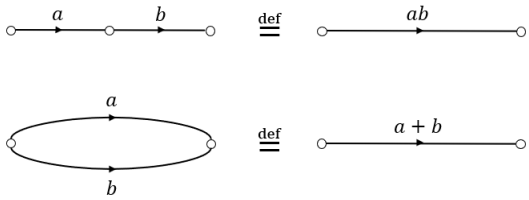

Figure 5.5: Node reduction rules

Parallel branch one: Red

$$\begin{aligned} G_{i_z u_{dio}(1)} &= K_{qz} \cdot r_s \cdot \cos(\delta) - K_{dz} \cdot r_s \cdot (-\sin(\delta)) \\ &= -r_s \left(-K_{qz} \cdot \cos(\delta) - K_{dz} \cdot \sin(\delta)\right) \end{aligned} \tag{5.11}$$

Parallel branch two: Blue

$$\begin{aligned} G_{i_z u_{dio}(2)}(s) &= K_{qz} \cdot x_q(s) \cdot (-n) \cdot (-\sin(\delta)) - K_{dz} \cdot x_d(s) \cdot n \cdot \cos(\delta) \\ &= -n \left(K_{dz} \cdot x_d(s) \cdot \cos(\delta) - K_{qz} \cdot x_q(s) \cdot \sin(\delta)\right) \end{aligned} \tag{5.12}$$

Parallel branch three: Green

$$\begin{aligned} G_{i_z u_{dio}(3)}(s) &= K_{qz} \cdot x_q(s) \cdot \frac{s}{\omega_n} \cdot \cos(\delta) - K_{dz} \cdot x_d(s) \cdot \frac{s}{\omega_n} \cdot (-\sin(\delta)) \\ &= -\frac{s}{\omega_n} \left(-K_{dz} \cdot x_d(s) \cdot \sin(\delta) - K_{qz} \cdot x_q(s) \cdot \cos(\delta)\right) \end{aligned} \tag{5.13}$$

Yellow branch: Between the nodes Δu_f and Δu_{dio}:

$$\begin{aligned} G_{u_f u_{dio}}(s) &= G_{u_f p_2}(s) \cdot n \cdot \cos(\delta) + G_{u_f p_2}(s) \cdot \frac{s}{\omega_n} \cdot (-\sin(\delta)) \\ &= G_{u_f p_2}(s) \cdot \left(n \cdot \cos(\delta) - \frac{s}{\omega_n} \cdot \sin(\delta)\right) \\ &= \frac{\omega_n \cdot T'_{d0}}{1 + T'_{d0} \cdot s} \cdot \frac{x_d - x'_d}{x_{md}} \cdot \left(n \cdot \cos(\delta) - \frac{s}{\omega_n} \cdot \sin(\delta)\right) \end{aligned} \tag{5.14}$$

Purple branch: Between the nodes Δi_z and Δi_f:

$$\begin{aligned} G_{i_z i_f}(s) &= -K_{dz} \cdot -G_{i_d i_f}(s) \\ &= K_{dz} \cdot \frac{T'_{d0} \cdot s}{1 + T'_{d0} \cdot s} \cdot \frac{x_d - x'_d}{x_{md}} \end{aligned} \tag{5.15}$$

Brown branch: Between the nodes Δu_f and Δi_f:

$$G_f(s) = \frac{\omega_n \cdot T'_{d0}}{1 + T'_{d0} \cdot s} \cdot \frac{x_d - x'_d}{x_{md}^2} \tag{5.16}$$

The result are three parallel branches between Δi_z and Δu_{dio} which are presented in 5.11-5.13. The other connected nodes are reduced to single connected branches according to equation 5.14-5.16. Additionally, the branch between Δp_1 and Δi_z is defined as:

$$G_{p_1 i_z}(s) = \frac{1}{r_z\,(1 + sT_z)} \tag{5.17}$$

It is then possible to remove every node inside these branches. The resulting flow diagram is displayed in figure 5.6.

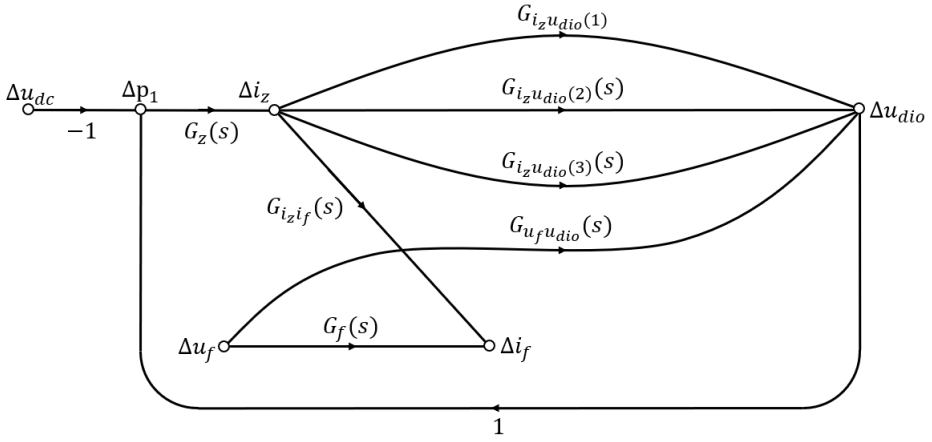

Figure 5.6: Node reduces flow diagram

In the second transformation the flow diagram is reduced to the nodes Δu_{dc}, Δi_z Δu_f and Δi_f, with individual branch connections. To begin with, the transfer function between Δp_1 and Δi_z is investigated. The relation is given by the transfer function $G_z(s)$ divided by a positive feedback of the open loop transfer function. Note that the influence by Δu_f is not considered in these calculations, since influence of Δp_1 on Δi_z is investigated. The transfer function is calculated below:

$$\begin{aligned} G_{p_1 i_z}(s) &= \frac{G_z(s)}{1 - G_z \cdot \left(G_{i_z u_{dio}(1)} + G_{i_z u_{dio}(2)}(s) + G_{i_z u_{dio}(3)}(s)\right)} \\ &= \frac{1}{\frac{1}{G_z} - \left(G_{i_z u_{dio}(1)} + G_{i_z u_{dio}(2)}(s) + G_{i_z u_{dio}(3)}(s)\right)} \end{aligned} \tag{5.18}$$

A new transfer function denoted $N(s)$ is defined in equation 5.19. This is done for convenience when presenting the transfer function, evident in equation 5.20.

$$N(s) = \frac{1}{G_{p_1 i_z}} \tag{5.19}$$

$$\begin{aligned} N(s) = r_z \left(1 + T_z \cdot s\right) + r_s \cdot \left(-K_{qz} \cdot \cos(\delta) - K_{dz} \cdot \sin(\delta)\right) \\ + n \left(K_{dz} \cdot x_d(s) \cdot \cos(\delta) - K_{qz} \cdot x_q(s) \cdot \sin(\delta)\right) \\ + \frac{s}{\omega_n} \left(-K_{dz} \cdot x_d(s) \cdot \sin(\delta) - K_{qz} \cdot x_q(s) \cdot \cos(\delta)\right) \end{aligned} \tag{5.20}$$

The definitions of r_z from equation 4.71 and T_z from equation 4.72 is introduced into equation 5.20. Some restructuring yields the following result:

$$\begin{aligned} N(s) =& r_s \left(-K_{qz} \cdot \cos(\delta) - K_{dz} \cdot \sin(\delta)\right) \\ &+ n \left(\frac{\pi x_\sigma}{6} + K_{dz} \cdot x_d(s) \cdot \cos(\delta) - K_{qz} \cdot x_q(s) \cdot \sin(\delta)\right) \\ &+ \frac{s}{\omega_n} \left(x_{zt} - K_{dz} \cdot x_d(s) \cdot \sin(\delta) - K_{qz} \cdot x_q(s) \cdot \cos(\delta)\right) \end{aligned} \tag{5.21}$$

The transfer function between Δu_{dc} and Δi_z is then:

$$G_{u_{dc} i_z}(s) = -1 \cdot G_{p_1 i_z} \tag{5.22}$$

Which can be written as:

$$-G_{u_{dc} i_z}(s) = \frac{1}{N(s)} \tag{5.23}$$

The bode plot of the transfer function $G_{u_{dc} i_z}(s)$ is displayed in figure 5.7. The steady state and transient gain are analyzed for the function.

Firstly, the inductance transfer functions are investigated. When $s \to \infty$ the reactances transfer functions in equation 5.21 is equal their sub-transient states:

$$x_d(\infty) = x_d^{''} \qquad x_q(\infty) = x_q^{''} \tag{5.24}$$

On the other hand, when $s \to 0$, the reactance functions is equal their steady-steady state values:

$$x_d(0) = x_d \qquad x_q(0) = x_q \tag{5.25}$$

It is observed that the steady state gain at $G_{u_{dc}i_z}(0)$ is equal to the inverse of the two first terms in 5.21 inserted the equation in expression array 5.24.

The transfer functions $G_{u_{dc}i_z}(\infty)$ is dominated by the integrator in the third term in 5.21. This results is a $-90°$ and a magnitude that approaches $-\infty$. In other word, the transient gain approaches zero.

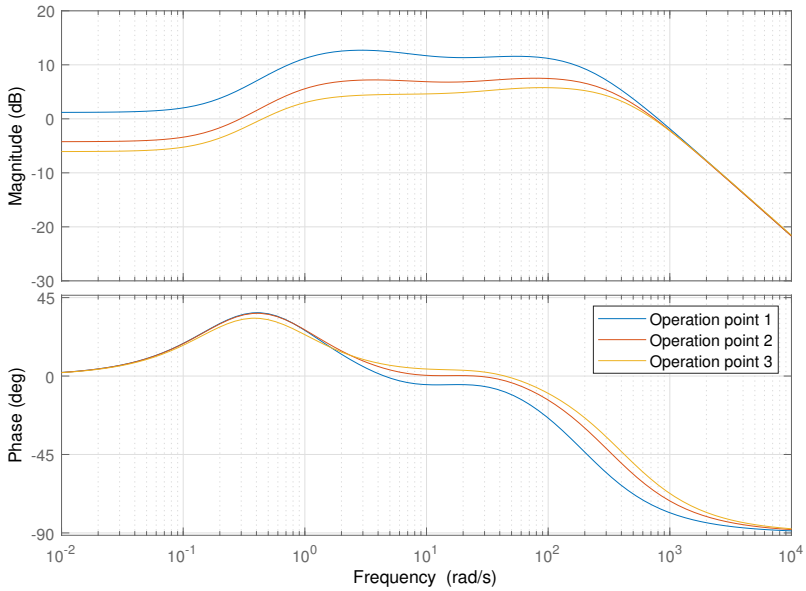

Figure 5.7: Bode plot of $G_{u_{dc}i_z}(s)$

The next transfer function investigated is between Δu_f and Δi_z. This transfer function can be observed from figure 5.6 to be equal the branch between Δu_f and Δu_{dio} times the feedback branch, which equals one, time the function $G_{p_1 i_z}(s)$ defined in equation 5.19. Note that the contribution from Δu_{dc} is not considered in this relation.

$$\begin{aligned} G_{u_f i_z}(s) &= G_{u_f u_{dio}}(s) \cdot 1 \cdot G_{p_1 i_z}(s) \\ &= \frac{\omega_n \cdot T'_{d0}}{1 + T'_{d0} \cdot s} \cdot \frac{x_d - x'_d}{x_{md}} \cdot \left(n \cdot \cos(\delta) - \frac{s}{\omega_n} \cdot \sin(\delta) \right) \cdot G_{p_1 i_z}(s) \end{aligned} \tag{5.26}$$

The transfer function $G_{u_f i_z}(s)$ is plotted in figure 5.8. The steady state gain is, equivalent to the above case, equal to the constant terms. The transfer function saw the introduction of a 1st order system and a differentiator into the transfer function $G_{p_1 i_z}(s)$. This means that the order of s is increased by one in both the nominator and the denominator. The transfer function $G_{u_f i_z}(s)$ therefor has the same phase of $-90°$ and the same transient gain approaching zero as $G_{p_1 i_z}(s)$.

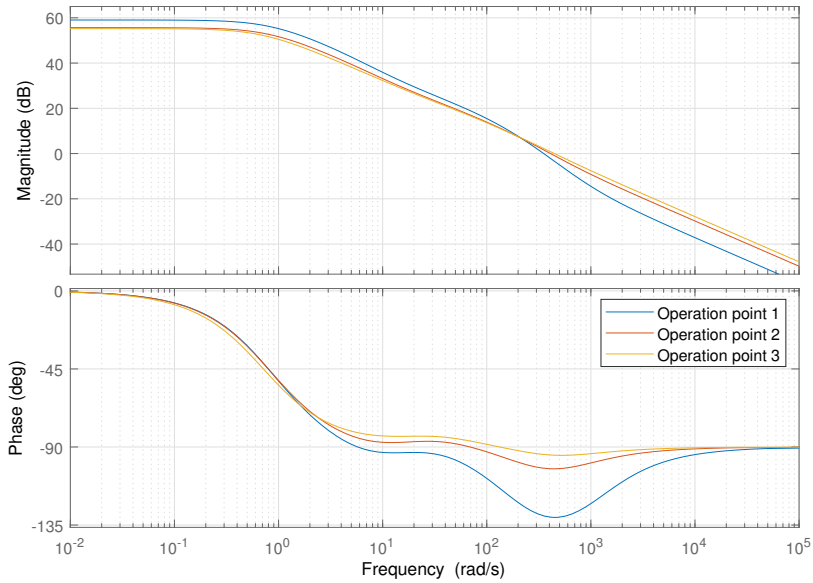

Figure 5.8: Bode plot of $G_{u_f i_z}(s)$

The third transfer function analyzed is between Δu_{dc} and Δi_f. By inspecting figure 5.6 the transfer function is found to be equal $-G_{u_{dc}i_z}(s)$ times $G_{i_z i_f}$, which can be written as:

$$\begin{aligned} G_{u_{dc}i_f}(s) &= G_{i_z i_f}(s) \cdot (-G_{u_{dc}i_z}(s)) \\ -G_{u_{dc}i_f}(s) &= K_{dz} \cdot \frac{T'_{d0} \cdot s}{1 + T'_{d0} \cdot s} \cdot \frac{x_d - x'_d}{x_{md}} \cdot G_{p_1 i_z}(s) \end{aligned} \tag{5.27}$$

The transfer function $G_{u_{dc}i_f}(s)$ is plotted in figure 5.9. A differentiator is introduced to the constant therm from the transfer function $G_{p_1 i_z}(s)$. The nominator of $G_{u_{dc}i_f}(s)$ therefore approaches zero when $s \to 0$, while a constant term is present in the denominator. The result is a steady state gain which approaches zero. The introduction of a 1st order system and a differentiator to the transfer function results in a transient gain of zero.

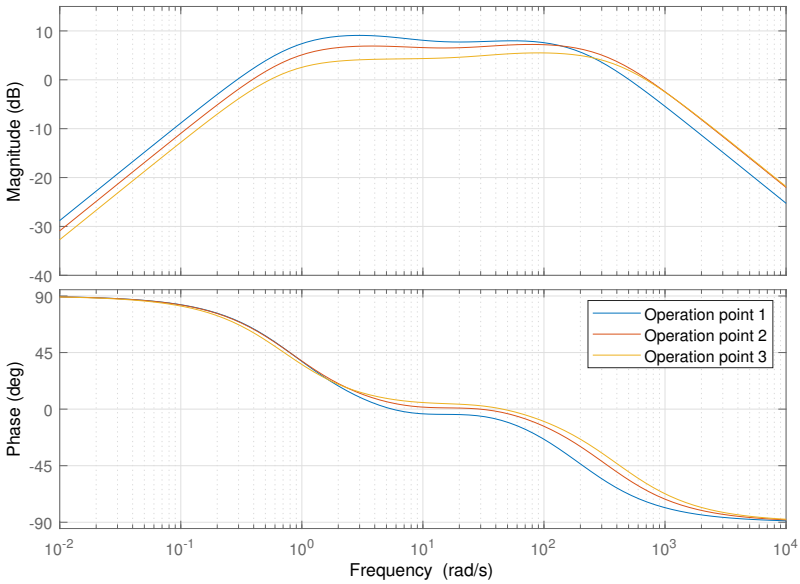

Figure 5.9: Bode plot of $G_{u_{dc}i_f}(s)$

The last transfer function analyzed from figure 5.6 is between Δu_f and Δi_f. The transfer function is obtained with super position by considering the two branches connections Δu_f and Δi_f independently. The first contribution is simply the function G_f defined in equation 5.16. This is the transfer function for the generators field current. This function is known to be a first order system with a break point in field current time constant $T_{d0}^{'}$ and a steady state gain equal r_f^{-1}.

The second contribution is from the branches $G_{u_f i_f}$ defined in equation 5.28.

$$\begin{aligned} G_{u_f i_f}(s) &= G_f(s) + G_{u_f u_{dio}}(s) \cdot G_{p_1 i_z}(s) \cdot G_{i_z i_f}(s) \\ &= G_f(s) + G_{u_f u_{dio}}(s) \cdot G_{p_1 i_f}(s) \end{aligned} \tag{5.28}$$

$$\begin{aligned} =& \frac{\omega_n \cdot T'_{d0}}{1 + T'_{d0} \cdot s} \cdot \frac{x_d - x'_d}{x_{md}^2} \\ &+ \frac{\omega_n \cdot T'_{d0}}{1 + T'_{d0} \cdot s} \cdot \frac{x_d - x'_d}{x_{md}} \cdot \left(n \cdot \cos(\delta) - \frac{s}{\omega_n} \cdot \sin(\delta) \right) \cdot G_{p_1 i_f}(s) \end{aligned} \tag{5.29}$$

$$= \frac{\omega_n \cdot T'_{d0}}{1 + T'_{d0} \cdot s} \cdot \frac{x_d - x'_d}{x_{md}} \left(\left(n \cdot \cos(\delta) - \frac{s}{\omega_n} \cdot \sin(\delta) \right) \cdot G_{p_1 i_f}(s) + \frac{1}{x_{md}} \right)$$

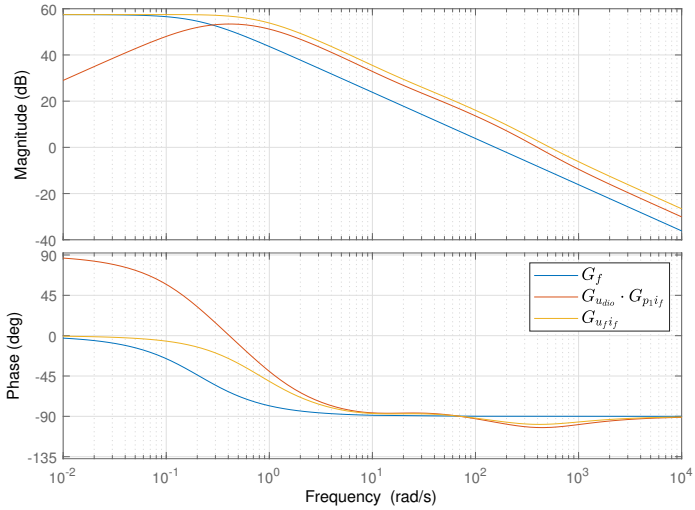

Figure 5.10: Bode plot of $G_{u_f i_f}(s)$

The two terms and the resulting transfer function $G_{u_f i_f}$ is plotted in figure 5.10. The resulting function is, as expected, to be a function of the two terms. When $s \to 0$ the function $G_{u_f i_f}(s)$ is equal $G_f(s)$, since $G_{u_f u_{dio}}(s) \cdot G_{p_1 i_f}(s)$ approaches zero gain. The transfer function $G_{u_f i_f}$ is then plotted for the three operation point in figure 5.11.

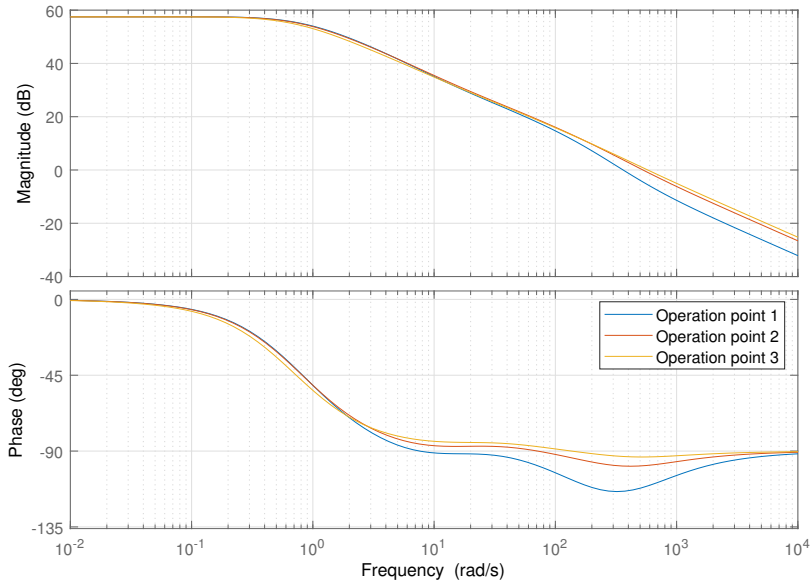

Figure 5.11: Bode plot of $G_{u_f i_f}(s)$

The last transfer function necessary to draw the new signal flow diagram is the capacitor transfer function. The function was calculated in equation 4.80, and presented below:

$$G_c(s) = \frac{\omega_n \cdot x_c}{s} \tag{5.30}$$

The node and branch reduced signal flow diagram is presented in figure 5.12.

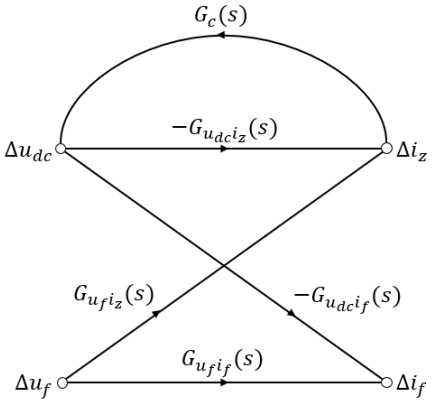

Figure 5.12: Node and branch reduced flow diagram

The regulator, exciter and filter are added to the signal flow diagram. The regulator is a PI-controller denoted G_{Rf}, the exciter a thyristor rectifier denoted G_{ef} and the filter in the feedback loop denoted G_{ffi}. The resulting flow diagram is presented in figure 5.13.

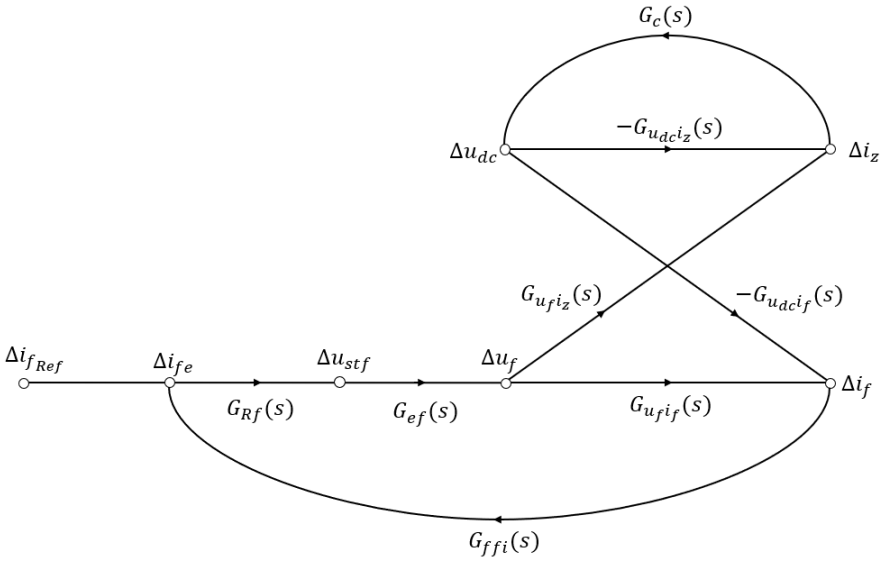

Figure 5.13: Flow diagram included regulator, exciter and filter

The final node reduction consists of transforming the branches connecting Δu_f and Δi_f into one branch. The super position principle is again utilized, and the two different relations analyzed independently. The first part is simply the transfer function $G_{u_f i_f}(s)$. The second part is a series connection between $G_{u_f i_z}(s)$, $-G_{u_{dc} i_f}(s)$ and the feedback circuit. The new transfer function, denoted $G^*_{u_f i_f}(s)$ can then be calculated:

$$\begin{aligned} G^*_{u_f i_f}(s) &= G_{u_f i_f}(s) + G_{u_f i_z}(s) \cdot \frac{G_c(s)}{1 + G_c(s) \cdot G_{u_{dc} \cdot i_z}(s)} \cdot \left(-G_{u_{dc} i_f}(s)\right) \\ &= G_{u_f i_f}(s) - \frac{G_{u_f i_z}(s) \cdot G_c(s) \cdot G_{u_{dc}}(s) i_f(s)}{1 + G_c(s) \cdot G_{u_{dc} i_z}(s)} \end{aligned} \tag{5.31}$$

The transfer function $G_{u_f i_f}$ is plotted in figure 5.14. The function observed to have the same steady state gain of r_f^{-1} as the field circuit. Additional, the first pole occurs at approximately $2 \cdot 10^{-1} rad/s$, which corresponds to the field circuit time circuit constant T'_{d0}.

It can be observed that if the poles and zeros between $2 \cdot 10^0 rad/s$ and $1 \cdot 10^3 rad/s$ are ignored, the system can be considered a first order system. This is utilized in the tuning of the controller.

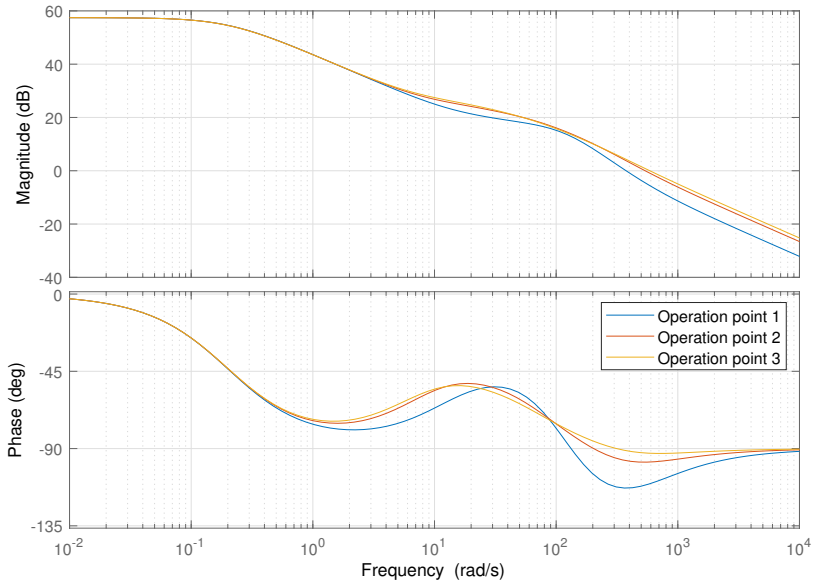

Figure 5.14: Bode plot of $G^*_{u_f i_f}(s)$

The signal flow diagram from figure 5.13 is transformed into a block diagram where the transfer function $G^*_{u_f i_f}$ from equation 5.14 is introduced:

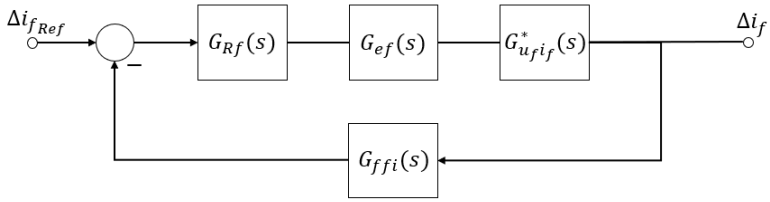

Figure 5.15: Block diagram of regulation circuit

Where the transfer functions for the filter and PI-controller are defined as following:

$$G_{rf} = k_p \cdot \frac{1 + T_i s}{T_i \cdot s} \qquad G_{ffi} = \frac{1}{1 + T_{ffi} \cdot s} \tag{5.32}$$

Initially, the exciter circuit is realized with a thyristor rectifier. The time delay for the converter is model an exponential term in control theory. However, it can be simplified by being assumed equal to a first order system [25]. The converter model is then written as:

$$u_{d\alpha f} = u_{diof} \cdot e^{-s \cdot T_{fe}} \cdot u_{control} \approx \frac{u_{dio}}{1 + s \cdot T_{ef} \cdot s} \cdot u_{control} \tag{5.33}$$

The transfer function for the exciter circuit is then given by:

$$G_{ef}(s) = \frac{u_{dio}}{1 + s \cdot T_{ef}} \tag{5.34}$$

5.4 Tuning the field regulator

The tuning of the controller is done according to the tuning principle *modulus optimum*. Theory on modulus optimum, analog filter dimensioning and calculation are conducted in appendix E. The exciter time constant and filter time constant was calculated to be equal to:

$$T_{ef} \approx 1.4\text{ms} \qquad T_{ffi} = 0.6ms \tag{5.35}$$

Firstly, the open loop transfer function for the system without the regulator is considered. The transfer function for this system is presented in equation 5.36. The gain K_{cs} and time constant T_{cs} represents the combined system. The transfer function presented in equation 5.36 is plotted in figure 5.16. It is evident from the plot that the field time constant is considerable large then the filter and exciter time constant. This is a prerequisite for merging the smaller time constant during calculations of controller parameters, which is utilized in appendix E.

$$h_{0_{ureg}} = \frac{u_{dio}}{1 + T_{ef} \cdot s} \cdot \frac{1}{1 + T_{ffi} \cdot s} \cdot \frac{K_{cs}}{1 + T_{cs} \cdot s} \tag{5.36}$$

$$K_{cs} = \frac{1}{r_f} \qquad T_{cs} = T_{d0}^{'} \tag{5.37}$$

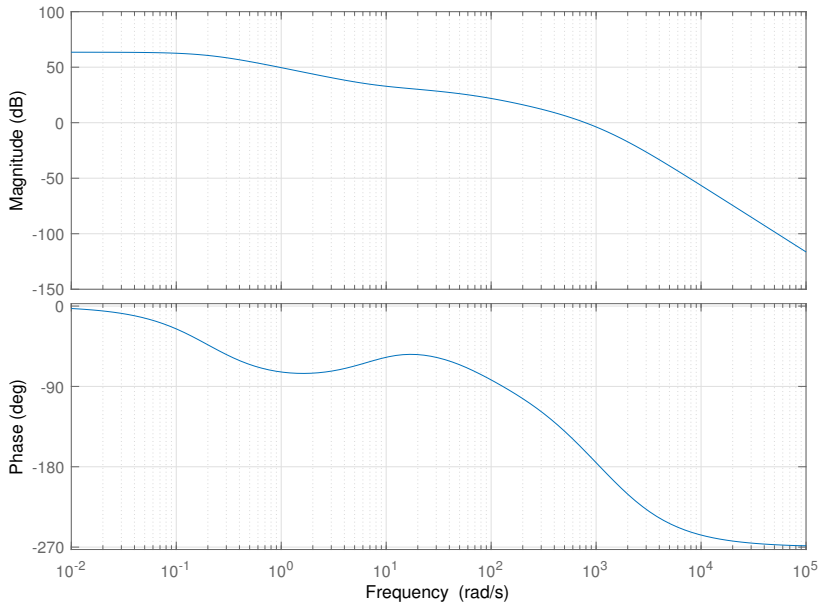

Figure 5.16: Bode plot of the open loop transfer function without regulator

The following parameters for the PI-controller was calculated in appendix chapter E.3:

$$T_i = 4.8 \qquad K_p = 0.803 \tag{5.38}$$

The open loop transfer function for the entire system including the regulator are presented in equation 5.39. This transfer function is plotted together with open loop transfer function without the PI-controller in figure 5.17. The effect of the PI-controller can then be observed in the plot. The larges time constant is eliminated, and the gain is lifted slightly compared to the system without the regulator. Additionally, the effect poles and zeros in the range between $2 \cdot 10^0 rad/s$ and $\cdot 10^3 rad/s$ are evident. An actual first order system would stay at $-90°$ until the rectifier pole at $7 \cdot 10^2$. The dislocation of the phase, and resulting magnitude, affects the gain and phase margins for the control system.

$$h_0(s) = G_{r_f}(s) \cdot G_{ef}(s) \cdot G_{ffi}(s) \cdot G^*_{ufif}(s) \tag{5.39}$$

$$= k_p \cdot \frac{1 + T_i \cdot s}{T_i \cdot s} \cdot \frac{u_{dio}}{1 + T_{fe} \cdot s} \cdot \frac{1}{1 + T_{ffi} \cdot s} \cdot \frac{K_{cs}}{1 + T_{cs} \cdot s} \tag{5.40}$$

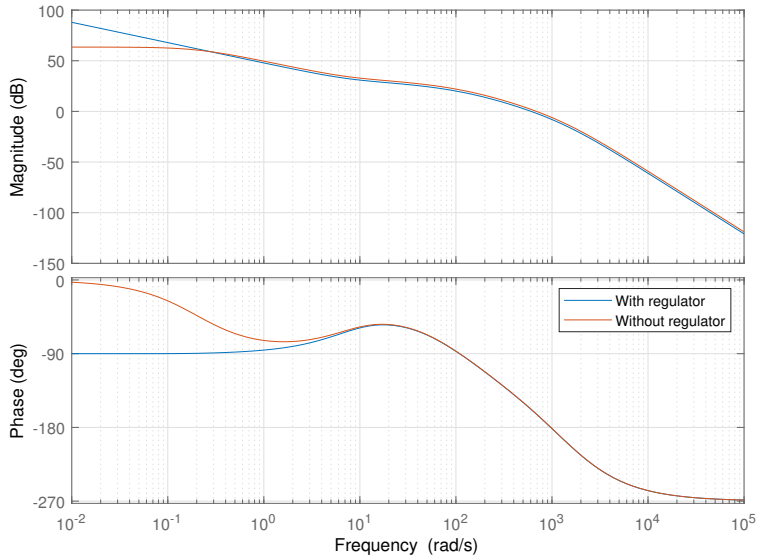

Figure 5.17: Bode plot of the open loop transfer function with and without regulator

The open loop transfer functions including the regulator are presented in figure 5.18. The phase margin and the gain margin for operation point one are investigated. Operation point one has the lowest phase margin, while the gain margin is almost equal for all three cases. A gain margin and phase margin of only $-5.3db$ and $14°$ respectively are observed. The recommended phase and gain margin for minimum oscillation in the step response is $-12db$ and $45°$ respectively.

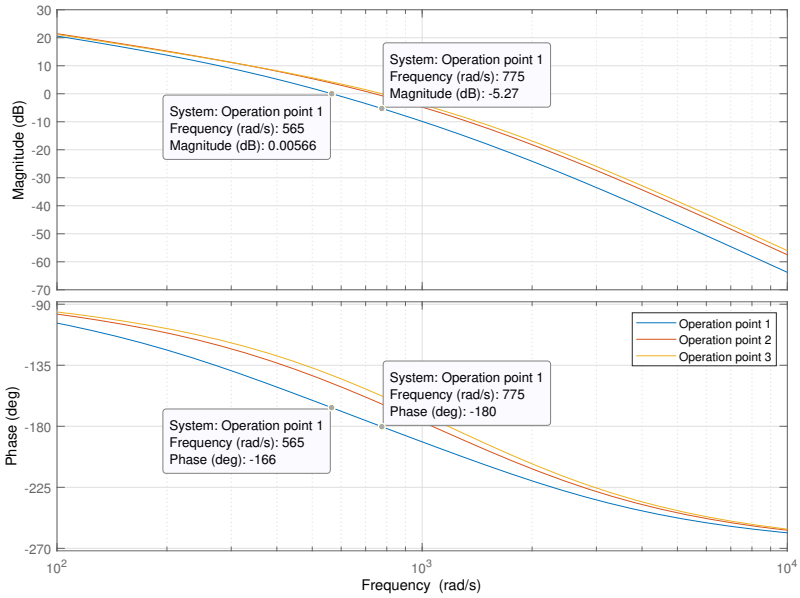

Figure 5.18: Bode plot of the open loop transfer with regulator gain according to modulus optimum

The open loop transfer function is therefore re-plotted in figure 5.19 with the gain parameter k_p of the PI-controller multiplied with a factor of 0.5. The gain margin is then increased to $-11.2db$, while the phase margin is increased to $31°$. The increased phase and gain margin results in less oscillations and better stability of the system.

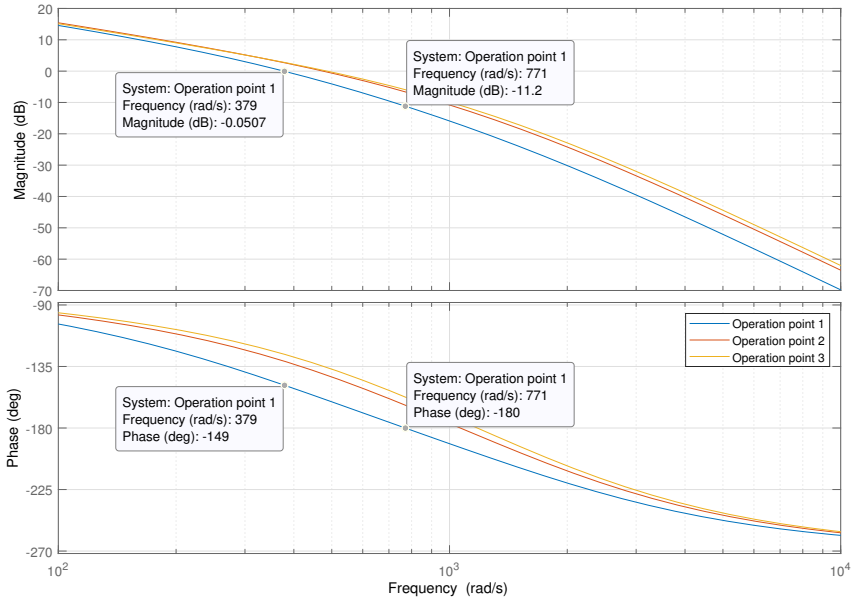

Figure 5.19: Bode plot of the open loop transfer with adjusted regulator gain

The control loop is closed and the closed loop transfer function is calculated according to equation 5.41. Figure 5.20 displays the closed loop transfer function with regulator gain according to modulus optimum, while the adjusted gain case is displayed in figure 5.21. The magnitude peak in the first plot approaches $20db$, which indicates a potential unstable system. The regulator gain was reduced in the second case, which resulted in lower magnitude peak and a more stable system. However, the bandwidth is observed to be considerably lower.

$$M(s) = \frac{G_{rf} \cdot G_{ef} \cdot G^*_{u_f i_f}}{1 + G_{ffi} \cdot G_{rf} \cdot G_{ef} \cdot G^*_{u_f i_f}} \tag{5.41}$$

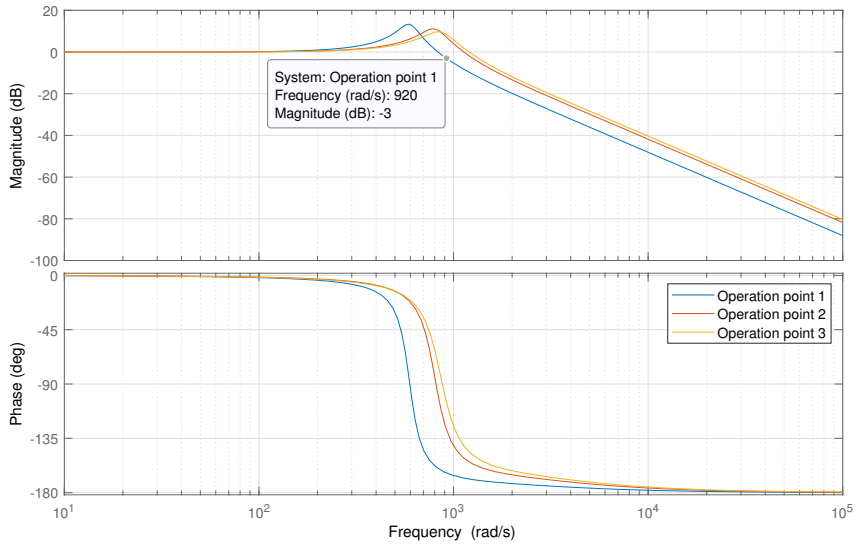

Figure 5.20: Bode plot of the closed loop transfer with regulator gain according to modulus optimum

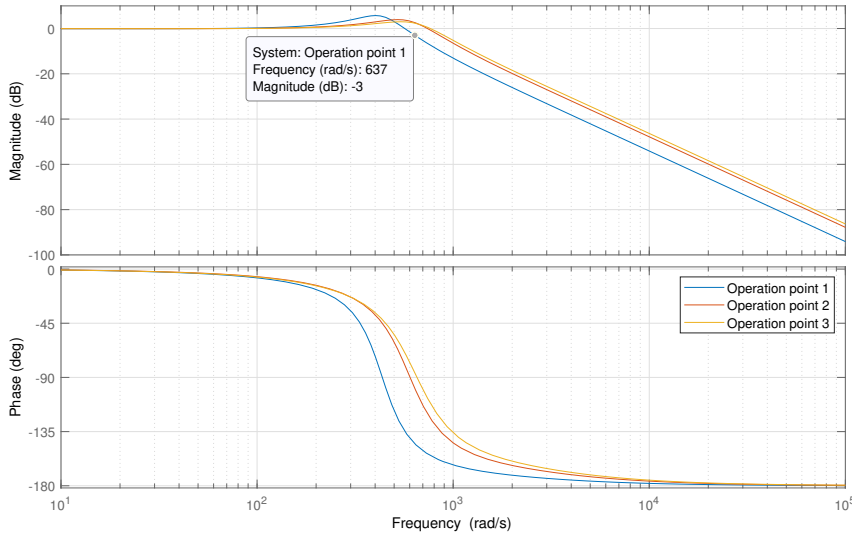

Figure 5.21: Bode plot of the closed loop transfer with adjusted regulator gain

5.5 Additional considerations

5.5.1 Changing the inductance x_f

The inductance x_f varies depending on cable length and eventual components between the generator and the diode rectifier. If the diode rectifier is connected in close proximity to the generator, the value of x_f could be assumed to be zero. Different values of x_f are investigated, spanning between very small to very large inductances. The result for the transfer function $G_{u_{dc}i_z}(s)$ is displayed in figure 5.22. Operation point 2 are plotted with four values of x_f, where $x_f = 0.05pu$ is the default value and $x_f = 1pu$ is an unrealistic high value for these kinds of systems. The most notable difference between the different values is the steady state gain, and the highest frequency breakpoint. The increased x_f results in a reduction of bandwidth, which can be observed in the closed loop transfer function in figure 5.23. However, the difference between the $x_f = 0.05$ and $x_f = 0$ are negligible. It is therefore possible to assume $x_f \approx 0$ in order to simplify the governing equations.

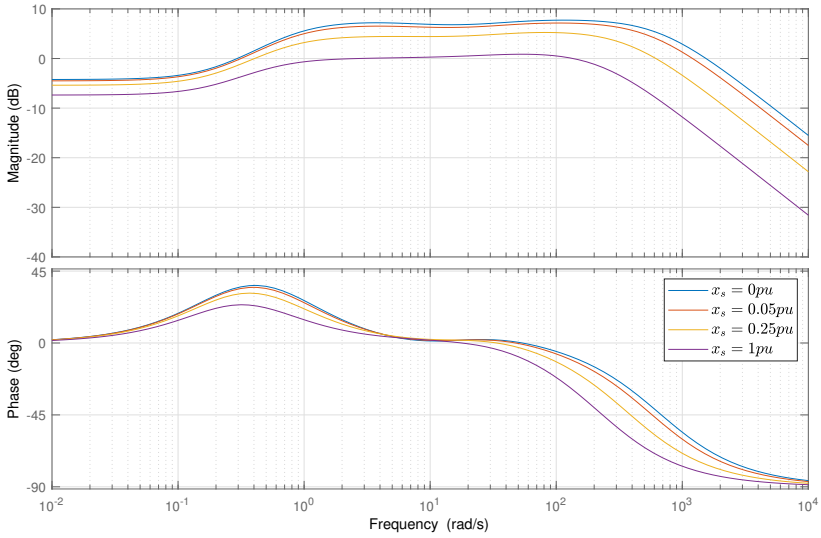

Figure 5.22: Bode plot of $G_{u_{dc}i_z}(s)$ with varying line inductance

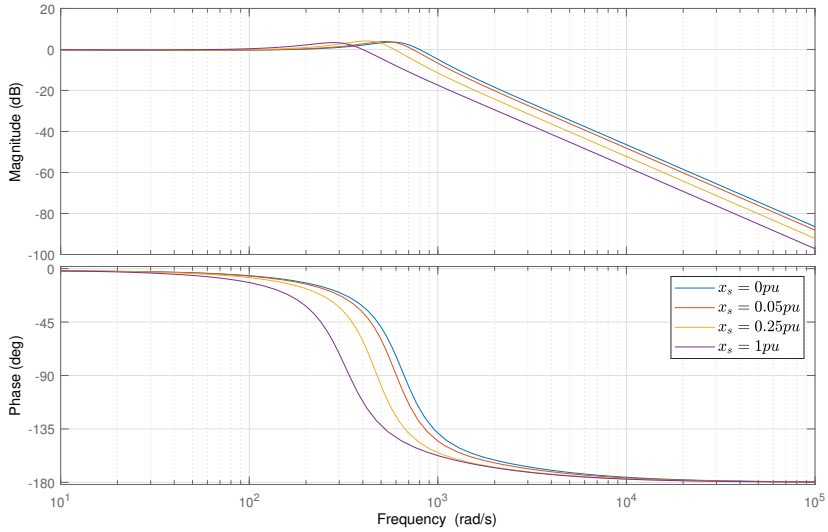

Figure 5.23: Bode plot of the closed loop transfer function with varying line inductance

5.5.2 Changing DC-link capacitor

The value of the DC-link capacitor varies depending on the number of inverters connected to the DC-link. The three operations point are analyzed with capacitor values which are calculated based on the total load power. They are calculated based purely on the active power load of the DC-link. They do not take into account that multiple converters could be connected and operating with reduced load. The values for the different operation points was presented in table 4.1, and the open loop transfer function plotted in figure 5.24. It is observed that low capacitor values occurring in operation point one result in a magnitude deviation in the $10^1 rad/s$ to $10^3 rad/s$ range compared to the other two operation point. The impact on the closed loop transfer function can be observed in figure 5.25. The transfer function for operation point one has a noticeable drop before the breakpoint.

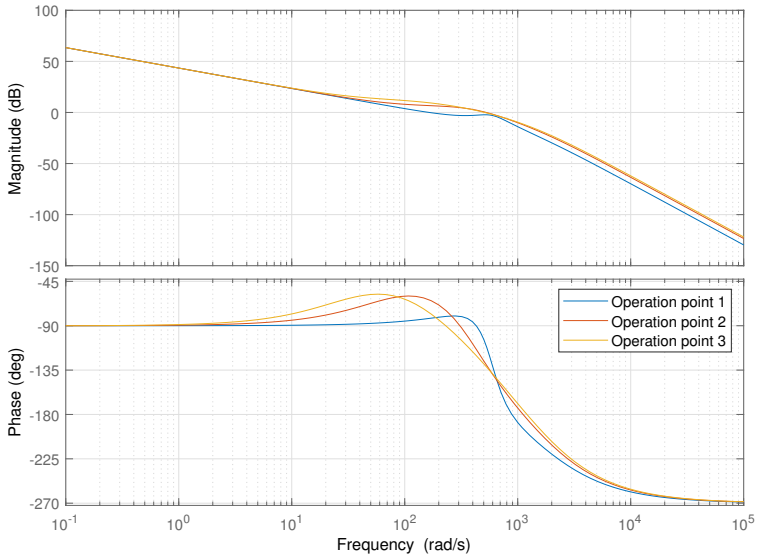

Figure 5.24: Bode plot of the open loop transfer function with varying capacitor value

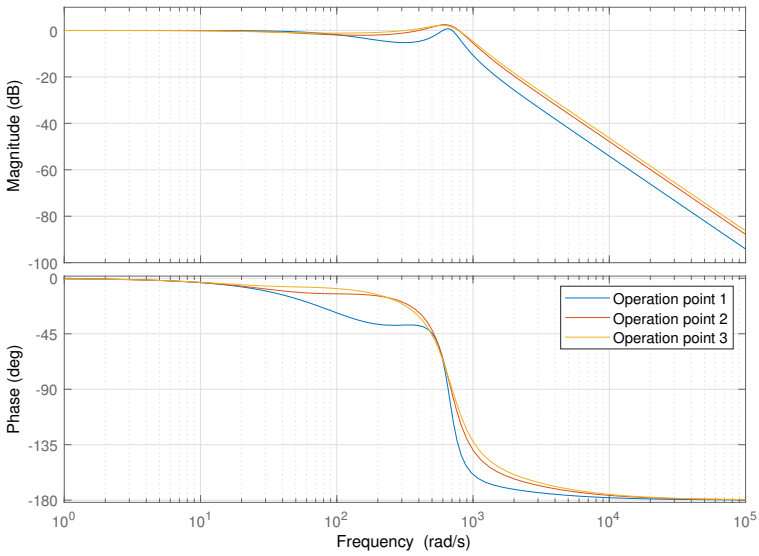

Figure 5.25: Bode plot of the closed loop transfer function with varying capacitor value

The regulator gain is increased as an attempt to improve the closed loop response. The transfer function for operation point one with and without increased gain are plotted in figure 5.26. It can be observed that the magnitude deviation is smaller with the increased gain. However, the magnitude peak is rather high, indicating a less stable system.

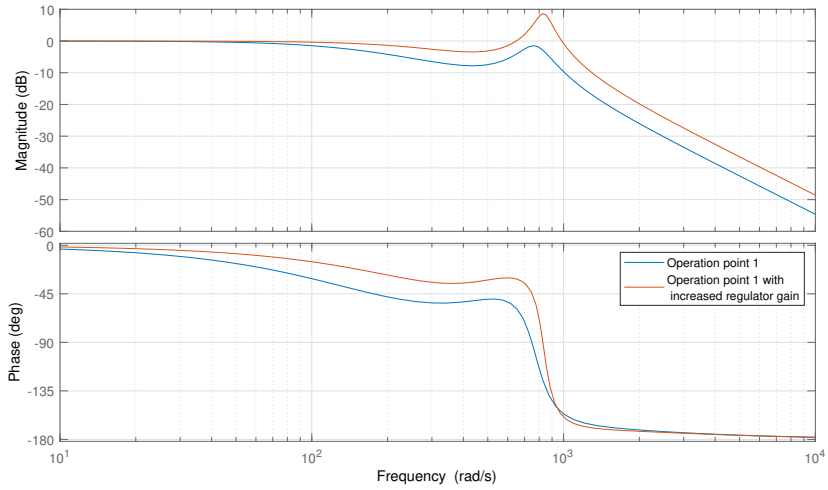

Figure 5.26: Bode plot of the closed loop transfer function small capacitor value and increased regulator gain

Chapter 6

Discussion

The shipboard DC-distribution system has in later years emerged as a competitor to the traditional AC-distribution system. Even though the DC-system is hardly a new technology, the significance of the system has been small compared to its AC counterpart. Recent development, especially in power electronics, has affected the usability and therefore the relevancy of the system. However, due to previous modest use, the DC-distribution technology lacks in studies, analysis and familiarity compared to the AC-system. The content of this thesis therefore had an emphasis on theoretical background, mathematical deducing of equations and understanding of the source material. A solid understanding of grid design philosophy is essential when system control structure and design are decided. The strict safety requirements for the shipboard power system, together with the system characteristics, lays the foundation for this philosophy.

The DC-distribution system was investigated to explore central concepts which are important for system modeling and design. The defining concept for the modeling was the introduction of a varying generator speed. This is due to the fuel consumption reduction of prime movers when operated at optimal speed instant of constant speed. The prime movers in an AC-system are operated at constant speed to achieve rated frequency. This is not a constraint in the DC-system. The speed controller adjusts the speed of the prime mover in order to achieve optimal fuel consumption. The design of- and the dynamic response of the speed controller are not considered in this report. A future priority should therefore be placed on expanding the understanding the prime mover and associated speed controller, since it is a vital part of the overall systems. Additionally, the option of implementing an energy storage system, which can further improve fuel saving, was considered. A long-term objective for future projects could be to conduct a thorough investigation of the attributes, control strategies and implementation of such a system.

The prime mover and DC-link load consideration are two important subjects which was only briefly analyzed in this report. Every load connected to a DC-link is connected through an inverter, since they are inherently AC. It was mentioned that these loads have a destabilizing effect on the system, but no further explanation was given, or analysis conducted. Likewise, a short introduction was given for the prime mover, and a graph of the fuel consumption was presented. An important continuation for future project should therefore be to expand on these subjects. An increased understanding of the prime mover can contribute to speed controller design and its impact on the overall dynamic of the system. An analysis of the loads can reveal potential instability problems and contribute to develop solutions to handle these problems.

The most intricate element in the system, both from a theoretical and a dynamical perspective, is the synchronous machine. Due to the importance of the synchronous machine, a considerable effort was spent on understanding and deducing the Park/Clark transformation and the resulting generator model. The model was represented as per unit values and the damper windings was eliminated, which is beneficial for control purposes. The reasoning behind the chosen pu values were not analyzed-, and the deduction of the equations utilized to eliminate the damper windings from the model were not included in this report. Potential further work could include more detailed analysis of this themes, in order to increase the understanding of the model.

An average value method was utilized in the diode rectifier modeling. The harmonics in the voltages and currents are neglected in this method and only an average value considered. The harmonics of the diode rectifier connected to a DC-link, analyzed in specialization project, was shown to be dependent the operation modes of the rectifier. The average value method might be inaccurate depending on the operation mode of the rectifier. This dependency should be investigated when the complete system is simulated.

The system variables were investigated as functions of the intermediate current. The intermediate current was chosen as the function variable since the modeling of the diode rectifier was based on the constant current model. However, the system variable was shown to be dependent on both the stator flux and the intermediate current. An expression of the stator flux as a function of the intermediate current should therefore be developed. It is then possible to expresses the systems variables as function dependent on the intermediate current, and otherwise constant values.

The focal point in this report was the modeling and design of the inner field current controller. The terminal voltage of the generator is determined, among others, by the generator field current. The combined inner field current controller and outer voltage controller regulates the field current until requested DC-link voltage is achieved. A linear description of the system is a pre-requisite for modeling it with Laplace transformed transfer function. It was observed that the transitional variables introduced an un-linearity to the transitional equations, which needed to be linearized. The current linearization variables were obtained for the current equations and plotted as a function of the intermediate current. The stator flux is in these considerations assumed equal to $1pu$, since the intermediate current/stator flux relation is not determined. The expression for calculating the voltage linearization variables were established, but the calculations were not followed through due to time constraints. The voltage relation between the generator model and rectifier model was therefore assumed to be linear. It is necessary to verify if the assumption is valid, and if not, continue to derive the linearization variables.

A signal flow diagram was created for the combined rectifier and generator system. The signal flow diagram was node and branch reduced until a transfer function describing the relation between the field voltage and field current was established. It was observed that this transfer function could be considered a first order system, which made it possible to utilize the tuning principle modulus optimum. The stability of the complete field current regulation system was examined by considering the gain and phase margin. Some adjustments of the regulator gain resulted in a stable system according to the phase and gain margin considerations. However, a thorough stability analysis of the process transfer function was not conducted. The closed loop system could therefore contain right half-plane singularities which are not observed in the bode plot. A more detailed stability analysis, perhaps utilizing Nyquist diagram, should be conducted to determine absolute stability for different operation scenarios.

Different values of the inductances x_f and the DC-link capacitor were investigated. It was observed that the x_f primarily influences the bandwidth of the closed loop transfer function. x_f is usually small compared to the generator leakage inductance and can therefore be assumed to be zero in many cases. Reduced capacitance of the DC-link capacitor caused the magnitude to notably deviate from zero decibel before the function breakpoint. An increase of regulator gain had an improving effect, but the added side effect of a less stable system. The cause of the magnitude deviations was not investigated in detail due to time constraints. A thorough analysis of the process transfer function should be conducted to determine the capacitors influence, and how to counter the experienced problem.

Chapter 7

Conclusion

This thesis investigates the DC-distribution system, which has gain increased attention in the maritime industry. The distribution system is supplied from a synchronous generator connected thorough a diode rectifier. This solution has reduced flexibility compared to active rectifiers, since the diodes cannot be controlled. The voltage control on the DC-link is therefore provided by regulating the generator field current. A model representing the entire system, including generator, rectifier and capacitor, was therefore necessary in order to design the filed circuit control system.

A theoretical study was conducted on the shipboard power system and a DC-distribution system. The DC-system has no frequency constraints, which makes it possible to operate the prime movers at optimal fuel consummation speed. A combined model for the entire system was created where the varying speed consideration was included. A signal flow diagram was constructed for the combined system consisting of Laplace transformed transfer function deduced for the system. The signal flow diagram was branch and node reduced until a single transfer function for the relation between the field voltage and field current was obtained. The resulting filed circuit transfer function are then the process element in the regulated system.

The process transfer function was observed to be approximately equal to a first order system. The process gain was equal to the inverse field resistance while the breakpoint occurred at the field time constant. This approximation was utilized in the regulator tuning, which made it possible to apply the tuning principle modulus optimum. The regulator parameters were adjusted in order to obtain a stability margin based on gain margin and phase margin. The system appeared stable for the solution proposed, however a thorough stability analysis must be conducted. Additionally, the influence of the capacitor should be investigated further.

The models developed in this thesis establishes a foundation for further development, regulator design and stability analysis. The inner current control system appears stable, but more research is necessary before a definite conclusion can be drawn. A theoretical background for the system is constructed, but some additions might be beneficial to increase the understanding of the subjects. A detailed recommendation for further work is presented in chapter 8.

Chapter 8

Further work

The further work can be divided into the category's theoretical enhancement, continuation of the current work and long-term possibilities.

The theoretical enhancement is primarily on important elements in the system, which was just briefly analyzed or mentioned, but some additional insight could benefit for some of the themes explored:

- Further analysis of the synchronous machine and deducing the equations utilized in the block diagram.
- Investigate different droop control schemes applicable for the DC-link voltage droop.
- Establish a theoretical foundation and create models of the prime mover, loads and the energy storage system.

The continuations of the current work involve the tasks necessary to complete the generators control systems:

- Develop an expression for the stator flux as a function of the intermediate current
- Linearize the transitional voltage equations or verify the assumption that this equation is almost linear.
- Thorough stability analysis of the field circuit.
- Examine the final field circuit transfer function and determine the capacitors influence on the system.
- Design the outer voltage controller.

Long-term possibilities consist of task which are currently not considered as objectives in the problem description but could be interesting future continuation of the project.

- Design the optimal speed controller
- Design the ESS-control system
- Analysis the entire system including multiple parallel connected generators and a energy storage system.

Bibliography

[1] E. Skjong, R. Volden, E. Rødskar, M. Molinas, T. A. Johansen, and J. Cunningham, "Past, present, and future challenges of the marine vessel's electrical power system," *IEEE Transactions on Transportation Electrification*, vol. 2, pp. 522–537, Dec 2016.

[2] International Maritime Organization (IMO), "Prevention of Air Pollution from Ships." `http://www.imo.org/en/OurWork/Environment/PollutionPrevention/AirPollution/Pages/Air-Pollution.aspx`, 2010. [Online; accessed 13.02.2019].

[3] U. Javaid, D. Dujić, and W. van der Merwe, "Mvdc marine electrical distribution: Are we ready?," in *IECON 2015 - 41st Annual Conference of the IEEE Industrial Electronics Society*, pp. 000823–000828, Nov 2015.

[4] J. F. Hansen, J. O. Lindtjørn, and K. Vanska, "Onboard dc grid for enhanced dp operation in ships." `https://dynamic-positioning.com/proceedings/dp2011/power_hansen.pdf`, 2012. [Online; accessed 16.02.2019].

[5] J. O. Lindtjørn, "Onboard dc grid – a system platform at the heart of shipping 4.0." `https://new.abb.com/marine/generations/generations-2017/business-articles/onboard-dc-grid-a-system-platform-at-the-heart-of-shipping`, 2011. [Online; accessed 16.02.2019].

[6] J. A. M. Bleijs, "Continuous conduction mode operation of three-phase diode bridge rectifier with constant load voltage," *IEE Proceedings - Electric Power Applications*, vol. 152, pp. 359–368, March 2005.

[7] P. Pejović and J. W. Kolar, "An analysis of three-phase rectifiers with constant voltage loads," in *Circuits and Systems for Communications (ECCSC), 2010 5th European Conference on*, pp. 119–126, IEEE, 2010.

[8] N. Mohan, T. M. Undeland, and W. P. Robbins, *Power Electronics. Converters, Applications and Design*. John Wiley and Sons, Inc, third ed., 2003.

[9] I. Jadric, D. Borojevic, and M. Jadric, "Modeling and control of a synchronous generator with an active dc load," *IEEE Transactions on Power Electronics*, vol. 15, pp. 303–311, March 2000.

[10] N. Doerry, "Naval power systems: Integrated power systems for the continuity of the electrical power supply.," *IEEE Electrification Magazine*, vol. 3, pp. 12–21, June 2015.

[11] DNV-GL, "Dynamic positioning vessel design philosophy guidelines." http://rules.dnvgl.com/docs/pdf/dnvgl/RP/2015-07/DNVGL-RP-E306.pdf, 2012. [Online; accessed 16.02.2019].

[12] R. E. HEBNER and authors, "Technical cross-fertilization between terrestrial microgrids and ship power systems," *Journal of Modern Power Systems and Clean Energy*, vol. 4, pp. 161–179, Apr 2016.

[13] A. B. Jusoh, "The instability effect of constant power loads," in *PECon 2004. Proceedings. National Power and Energy Conference, 2004.*, pp. 175–179, Nov 2004.

[14] M. Patel, "Shipboard electrical power systems." https://doi.org/10.1201/b11359, 2012. [Online; accessed 13.02.2019].

[15] Wärtsilä, "Shaft generators: propelling vessels toward leaner, greener power generation." https://www.wartsila.com/twentyfour7/in-detail/shaft-generators-propelling-vessels-toward-leaner-greener-power-generation, 2016. [Online; accessed 29.04.2019].

[16] B. Zahedi and L. E. Norum, "Efficiency analysis of shipboard dc power systems," in *IECON 2013 - 39th Annual Conference of the IEEE Industrial Electronics Society*, pp. 689–694, Nov 2013.

[17] R. Nilsen and I. Sorfonn, "Hybrid power generation systems," in *2009 13th European Conference on Power Electronics and Applications*, pp. 1–9, Sep. 2009.

[18] R. M. Calfo, J. A. Fulmer, and J. E. Tessaro, "Generators for use in electric marine ship propulsion systems," in *IEEE Power Engineering Society Summer Meeting,*, vol. 1, pp. 254–259 vol.1, July 2002.

[19] ABB, "Onboard dc grid: The step forward in power generation and propulsion." https://resources.news.e.abb.com/attachments/published/13107/en-US/A79B8B042988/12-10-onboarddcgrid-technical-information.pdf, 2011. [Online; accessed 16.02.2019].

[20] R. Prenc, A. Cuculić, and I. Baumgartner, "Advantages of using a dc power system on board ship," 2016.

[21] "Ieee recommended practice for 1 kv to 35 kv medium-voltage dc power systems on ships," *IEEE Std 1709-2010*, pp. 1–54, Nov 2010.

[22] V. Staudt, R. Bartelt, and C. Heising, "Fault scenarios in dc ship grids: The advantages and disadvantages of modular multilevel converters.," *IEEE Electrification Magazine*, vol. 3, pp. 40–48, June 2015.

[23] P. Kundur, *"Power System Stability and Control"*. McGraw-Hill, Inc., 1993.

[24] R. Nilsen, *SIE 1025 Elektriske motordrifter, compendium*. Norwegian University of Science and Technology, Department of Electric Power Engineering, 2002.

[25] R. Nilsen, *TET4120 Electrical Drives, compendium*. Norwegian University of Science and Technology, Department of Electric Power Engineering, 2018.

[26] H. Bühler, *Einführung in die Theorie geregelter Drehstromantriebe, Band1:Grundlagen*. Birkhäuser verlag basel und stuttgart, first ed., 1977.

[27] S. Moriyasu and C. Uenosono, "An analysis on the characteristics of a synchronous machine connected to a d.c.-link," *Archiv für Elektrotechnik*, vol. 69, pp. 111–120, Mar 1986.

[28] H. Bühler, *Einführung in die Theorie geregelter Drehstromantriebe, Band2:Anwendungen*. Birkhäuser verlag basel und stuttgart, third ed., 1977.

[29] S. J. Mason, "Feedback theory-some properties of signal flow graphs," *Proceedings of the IRE*, vol. 41, pp. 1144–1156, Sep. 1953.

Appendix A

Generator data

$$S_n = 13.75MW \qquad U_{LL} = 1000V$$
$$f = 60Hz \qquad I_n = 7940A$$

$$x_d = 2.07pu \qquad x_q = 1pu$$
$$x'_d = 0.402pu \qquad x''_q = 0.315pu$$
$$x''_d = 0.273pu$$

$$r_s = 0.00665pu \qquad x_{md} = 1.835pu$$
$$r_f = 0.001339pu \qquad x_{mq} = 0.765pu$$

$$T'_d = 1.15 \qquad T'_{d0} = 4.8 \qquad T''_{q0} = 0.116$$
$$T''_d = 0.024 \qquad T''_{d0} = 0.032 \qquad T''_q = 0.027$$
$$T_a = 0.14$$

$$x_{f\sigma} = 0.1837pu \qquad x_{D\sigma} = 0.0492pu \qquad x_{Q\sigma} = 0.0843pu$$
$$x_f = 2.0187pu \qquad x_D = 1.8842pu \qquad x_Q = 0.8542pu$$

Appendix B

Speed and load considerations

The system parameters are calculated for three different operation points. The correlation between the prime mover speed and produced power is given by figure 3.5. The equations involved in the calculations is presented in expression array B.1.

$$\begin{aligned} \hat{U}_n &= \frac{\sqrt{2}}{\sqrt{3}} \cdot U_{LL} & Z_b &= \frac{U_b^2}{S_b} \\ U_b &= \hat{U}_n & Z_{\sigma_a} &= Z_{\sigma_{pu}} \cdot Z_b \\ S_b &= S_n & L_\sigma &= \frac{Z_\sigma}{\omega_n} \end{aligned} \tag{B.1}$$

The generator data necessary for the calculations are shown is expression array B.2.

$$\begin{aligned} S_n &= 13.75MW & I_n &= 7940A \\ U_{LL} &= 1000V & z_\sigma &= 0.29pu \end{aligned} \tag{B.2}$$

Utilizing the values from expression array B.2 in the equations in expression array B.1 yields the following value for the commutation inductance. The transformation to real values was to be able to verify the results in a Simulink model.

$$L_\sigma = 37.14\mu H \qquad L_s \approx 0 \tag{B.3}$$

The three different operation points was chosen according to the following arguments. Note that the power listed is according to DC-link reference, which gives positive sign. The power produced by the generator, with motor reference, would result in negative active power.

Operation 1: As explored in chapter 2.3 constant current assumption is inaccurate at low loading. It it therefore assumed that continuous operation below $0.2pu$ loading does not occur. This yields a prime mover speed of $0.2pu$.

Operation 3: Operation speed two is set to the prime mover operating at maximum speed of $n = 1pu$. The active power relation is defined such that maximum production of the prime mover results in $0.9pu$ of power from the generator. The remaining $0.1pu$ is utilized to cover reactive power.

Operation 2: The second, or middle, operation point is then chosen as the speed in the middle of the two previous determined operation point. This give a speed of $0.8pu$ and $0.52pu$ of active power.

The operation parameter for the three operation points in then calculated with the equations in expression array B.4. The result is presented in table B.1.

$$\begin{aligned} U_{dio} &= U_{dc} + U_{dk} & \qquad U_{br} &= \frac{3 \cdot \sqrt{3}}{\pi} \cdot \hat{U_n} \\ U_{dk} &= -\frac{3}{\pi}\omega L_i \cdot I_z & \qquad I_{\mathrm{br}} &= \frac{\pi}{2\sqrt{3}} \cdot \hat{I}_{\mathrm{n}} \\ I_z &= \frac{P_{load}}{U_{dc}} & \qquad u_{dio} &= \frac{U_{dio}}{U_{br}} \\ x_c &= \frac{1}{C \cdot \omega_n} \cdot \frac{I_{\mathrm{br}}}{U_{\mathrm{br}}} & \qquad \omega &= n \cdot \omega_n \end{aligned} \tag{B.4}$$

Table B.1: Generator operation points

Operation point one	Operation point two	Operation point three
$p_1 = 0.2pu$	$p_2 = 0.52pu$	$p_3 = 0.9pu$
$n_1 = 0.58pu$	$n_2 = 0.8pu$	$n_3 = 1pu$
$u_{dio_1} = 0.757pu$	$u_{dio_2} = 0.78pu$	$u_{dio_3} = 0.864pu$
$i_{z_1} = 0.27pu$	$i_{z_2} = 0.72pu$	$i_{z_3} = 1.23pu$
$\psi_1 = 1.305pu$	$\psi_2 = 1pu$	$\psi_3 = 0.864pu$
$x_c = 0.67pu$	$x_c = 0.29pu$	$x_c = 0.17pu$

Appendix C

Combined system vector calculations

A vector diagram is drawn based on the second generator operation point. The relevant generator and operation parameters are given in array C.1.

$$\begin{array}{rr} & x_d = 2.07pu \\ \psi_s = 1pu & x_q = 1pu \\ n = 0.8pu & x_{md} = 1.853pu \\ i_z = 0.72pu & x_\sigma = 0.29pu \\ & r_s = 0.00665pu \end{array} \tag{C.1}$$

The angles δ and φ_{g_1} are found by applying the values from array C.1 in the equations C.2 and C.3.

$$\delta = -\arctan\left(\frac{i_z \cos\left(\varphi_{g_1}\right) \cdot x_q}{i_z \sin\left(\varphi_{g_1}\right) \cdot x_q + \psi_s}\right) \tag{C.2}$$

$$\varphi_{g_1} = \arccos\left(1 - \frac{\pi}{6} \cdot \frac{x_i i_z}{\psi_s}\right) \tag{C.3}$$

When these angles are known, the d- and q-axis voltages and current can be calculated with expression array C.4 and the field current with equation C.5.

$$\begin{array}{ll} u_d = -u_s \cdot \sin(\delta) & u_q = u_s \cdot \cos(\delta) \\ i_d = -i_z \cdot \sin(\varphi_{g_1} - \delta) & i_q = i_z \cos(\varphi_{g_1} - \delta) \end{array} \tag{C.4}$$

$$i_f = \frac{\psi_s \cos(\delta) - i_z \cdot x_d \cdot \sin\left(-\varphi_{g_1} + \delta\right)}{x_{md}} \tag{C.5}$$

The resulting values are presented below:

$$\begin{aligned} u_d &= 0.34pu & u_q &= 0.7pu \\ i_d &= -0.57pu & i_q &= -0.44pu \\ u_p &= 1.67pu & i_f &= 1.13pu \\ \varphi_1 &= 27.0^\circ & \delta &= -24.2^\circ \\ r_s \cdot i_d &= -0.0038pu & r_s \cdot i_q &= -0.0029pu \\ n \cdot x_d \cdot i_d &= -0.95pu & n \cdot x_q \cdot i_q &= -0.35pu \end{aligned} \tag{C.6}$$

The phasor diagram is then drawn based on the values from array C.6 in figure C.1.

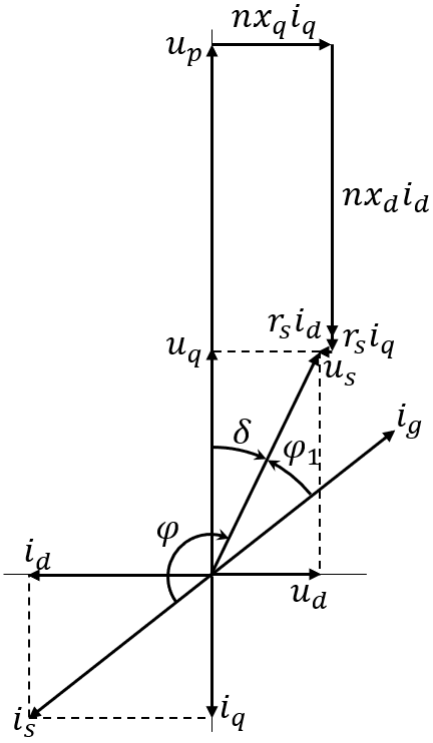

Figure C.1: Vector diagram for the combined system

Appendix D

Linearization

This appendix contains the calculations of the linearization variables presented and discussed in chapter 5.1.

D.1 Current relation

D.1.1 d-axis current

The equation for the d-axis current is given by equation D.1. The linearization variable is calculated according to equation D.2. The result of the derivation is presented in equation D.5. The linear relationship between i_d and i_z is then given by equation D.6.

$$i_d = -i_z \cdot \sin(\varphi_p) \tag{D.1}$$

$$K_{dz} = \frac{di_d}{di_z} \tag{D.2}$$

$$\begin{aligned} u &= -i_z & v &= \sin(\varphi_p) \\ u' &= -1 & v' &= \cos(\varphi_p) \cdot \frac{d\varphi_p}{di_z} \end{aligned} \tag{D.3}$$

$$K_{dz} = -\sin(\varphi_p) - i_s \cos(\varphi_p) \cdot \frac{d\varphi_p}{di_z} \tag{D.4}$$

$$-K_{dz} = \sin(\varphi_p) + i_s \cos(\varphi_p) \cdot \frac{d\varphi_p}{di_z} \tag{D.5}$$

$$\Delta i_d = -K_{dz} \Delta i_z \tag{D.6}$$

D.1.2 q-axis current

The equation for the q-axis current is given by equation D.7. The linearization variable is calculated according to equation D.8. The result of the derivation is presented in equation D.10. The linear relationship between i_q and i_z is then given by equation D.11.

$$i_q = -i_z \cdot \cos(\varphi_p) \tag{D.7}$$

$$K_{qz} = \frac{di_q}{di_z} \tag{D.8}$$

$$\begin{aligned} u &= -i_z & v &= \cos(\varphi_p) \\ u' &= -1 & v' &= -\sin(\varphi_p) \cdot \frac{d\varphi_p}{di_z} \end{aligned} \tag{D.9}$$

$$K_{qz} = -\cos(\varphi_p) + i_z \sin(\varphi_p) \cdot \frac{d\varphi_p}{di_z} \tag{D.10}$$

$$\Delta i_q = K_{qz} \Delta i_z \tag{D.11}$$

D.2 Voltage relation

The voltage relation is given by equation D.12. The d- and q-axis terms are analyzed separately.

$$u_{dio} = u_q \cdot \cos(\delta) - u_d \cdot \sin(\delta) \tag{D.12}$$

D.2.1 d-axis voltage

The equation for the q-axis part of the voltage relation is given by equation D.20. The linearization variable is calculated according to equation D.8. The result of the derivation is presented in equation D.25

$$u_{dio_1} = -u_d \cdot \sin(\delta) \tag{D.13}$$

$$\Delta u_{dio} = \Delta u_d \cdot K_{du} \tag{D.14}$$

$$K_{du} = \frac{du_{dio}}{du_d} \tag{D.15}$$

$$u \cdot v' + u' \cdot v \tag{D.16}$$

$$\begin{aligned} u &= -u_d & v &= \sin(\delta) \\ u' &= -1 & v' &= \cos(\delta) \cdot \frac{d\delta}{du_d} \end{aligned} \tag{D.17}$$

$$K_{du} = -\sin(\delta) - u_d \cos(\delta) \cdot \frac{d\delta}{du_d} \tag{D.18}$$

$$-K_{du} = \sin(\delta) + u_d \cos(\delta) \cdot \frac{d\delta}{du_d} \tag{D.19}$$

D.2.2 q-axis voltage

The equation for the q-axis part of the voltage relation is given by equation D.20. The linearization variable is calculated according to equation D.8. The result of the derivation is presented in equation D.25.

$$u_{dio_2} = u_q \cdot \cos(\delta) \tag{D.20}$$

$$\Delta u_{dio_2} = \Delta u_q \cdot K_{qu} \tag{D.21}$$

$$K_{qu} = \frac{du_{dio_2}}{du_q} \tag{D.22}$$

$$u \cdot v' + u' \cdot v \tag{D.23}$$

$$\begin{array}{ll} u = u_q & v = \cos(\delta) \\ u' = 1 & v' = -\sin(\delta) \cdot \dfrac{d\delta}{du_q} \end{array} \tag{D.24}$$

$$K_{qu} = \cos(\delta) - u_q \sin(\delta) \cdot \frac{d\delta}{du_q} \tag{D.25}$$

D.2.3 Linearized voltage relation

The equation for the linearized voltage relations then results in:

$$\Delta u_{dio} = K_{qu} \cdot \Delta u_q - K_{du} \cdot \Delta u_d \tag{D.26}$$

In order to utilize this equation, expressions for the angle δ as a function of the d- and q-axis voltage must be derived. This is not included in this report due to time issues.

Appendix E

Tuning theory and calculations

E.1 Modulus optimum

The tuning principle *modulus optimum* is utilized to tune the field PI-controller [25, p.103]. The field current open loop transfer function contains one large dominant time constant ($T_{d0}^{'}$), and two smaller ones (T_{ffi} and T_{fe}). The smaller time constant can be merge into one time constant T_{sum}, if they are considerable smaller than the dominant one. The open loop system can then be written as:

$$h_0(s) = K_p \frac{1 + T_i \cdot s}{T_i \cdot s} \cdot K_s \frac{1}{1 + T_{sum} \cdot s} \cdot \frac{1}{1 + T_1 \cdot s} \tag{E.1}$$

The PI-controller time constant is chosen equal to the dominant time constant, which yields the following open loop transfer function.

$$h_0(s) = \frac{K_p K_s}{T_1} \cdot \frac{1}{s\left(1 + T_{sun} \cdot s\right)} \tag{E.2}$$

The closed loop transfer function then becomes:

$$M(s) = \frac{1}{1 + \frac{T_1}{K_p K_s} \cdot s + \frac{T_1 T_{sum}}{K_p K_s} \cdot s^2} \tag{E.3}$$

$$= \frac{1}{1 + 2\zeta \cdot \frac{s}{\omega_0} + \left(\frac{s}{\omega_0}\right)^2} \tag{E.4}$$

By comparing equation E.3 the following expressions are deduced:

$$\omega_0 = \sqrt{\frac{K_p K_s}{T_1 T_{sum}}} \qquad\qquad \zeta = \frac{1}{2}\sqrt{\frac{T_1}{K_p K_s T_{sum}}} \tag{E.5}$$

Finally, K_p is chosen such that the relative damping becomes $1/\sqrt{2}$. Then controller parameters then become:

$$\begin{aligned} T_i &= T_1 & \zeta &= \frac{1}{\sqrt{2}} \approx 0.7 \\ K_p &= \frac{T_1}{2K_s T_{sum}} & \omega_0 &= \frac{1}{\sqrt{2}T_{sum}} \end{aligned} \tag{E.6}$$

The open loop transfer function for the field circuit is given as:

$$h_0(s) = G_{r_f}(s) \cdot G_{ef}(s) \cdot G_{ffi}(s) \cdot G^*_{u_f i_f}(s) \tag{E.7}$$

$$= k_p \cdot \frac{1 + T_i \cdot s}{T_i \cdot s} \cdot \frac{u_{dio}}{1 + T_{fe} \cdot s} \cdot \frac{1}{1 + T_{ffi} \cdot s} \cdot \frac{K_{cs}}{1 + T_{cs} \cdot s} \tag{E.8}$$

The control parameters for the field current controller can then be calculated with equation E.9, where T_{sum} is given by equation E.10.

$$T_i = T_{cs} = T'_{d0} \qquad K_p = \frac{T_{cs}}{2 \cdot \frac{u_{dio}}{r_f} \cdot T_{sum}} \tag{E.9}$$

$$T_{sum} = T_{fe} + T_{ffi} \tag{E.10}$$

E.2 Filter calculations

A filter is design to reduce the ripple in the control circuit [25, p.115]. A first order filter is chosen, which has the following transfer function:

$$h_f(s) = \frac{1}{1 + T_f \cdot s} \tag{E.11}$$

According to [25] the ripple in a thyristor rectifier can be calculated as following:

$$^{\sim}I_{\max}(t) \approx \frac{U_{dio}}{\omega_n \cdot L} \cdot \widehat{w}_{i,\max} = 0.093 \cdot \frac{U_{dio}}{\omega_n \cdot L} \tag{E.12}$$

When the system is operating in steady state, the integral part of the controller can be neglected. The ripple at the output of the controller then becomes:

$$^{\sim}u_{control}(s) = K_p \cdot \frac{1}{1 + T_f \cdot s} \cdot^{\sim} I(s) \tag{E.13}$$

Equations E.13 is then expressed with the actual ripple frequency. Also, the expression for k_p from equation E.9 is inserted, which yields:

$$\sim u_{\text{control}}\left(\omega_{\text{ripple}}\right) = \frac{T_1}{2 \cdot K_s \cdot \left(T_{\text{delay}} + T_f\right)} \cdot \frac{1}{\sqrt{1 + \left(\omega_{\text{ripple}} \cdot T_f\right)^2}} \cdot^{\sim} I\left(\omega_{\text{ripple}}\right) \quad \text{(E.14)}$$

The expression for K_p from expression array E.9 is introduced in equation E.14. The resulting control ripple can then be expressed as:

$$\sim u_{\text{control}}\left(\omega_{\text{ripple}}\right) = \frac{0.093}{2 \cdot \left(T_{ffi} + T_{fe}\right) \cdot \omega_n \cdot \sqrt{1 + \left(6 \cdot \omega_n \cdot T_{ffi}\right)^2}} \quad \text{(E.15)}$$

Equation E.15 is plotted in figure E.1. The maximum ripple is set to be no more then 5%. This gives a filter time constant of $0.6ms$.

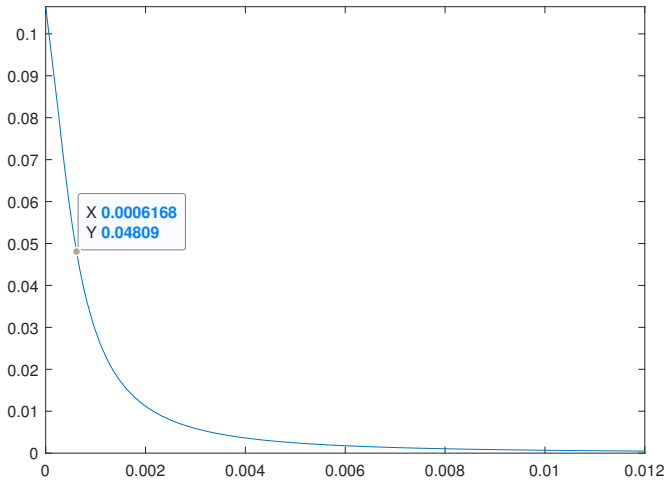

Figure E.1: Plot for deciding filter size

E.3 Calculation of controller parameters

The parameters for the controller are calculated with the expressions in equation array E.9. The only remaining unknown time constant belongs to the exciter. An exciter based on a thyristor rectifier are chosen. According to [26] the delay in a thyristor rectifier can be calculated with equation E.16, where T is the electric period.

$$T_{fe} = \frac{T}{12} \approx 1.4ms \tag{E.16}$$

The variables necessary for calculating the PI-controller parameters are presented below:

$$\begin{aligned} u_{dio} &= 2pu & \qquad T_{sum} &= 2ms \\ r_f &= 0.001339pu & \qquad T_{d0}^{'} &= 4.8s \end{aligned} \tag{E.17}$$

By utilizing the values from array E.17 in expression array E.9, the following parameters are obtained:

$$T_i = 4.8s \qquad\qquad K_p = 0.803 \tag{E.18}$$

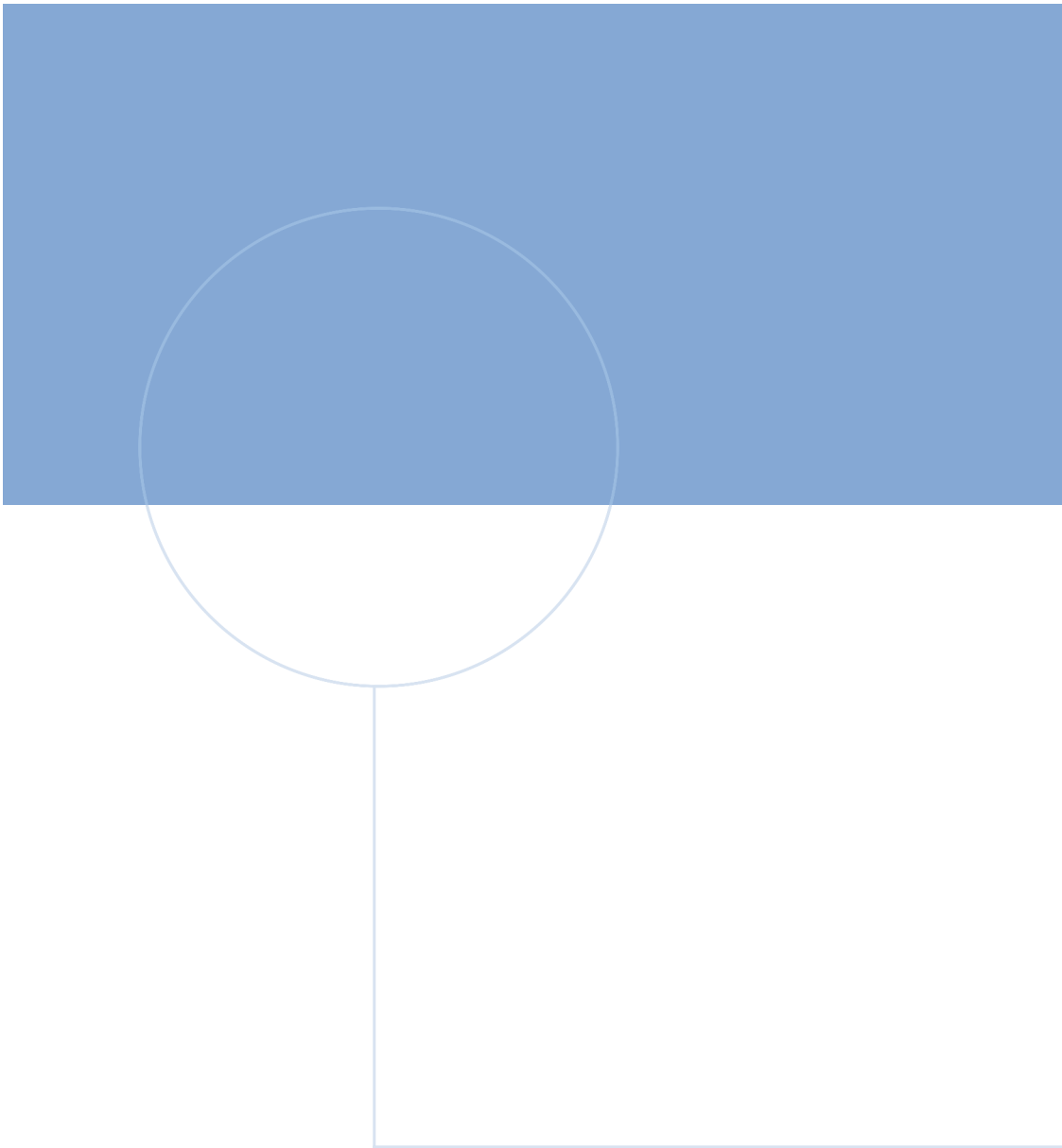

NTNU
Norwegian University of
Science and Technology